UNIVERSIDADE DE SÃO PAULO

INSTITUTO SÃO CARLOS

FREDDY JACKSON POVEDA CUEVAS

ASPECTS OF HYBRID CONFINEMENT FOR A BOSE-EINSTEIN CONDENSATE: GLOBAL PRESSURE AND COMPRESSIBILITY

SÃO CARLOS

2013

FREDDY JACKSON POVEDA CUEVAS

ASPECTS OF HYBRID CONFINEMENT FOR A BOSE-EINSTEIN CONDENSATE: GLOBAL PRESSURE AND COMPRESSIBILITY

Thesis presented to the Graduate Program in Physics at the São Carlos Institute of Physics, Universidade de São Paulo to obtain the degree of Doctor of Science.

Concentration area: Basic Physics
Advisor: Prof. Dr. Vanderlei S. Bagnato

Corrected Version

(Original version available on the Program Unit)

São Carlos

2013

Ficha catalográfica elaborada pelo Serviço de Biblioteca e Informação do IFSC,
com os dados fornecidos pelo(a) autor(a)

Poveda Cuevas, Freddy Jackson
Aspects of hybrid confinement for a Bose-Einstein condensate: global pressure and compressibility / Freddy Jackson Poveda Cuevas; orientador Vanderlei Salvador Bagnato - versão corrigida -- São Carlos, 2014.
113 p.

Tese (Doutorado - Programa de Pós-Graduação em Física Básica) -- Instituto de Física de São Carlos, Universidade de São Paulo, 2014.

1. Bose-Einstein condensation. 2. Thermodynamics. 3. Global variables. 4. Compressibility. I. Bagnato, Vanderlei Salvador, orient. II. Título.

A mi Familia.

Em homenagem ao Laboratório
de Física Atômica.

ACKNOWLEDGEMENTS

Acknowledgements in Portu-Espan-Glish:

Agradezco a Sandra cada momento compartido en estos cuatro años, porque a cada instante me hace recordar y vivir mis proprias palabras: *El camino y el tiempo compartidos son el pilar de nuestros triunfos.*

Ao Vanderlei, pelo exemplo, não só como cientista mas também como pessoa e sua particular forma de viver a vida. Obrigado pela oportunidade de trabalhar em meu futuro.

A mis padres Aura Rosa y José Fredy, por ayudarme a pensar con "lógica" en que todos los logros y esfuerzos tiene en algún momento una recompensa.

A mis hermanos Leonardo Andrés, Sergio Alejandro y Laura Catalina, por impulsarme a ser mejor para ustedes, y por ser simplemente esa alegría que me insitó a dedicarle esta tesis a toda mi familia. Junto con ellos voy a agradecer a mi hermano mayor Olmer por sus interesantes discusiones metafísicas.

A los que ahora considero mis segundos padres la señora Cecilia y don Pedro, por su constante apoyo en aquellos momentos que realmente lo necesitabamos.

Faço um agradecimento muito especial para uma grande amiga que me deu a sua ajuda quando pensávamos que não havia maneira: Aline Olimpio Pereira. É, claro, aos pais dela, Conceição e João, pela sua hospitalidade em troca de nada, simplesmente não tenho palavras para este ato.

A Jorge, mi maestro en el lab. Por motivarme a continuar a pesar de mis dudas. Por el fato, de ayudarme a melhorar mi Portuñol. Por demostrarme su increíble capacidad como físico, como ser humano y para crear "innumerables" nombres de la nada.

À Paty, por me acompanhar nesta longa jornada, nesta batalha que nos fez chorar (mais você do que a mim). Obrigado por ser a minha professora da paciência. Por ser a maior motivadora em ter nossos próprios dados no BEC2.

Ao Amilson, por sua companhia e amizade na última parte do meu doutorado.

Aos nossos IC's perdidos: Rodrigo (Denpendeptl), Ryan (o Americano) e Paulo.

Ao meu ex-orientador por levarme até o Vanderlei. E ao Gastão Krein novamente.

To my especial friends: Giacomo and Elenora, because without you we would not have achieved to focus our efforts and make a condensate.

A toda a equipe do grupo de óptica que me ajudaram de uma forma ou outra neste trabalho: Sergio, Kilvia, Emanuel, Gustavo (Gugs), Rodrigo, Pedro, Guilherme, Edwin, Franklin, Andrés, Stella e os IC's dos quais não lembro todos os nomes.

Ao Pessoal do Liepo: João, Leandro, Denis e André.

Aos meus colegas teóricos: Rafael, Adnilson, Edmir e André.

To colleagues and friends: Romain, Kyle, Manuel (Mexicano), and Olivier.

to readers and verifiers of this thesis: Mônica (theoretician), and Daniela (Dani my cousin).

Aos amigos meus amigos pela grande amizade Alexander, Oscar, Camilo (Sogamoso), Almeira, Alberto, Danuce, Ana María e Galia. Sempre contribuindo com um sonriso.

A mi otra parte de la familia, importante en cada momento: Paola, Adriana, Yaneth, Sebastian (Sebascho), Cesar.

A dos grandes amigas que estimo y recuerdo con cariño: Ingrid Rocío y Liliana Patricia.

A los compañeros de la UPTC y viejos amigos: Nicanor (tío Nic), Ángela, Luis y Yuber.

Ao ^{87}Rb por ser um átomo tão legal e se deixar condensar (hehehe).

Aos funcionários do Grupo de Óptica e do IFSC-USP, pelo apoio técnico, administrativo e acadêmico.

À CAPES, pelo apoio financeiro.

La verdad es mil veces más maravillosa que la misma fábula: la realidad vuela más alto que la ficción a la que sirve a veces de alimento.

-- Evaristo Fernández de San Miguel y Valledor

I am enough of an artist to draw freely upon my imagination. Imagination is more important than knowledge. Knowledge is limited. Imagination encircles the world.

-- Albert Einstein

It seems to be one of the fundamental features of nature that fundamental physical laws are described in terms of a mathematical theory of great beauty and power... One could perhaps describe the situation by saying that God is a mathematician of a very high order, and He used very advanced mathematics in constructing the universe.

-- Paul Adrien Maurice Dirac

Resumo

POVEDA-CUEVAS, F. J. *Aspectos sobre confinamento híbrido para um condensado de Bose-Einstein: pressão global e compressibilidade.* 2013. 113p. Tese (Doutorado em ciências) - Instituto de Física de São Carlos, Universidade de São Paulo, São Carlos, 2014.

A pressão e o volume não podem ser definidos corretamente em um sistema não-homogêneo. Neste trabalho, definimos variáveis macroscópicas globais para um gás confinado em uma armadilha harmônica, os quais são análogos à pressão e o volume. Um sistema ultra-frio tem variáveis termodinâmicas naturais como o número de átomos e a temperatura. Introduzimos um novo conjunto de variáveis globais conjugadas para caracterizar o sistema macroscopicamente. Construímos diferentes diagramas de fase para um gás de Bose de ^{87}Rb aprisionado em uma armadilha harmônica em termos dessas novas variáveis globais obtidas a partir das frequências da armadilha e a distribuição da densidade dos átomos. Nós construímos estes diagramas de fase, identificando os principais aspectos relacionados à transição da condensação de Bose-Einstein em um gás aprisionado. Este procedimento pode ser usado para explorar aspectos relacionados com a condensação de Bose-Einstein, tais como a compressão isotérmica relacionados com a transição de fase. Por outro lado, estas novas quantidades termodinâmicas nos permitem estudar a natureza dos fenômenos quânticos como a pressão do ponto zero relacionada ao princípio da incerteza.

Palavras-chave: Condensação de Bose-Einstein. Termodinâmica. Variáveis globais. Compresibilidade.

Abstract

POVEDA-CUEVAS, F. J. *Aspects of hybrid confinement for a Bose-Einstein condensate: global pressure and compressibility.* 2013. 113p. Thesis (Doctorate) - São Carlos Institute of Physics, Universidade de São Paulo, São Carlos, 2014.

The pressure and volume can not be defined correctly on a non-homogeneous system. In this work we define macroscopic variables for a gas confined in an harmonic trap, which are analogous to pressure and volume. An ultra-cold system has natural thermodynamic variables as number of atoms and temperature. We introduce a new set of global conjugate variables to characterize the system macroscopically. We measure different phase diagrams of a ^{87}Rb Bose gas in a harmonic trap in terms of these new global variables obtained from frequencies of trap and the density distribution of atoms. We construct these phase diagrams identifying the main features related to the Bose-Einstein condensation transition in a trapped gas. This procedure can be used to explore different aspects related to Bose-Einstein condensation, such as the isothermal compressibility related with the phase transition characteristics. On the other hand, these new thermodynamic quantities allow us to study the nature of quantum phenomena as the zero-point pressure related to the uncertainty principle.

Keywords: Bose-Einstein condensation. Thermodynamics. Global variables. Compressibility.

List of Figures

List of Tables

List of Symbols

Δa	Standard deviation of quantity a (variance)
$\Delta^2 a$	Covariance of quantity a
λ_{dB}	Thermal de Broglie wavelength
μ	Chemical potential
$\hat{\rho}$	Density matrix operator
σ_i	Gaussian width in i-direction
σ_i^0	In situ gaussian width in i-direction
Π	Pressure parameter
Π_0	Condensate pressure parameter
Π_0^Q	Zero-point pressure
Π_C	Critical pressure parameter
Ξ	Grand partition function
ω_x	Frequency x-axis
ω_y	Frequency y-axis
ω_z	Frequency z-axis
$\bar{\omega}$	Geometrical mean of frequencies
Ω	Grand potential
Ω_R	Rabi frequency
$\mathcal{V}$	Volume parameter
$\bar{a}$	Harmonic natural length
a_s	Scattering lenght
$\hat{b}$	Destruction operator
$\hat{b}^\dagger$	Creation operator
E_0	Fundamental energy state
F	Quantum atomic angular momentum number
$\hat{\mathbf{F}}$	Quantum atomic angular momentum operator
g	Coupling constant
$g_n(z)$	Bose function
$\hbar$	Planck's constant
$\hat{H}$	Hamiltonian operator
I	Nuclear angular momentum number
$\hat{\mathbf{I}}$	Nuclear angular momentum operator
k_B	Boltzmann's constant
L	Quantum angular momentum number
$\hat{\mathbf{L}}$	Quantum angular momentum operator
n	Selfvalue of number operator
$\hat{n}$	Number operator
$n(\mathbf{r})$	Density
$\hat{n}(\mathbf{r})$	Density operator
N	Atom number
$\hat{N}$	Atom number operator
m	Mass
P	Power

R_i	Thomas-Fermi radius in i-direction
R_i^0	In situ Thomas-Fermi radius in i-direction
S	Entropy
S	Spin angular momentum number
$\hat{\mathbf{S}}$	Spin angular momentum operator
t	Time
t_{exp}	Expansion time
T	Temperature
T_C	Critical Temperature
$U(\mathbf{r})$	External potential
$V(\mathbf{r}_{ij})$	Interaction potential
z	Function of fugacity

Contents

Chapter 1

Introduction

The *Bose-Einstein condensation* (BEC) is a research topic of interest that affects several areas of physics such as thermodynamics, quantum mechanics, statistical physics, the many-body theory, hydrodynamics, and others. This phenomenon occurs when particles following the Bose-Einstein statistics undergo a phase transition and occupy the lower energy state of the system below a certain *critical temperature*. This occupation is a macroscopic state that preserves certain quantum properties, for that reason is called *quantum degeneracy*. In principle, a many body system that conserves the number of particles may reach BEC.

Systems of dilute trapped atomic gases can reach BEC when they reach temperatures of 100 nK and densities of the order of $10^{13}\,\mathrm{cm}^{-3}$. The condensation in such systems requires several steps and several techniques to obtain the necessary conditions of temperature and density (2, 3, 4). Historically the gases are confined using external magnetic fields (5, 6, 7, 8), electric fields (9), or both (10). The trap potential introduces an important feature because it produces an inhomogeneous BEC system. It will be the focus of our attention throughout this work.

Until today, different atomic species have been brought to quantum degeneracy: alkaline species as ^{87}Rb (2), ^{23}Na (3), ^{7}Li(11), ^{1}H (12), ^{85}Rb (13), ^{4}He (14, 15), ^{39}K (16) , ^{41}K (17),^{131}Cs (18), non-alkaline species as ^{170}Yb (19) , ^{174}Yb (20), ^{52}Cr (21), ^{40}Ca (22), ^{84}Sr (23), ^{164}Dy (24) and ^{168}Er (25). Each species represents an advance in the field of atomic physics and ultracold gases. This systems generate possible applications (26); such as quantum simulation models, especially condensed matter (26) tests of fundamental physics through precision measurements (27, 28) and study of complex and dynamical systems (29). Other interesting non-atomic species with BEC are: the condensate of photons (30), the condensate of quasi-particles (31, 32), and liquid Helium (33). However the advantage of experimental control offered by atomic gases has become of great interest in the scientific community.

Recently, one of the focuses of the study of ultracold gases is the thermodynamic description. Several groups have focused on the determination of the thermodynamic quantities that describe these gases (34, 35, 36). Inhomogeneous thermodynamic systems,

an issue that has been investigated by our group (37, 38, 39) and others groups in recent years (40, 41, 35, 42), and it will be the objective of this thesis. First, we will investigate some of these properties in terms of global variables (1, 43), in the transition from the classical regime to quantum degenerate regime. One goal of this work is to show that we can determine an equation of state for ultracold gases *equivalent to pressure and volume*. Let us remember that the usual pressure and volume for a trapped gas are not completely well defined.

Our approach is based on the theoretical definition of a global thermodynamic variables performed by Romero-Rochín (1, 43). *Parameters* equivalent to the thermodynamic pressure and volume have similar meanings: the *pressure parameter* is closely linked to the mechanical equilibrium of the system while the *volume parameter* can be easily identified with the spatial extent occupied by ultracold sample. Based on these interpretations it was possible to define and measure various thermodynamic quantities, important over the last years, in our experimental systems.

This thesis is structured as follows: Chapter 2 explains the main objectives of this work. In Chapter 3, some we describe the theoretical fundaments that will be applied in the subsequent chapters. The Chapter 4 shows the experimental procedure to obtain ^{87}Rb BEC. It explains some important details about the confinement trap, essential for the study of thermodynamics. Chapter 5 is devoted to the determination and characterization of the extensive variable for the harmonic potential. In Chapter 6 intensive variable is determined and we shall construct the phase diagrams from this quantity. The zero-point pressure parameter is shown in Chapter 7. Finally, conclusions and perspectives of this thesis are shown in Chapter 8 and 9, respectively.

Chapter 2

Problem Statement

The manifestations of quantum phenomena are evidently below the atomic scale. When the number of particles in a single quantum states of the system is big enough, we refer to this as a macroscopic state. Interestingly, for low temperatures usually occur events called *macroscopic quantum phenomena* (**MQPh**). Several of these phenomena have been extensively studied in the last century, such as *superfluidity* and *superconductivity*. MQPh can be observed in superfluid helium (44) and in superconductors (45, 46), but also in dilute quantum gases (47, 48). The superfluids and superconductors have the ability to carry currents without dissipation.

We have a particular interest in the superfluidity effect which was discovered by Kapitza (49) and Allen (50) in liquid Helium (^{4}He) at low temperatures. Clearly the macroscopic occupation of the fundamental state (BEC) is a MQPh. The anomalous properties of superfluids with BEC were related by London in ref. (51). The superfluidity is related to BEC, but it is not identical: not all BECs can be regarded as superfluids, and not all superfluids are BECs. However, the two phenomena are certainly related. In ^{4}He it is experimentally difficult to detect a macroscopic quantum state in contrast with dilute trapped gases, where there is a dramatic change in the density of the cloud.

The superfluids are especially interesting from the standpoint of thermodynamics because they exhibit both first-order and continuous phase transitions. In these type of systems the only relevant thermodynamic variables are the temperature and the pressure. Thereby, the abrupt viscosity drop between the phases He-I and He-II was a phenomenological description very successful with this variables. In fact, several phenomena which are a consequences of the superfluid, as quantized vorticity, persistent currents, turbulence, etc. can be explained through thermohydrodynamic description (52).

Not all the exotic properties that are in liquid helium can be found in atomic gases. Although a large part of the phenomena have been tested experimentally, the similarity between the two systems is limited, since an atomic superfluid presents a different confinement system (indefinite frontier). This fact drastically changes the usual way to study superfluid from the thermodynamic standpoint. Some of the most relevant features of BEC that are not shared with liquid helium are: the system is spatially inhomogeneous,

finite and weakly interacting. In atomic gases is also possible to tune the interaction (practically impossible in ^{4}He), and observe collective modes in a harmonic trap potential.

There are ways to deal with the problem and it is possible to introduce thermodynamic variables, for example, using *local density approximation* (**LDA**) (53, 54, 55). However, LDA is limited because it does not have a global description of the system. In addition, LDA requires spatial smoothness, i.e. if we introduce defects as vortices, where the density variations are drastic, LDA no longer is useful. On these two points the thermodynamics with global variables performed by Romero-Rochin is certainly more natural (1, 43).

With the previous observations, the main contribution of this thesis, actually of our group, it is show the validity of an alternative approach, where we preserve the global properties of the sample. Based on the thermodynamics with global variables performed by Romero-Rochin (1, 43), we show a more natural way to extract various thermodynamic properties using measured parameters in the experiments. This work represents a series of ideas that begin to mature and offer us some security en route to the correct description of a trapped superfluid.

Chapter 3

Fundamentals of thermodynamics

Thermodynamics is an empirical science which does not formulate hypotheses about the structure of matter. A thermodynamic system is used to study the exchange of energy and mass with the outside by *state variables* that characterize and depend on the nature of the system itself. In particular we are interested in systems that are relaxed or at equilibrium. There are two kind of variables, intensive (scale invariant) and extensive variables, some of which are generally irrelevant to microscopic systems. The relation between these quantities is a function called the *equation of state*.

In the literature it is common to find the thermodynamic description of a quantum gas using global variables such as pressure and volume (56). These variables are well defined when we consider that the gas is contained in a box of length L, whose volume is $V = L^3$. The pressure is the effect of the force that the gas exerts on the walls of the box, which is a conjugated variable to volume. The potential produced by the box potential can be considered *homogeneous*, because it does not depend on the position.

In experiments with ultra-cold atoms, the description does not happen anymore by a box because the trapped gases are confined in magnetic, electrical, or both fields. Usually, the configuration of these fields varies continuously with the position, and due to this the gas components naturally interacting at each point in space differently, therefore the potential is called *non-homogeneous*.

That pressure and volume are not the appropriate thermodynamic quantities for a system trapped, does not mean it is not possible to find a set of global variables that represent mechanical effects of force and displacement (associated with this force) (57). Nevertheless the choice of these variables can not be arbitrary, since they must contain all information on the studied system. In this chapter we will establish and identify the most appropriate variables for a trapped gas using Romero-Rochín's formalism (1). We begin by making a description of the ideal gas, and soon after we study the importance and necessity of including the interactions. Finally with the aim to validate the globality and extensivity volume parameter we will discuss the thermodynamic limit, which is fundamental for the correct macroscopic interpretation of quantum gases trapped.

3.1 Non-interacting Bose gas

Bose-Einstein condensates are obtained by experimental techniques in confining potentials and we can do a harmonic approximation, which is usually valid for the low temperature regime, i.e., the gas is nearly in the position of equilibrium close to the minimum potential. We show an approach of the ideal gas through statistical mechanics. The effects of quantum statistics are only significant when the thermal length is comparable to the average distance between the particles (58). We will use the *grand canonical ensemble*, which turns out to be the most appropriate ensemble to describe a system of bosons near to the condensation temperature (59, 52). Thus, we consider a gas of N bosons with mass m, where the *grand partition function* is

$$\Xi = \mathrm{Tr}\left[\mathrm{e}^{-\left(\hat{H}_N - \mu\hat{N}\right)/k_B T}\right], \tag{3.1.1}$$

μ is the chemical potential, k_B is the Boltzmann's constant, and T is the temperature. $\hat{N}$ is the *total number operator* and the Hamiltonian operator is:

$$\hat{H}_N = \sum_{i=1}^{N}\left(\frac{\hat{p}_i^2}{2m} + \hat{U}\left(\mathbf{r}_i\right)\right), \tag{3.1.2}$$

which is well defined in the occupation number space $\hat{H}_N\left(\hat{\mathbf{r}}, \hat{\mathbf{p}}\right) \equiv \hat{H}_N\left(\hat{N}\right)$ and whose spectrum is ε_N. The effects of external potential $U\left(\mathbf{r}\right)$ strongly alter the thermodynamic description, and to understand this fact, we do two reasonable considerations about the potential: there must be at least a minimum and must obey the following condition: $U\left(\mathbf{r}\right) \to \infty$ as $r \to \infty$ (60). A harmonic potential satisfies these two conditions and also happens to be a good approximation for trapped gases, this does not mean that it is not possible to study ultracold gases in other kinds of traps (60). Our group and collaborators have extensively explored systems that can be considered in the harmonic approximation potential (37). So we make a direct connection to thermodynamics with a microscopic system, using the *grand thermodymical potential*:

$$\Omega\left(\mu, T, \mathcal{V}\right) = -k_B T \ln \Xi, \tag{3.1.3}$$

$\mathcal{V}$ is a global extensive quantity which comes from configuration space. We define the *density matrix* for the grand canonical ensemble

$$\hat{\rho} = \frac{\mathrm{e}^{-\left(\hat{H}_N - \mu\hat{N}\right)/k_B T}}{\mathrm{Tr}\left[\mathrm{e}^{-\left(\hat{H}_N - \mu\hat{N}\right)/k_B T}\right]}. \tag{3.1.4}$$

The grand canonical ensemble describes an open system that interchanges particles and energy[1], in this form we can calculate some thermodynamic quantities from the eq. (3.1.1) with $\Omega\left(\mu, T, \mathcal{V}\right) \equiv \Omega$:

$$N = \mathrm{Tr}\left[\hat{N}\hat{\rho}\right] = -\left(\frac{\partial\Omega}{\partial\mu}\right)_{T,\mathcal{V}}, \tag{3.1.5}$$

$$S = \mathrm{Tr}\left[\hat{\rho}\ln\hat{\rho}\right] = -\left(\frac{\partial\Omega}{\partial T}\right)_{\mu,\mathcal{V}}, \tag{3.1.6}$$

$$E = \mathrm{Tr}\left[\hat{H}\hat{\rho}\right] = TS + \mu N + \Omega, \tag{3.1.7}$$

$$\Pi = -\left(\frac{\partial\Omega}{\partial\mathcal{V}}\right)_{\mu,T}, \tag{3.1.8}$$

which are the number of particles, entropy, and internal energy, respectively [2]. Usually, the pressure and volume are the combined thermodynamic quantities appearing at last, but it is possible to have other quantities such as magnetization and magnetic field, polarization and electric field, etc. Π and $\mathcal{V}$ are called generalized variables, and their choice can not be arbitrary, since it must contain all the information that will be studied in the system. For a trapped gas in an external potential Π and $\mathcal{V}$ are analogous to the mechanical effects of force and displacement associated with this force (57).

In the search for an appropriate description, Romero-Rochín in the ref. (1) conveniently studied an ideal gas confined harmonically where it can be calculated "analytically" the grand thermodynamic potential, which in principle should be the product of two conjugate variables (43). Particles confined in a 3D harmonic potential have a Hamiltonian

$$\hat{H}_N = \frac{1}{2m}\sum_{i=1}^{N}\left\{\hat{p}_i^2 + m^2\left(\omega_x^2\hat{x}_i^2 + \omega_y^2\hat{y}_i^2 + \omega_z^2\hat{z}_i^2\right)\right\}. \tag{3.1.9}$$

where $\hat{\mathbf{p}}_i = (\hat{p}_i^x, \hat{p}_i^y, \hat{p}_i^z)$, $\hat{\mathbf{r}}_i = (\hat{x}_i, \hat{y}_i, \hat{z}_i)$. i labels the number of particles in the eq. (3.1.2). We can rewrite this Hamiltonian in second quantization using the number occupation representation

$$\hat{H}_N = \sum_{i=1}^{N}\hbar\left[\omega_x\left(\hat{n}_i^x + \frac{1}{2}\right) + \omega_y\left(\hat{n}_i^y + \frac{1}{2}\right) + \omega_z\left(\hat{n}_i^z + \frac{1}{2}\right)\right]. \tag{3.1.10}$$

Thus, the grand thermodynamic potential can be obtained from eq.(3.1.1)

$$\Omega\left(\mu, T, \mathcal{V}\right) = -k_B T\sum_{n_x n_y n_z}\ln\left[1 - z\mathrm{e}^{-\hbar(\omega_x n_x + \omega_y n_y + \omega_z n_z)/k_B T - E_0/k_B T}\right]. \tag{3.1.11}$$

[1] There is a constraint for the grand canonical ensemble which says that the total number of particles is the sum of the number of particles of the k-th energy level, i.e. $N = \sum_k n_k$.

[2] In this document we will use indiscriminately the notation to mean values $\left\langle\hat{O}\right\rangle \equiv O$, unless it is necessary to do some specification.

where $z = \mathrm{e}^{\mu/k_BT}$ is the *fugacity*. $E_0 = \frac{1}{2}\hbar\left(\omega_x + \omega_y + \omega_z\right)$ is the zero-point energy of fundamental state of the potential. The selfvalues of number operators are $n_x, n_y, n_z = 0, 1, 2, ...$

We can get easily two quantities N and Π

$$N \equiv \sum_{\varepsilon} f_{BE}\left(\varepsilon, \mu\right), \tag{3.1.12}$$

$$\frac{\Pi\mathcal{V}}{k_BT} \equiv -\sum_{\varepsilon} \ln\left[1 - z\mathrm{e}^{-E_0/k_BT}\mathrm{e}^{-\varepsilon/k_BT}\right]. \tag{3.1.13}$$

When N bosons distributed over the various quantum states; the occupation number is proportional to the *Bose-Einstein distribution*

$$f_{BE}\left(\varepsilon, \mu\right) = \frac{1}{\exp\left[\left(\varepsilon + E_0 - \mu\right)/k_BT\right] - 1} = \frac{z'}{\mathrm{e}^{\varepsilon/k_BT} - z'}, \tag{3.1.14}$$

where the energy level is $\varepsilon \equiv \varepsilon\left(n_x, n_y, n_z\right)$. We use the notation $z' = z\mathrm{e}^{-E_0/k_BT} = \mathrm{e}^{(\mu - E_0)/k_BT}$. Commonly we can separate the contribution of the ground state in the expressions for Π and N

$$\frac{\Pi\mathcal{V}}{k_BT} \equiv -\ln\left[1 - z'\right] - \sum_{\varepsilon}^{\bullet} \ln\left[1 - z'\mathrm{e}^{-\varepsilon/k_BT}\right], \tag{3.1.15}$$

$$N = \frac{z'}{1 - z'} + \sum_{\varepsilon}^{\bullet} f_{BE}\left(\varepsilon, \mu\right), \tag{3.1.16}$$

the symbol $\sum_{\varepsilon}^{\bullet}$ indicates that the ground state is neglected.

Before proceeding the summations to the integrals we make a brief mathematical review. We can use a coordinate transformation from the cartesian coordiantes to pseudo-spherical coordinates

$$\begin{aligned} \omega_x x &= \omega r \sin\theta \cos\varphi, \\ \omega_y y &= \omega r \sin\theta \sin\varphi, \\ \omega_z z &= \omega r \cos\theta. \end{aligned}$$

Such that there is a constraint as a sphere: $\omega^2 r^2 = \omega_x^2 x^2 + \omega_y^2 y^2 + \omega_z^2 z^2$. The determinant of Jacobian matrix is

$$\left|J\left(r, \theta, \varphi\right)\right| = \begin{vmatrix} \frac{\partial x}{\partial r} & \frac{\partial x}{\partial \theta} & \frac{\partial x}{\partial \varphi} \\ \frac{\partial y}{\partial r} & \frac{\partial y}{\partial \theta} & \frac{\partial y}{\partial \varphi} \\ \frac{\partial z}{\partial r} & \frac{\partial z}{\partial \theta} & \frac{\partial z}{\partial \varphi} \end{vmatrix} = \frac{\omega^3}{\omega_x\omega_y\omega_z} r^2 \sin\theta.$$

In this form we simply choose $\omega^3 = \omega_x\omega_y\omega_z$, so that $\left|J\left(r, \theta, \varphi\right)\right|$ is identical to Jacobian of

the conventional spherical coordinates. Thus

$$\bar{\omega} = \left(\omega_x \omega_y \omega_z\right)^{1/3}, \tag{3.1.17}$$

which corresponds to *geometric mean* of the trap frequencies. Rewriting the sphere as

$$\bar{\omega}^2 r^2 = \omega_x^2 x^2 + \omega_y^2 y^2 + \omega_z^2 z^2, \tag{3.1.18}$$

which will be a useful relationship for upcoming deductions.

We consider the Thomas-Fermi semi-classical approximation which is valid considering that the number of particles in the system is large and the level spacing is much smaller than the average kinetic energy of the particles. Then, we can replace sums by integrals, such that the density of states in phase space for the harmonic oscillator is

$$\sum_{\varepsilon} \equiv \frac{1}{h^3} \int d^3r \int d^3p = \frac{4\pi \left(2m\right)^{3/2}}{h^3} \int_0^\infty d\varepsilon \int_0^\infty dr\, r^2 \sqrt{\varepsilon - \frac{1}{2} m\bar{\omega}^2 r^2} = \int_0^\infty d\varepsilon\, \rho\left(\varepsilon\right),$$

a volume which is in the energy range ε and $\varepsilon + d\varepsilon$. In this form

$$\rho\left(\varepsilon\right) = \frac{\varepsilon^2}{2\hbar^3 \bar{\omega}^3} \tag{3.1.19}$$

depends of the geometric mean.

Now we can express explicitly Π and N in integral forms, neglecting the effects of the ground state ($E_0 = 0$)

$$N = N_0 + \frac{k_B^3 T^3}{2\hbar^3 \bar{\omega}^3} \int_0^\infty d\left(\varepsilon / k_B T\right)\, \frac{\left(\varepsilon / k_B T\right)^2}{\mathrm{e}^{-\varepsilon / k_B T} / z - 1} \tag{3.1.20}$$

$$\Pi = \Pi_0 - \frac{k_B^4 T^4}{2\hbar^3 \bar{\omega}^3 \mathcal{V}} \int_0^\infty d\left(\varepsilon / k_B T\right)\, \left(\varepsilon / k_B T\right)^2 \ln\left[1 - z\mathrm{e}^{-\varepsilon / k_B T}\right], \tag{3.1.21}$$

where

$$N_0 = \frac{z}{1 - z} \tag{3.1.22}$$

is the number of particles in the fundamental state, and

$$\Pi_0 = -\frac{k_B T}{\mathcal{V}} \ln\left[1 - z\right] \tag{3.1.23}$$

is the pressure of the fundamental state. N is an explicit function of μ and the integral is a maximum value in $\mu = 0$. Typically the term $\ln\left[1 - z\right]$ can be neglected compared with the second term of the right part of the parameter Π.

The mean size of the system is restricted by the size of the effective potential, i.e. the natural mean length $\bar{a} = \sqrt{\frac{\hbar}{m\bar{\omega}}}$. Thus, $\bar{a}$ is related to the effective volume of the

sample, which is spatially distributed. Using the *thermal de Broglie length* $\lambda_{dB} = \sqrt{\frac{2\pi\hbar^2}{mk_BT}}$, we can establish the region where quantum effects start to be relevant to the gas that is:

$$\frac{k_B^3T^3}{\hbar^3\bar{\omega}^3} = (2\pi)^3\left(\frac{\bar{a}^3}{\lambda_{dB}^3}\right)^2 \ll 1.$$

Analogously to the gas in the box where $\frac{V}{\lambda_{dB}^3} \ll 1$. Naturally, the ground state is highly localized in the trap center, the condensation process results in a dramatic increase of density in the center of the cloud. Note that this density increase is a feature of the inhomogeneous gas. In homogeneous gases the density is constant and BEC manifests itself only in the momentum space, the effects of finite size in the box are studied in the ref. (61).

We rewrite the eq. (3.1.11) in terms of density in phase space

$$\Omega = \frac{k_BT}{2\hbar^3\bar{\omega}^3}\int_0^\infty d\varepsilon\,\varepsilon^2\ln\left[1 - z\mathrm{e}^{-\varepsilon/k_BT}\right], \tag{3.1.24}$$

Expanding the logarithm in a Taylor series and integrating term by term, we obtain a closed form for Ω

$$\Omega = -\frac{k_B^4T^4}{\hbar^3\bar{\omega}^3}\left[z + \frac{1}{2^4}z^2 + \frac{1}{3^4}z^3...\right] = -\frac{k_B^4T^4}{\hbar^3\bar{\omega}^3}\sum_{j=1}^{\infty}\frac{z^j}{j^4}.$$

On the other hand, we know that the power series,

$$g_n(z) = \sum_{j=1}^{\infty}\frac{z^j}{j^n}$$

is a Bose function defined as[3]:

$$\Omega = -\frac{k_B^4T^4}{\hbar^3\bar{\omega}^3}g_4(z). \tag{3.1.25}$$

The grand thermodynamic potential which is a consequence of the first thermodynamic law by definition is

$$\Omega = E - TS - \mu N. \tag{3.1.26}$$

Now that we know the functional form of Ω we can easily derive the thermodynamic relations starting from eqs. (3.1.5-3.1.7)

$$N = \left(\frac{\partial\Omega}{\partial\mu}\right)_T = \frac{k_B^3T^3}{\hbar^3\bar{\omega}^3}g_3(z), \tag{3.1.27}$$

$$S = \left(\frac{\partial\Omega}{\partial T}\right)_{\mathcal{V},\mu} = \frac{k_B^4T^3}{\hbar^3\bar{\omega}^3}\left[4g_4(z) - (\ln z)\,g_3(z)\right], \tag{3.1.28}$$

[3] $g_n(z)$ is a form of the polylogarithm function

$$E = TS + \mu N + \Omega = \frac{3k_B^4 T^4}{\hbar^3 \bar{\omega}^3} g_4(z). \tag{3.1.29}$$

We know that scale transformation as the quantities E, N, and S are proportional to the amount of material in the system, therefore they are extensive properties. Below we will show how in the harmonic confinement case we identify the equivalent extensive and intensive properties using the first law of thermodynamics. The study of these parameters as extensive and intensives quantities are well discussed in the references (43, 1).

Thus, based on the first law we can identify the extensive variable and the intensive variable for a harmonic potential, since:

$$\Omega(\mu, T, \mathcal{V}) = -\Pi\mathcal{V}, \tag{3.1.30}$$

where we identify

$$\Pi = \frac{k_B^4 T^4}{\hbar^3} g_4(z); \quad \mathcal{V} = \frac{1}{\bar{\omega}^3}. \tag{3.1.31}$$

Π and $\mathcal{V}$ are conjugate macroscopic quantities. $\mathcal{V}$ is an extensive variable with units inverse of frequency cubed, which we will call *volume parameter*. On the other hand, Π or *pressure parameter* is a intensive variable with units of energy times frequency cubed. In this form, the product of this variables preserves units of energy for the grand potential. Π is closely related to mechanical equilibrium of the system while the volume parameter can be easily identified with the spatial extent of the gas (1).

Using the energy E and the pressure parameter Π in the eq. (3.1.29) we obtain the relation:

$$E = 3\Pi\mathcal{V} \tag{3.1.32}$$

this equation is a fundamental relation for ideal gases in a harmonic potential known as *equation of state*. Comparing with the homogeneous case we have 3/2 factor for the usual variables of volume and pressure, i.e. $E_{box} = \frac{3}{2}PV$.

Now we can leave evidences of the macroscopic occupation of the ground state simply rewriting eq. (3.1.20)

$$N = N_0 + \frac{k_B^3 T^3}{\hbar^3 \bar{\omega}^3} g_3(z) \tag{3.1.33}$$

The critical temperature is reached when $z' = 1$, therefore we can obtain the relation between critical temperature and the number of atoms

$$T_C^3 = \frac{\hbar^3}{k_B^3 g_3(1)} \bar{\omega}^3 N. \tag{3.1.34}$$

which was calculated by first time by Bagnato, et al. in Ref. (62, 63). When we do $z = 1$ the Bose function is the same Riemann Zeta function, $g_3(1) \equiv \zeta(3) \approx 1.202$. T_C corresponds to the temperature where it begins to manifest the macroscopic occupation

of the ground state. In this form, we have

$$\frac{N_0}{N} = 1 - \left(\frac{T}{T_C}\right)^3, \tag{3.1.35}$$

which is called as the *condensate fraction* of a harmonically trapped gas. The eq. (3.1.35) shows the coexistence of the condensed state and excited states, two phases in thermal equilibrium.

The pressure has a critical value in the transition from the absence of condensation to coexistence of two phases, using the eqs. (3.1.25) and (3.1.27) we obtain

$$\Pi_C = \frac{g_4(1)}{\hbar^3} k_B^4 T_C^4, \tag{3.1.36}$$

which we call the *critical pressure*.

Somewhat tedious calculations lead to the general variances and covariances of the model (58) from eqs. (3.1.5-3.1.18)

$$\Delta^2 N = \left\langle \hat{N}^2 \right\rangle - \left\langle \hat{N} \right\rangle^2 = k_B T \left(\frac{\partial N}{\partial \mu}\right)_{T,\mathcal{V}}, \tag{3.1.37}$$

$$\Delta^2 E = \left\langle \hat{H}^2 \right\rangle - \left\langle \hat{H} \right\rangle^2 = k_B T^2 \left(\frac{\partial E}{\partial T}\right)_{\mu,\mathcal{V}} + \mu k_B T \left(\frac{\partial E}{\partial \mu}\right)_{T,\mathcal{V}}, \tag{3.1.38}$$

$$\Delta^2 (EN) = \left\langle \hat{N}\hat{H} \right\rangle - \left\langle \hat{N} \right\rangle \left\langle \hat{H} \right\rangle = k_B T \left(\frac{\partial E}{\partial \mu}\right)_{T,\mathcal{V}}, \tag{3.1.39}$$

We shall return later to discuss a bit about the fluctuations of the system from the point of view of statistical mechanics and its connection with mechanical response variables in thermodynamics.

3.2 Weakly-interacting Bose gas

By studying real gases we need to consider the interaction of particles that compose them. In fact, for ultracold samples, it is necessary to consider the interactions and the internal degrees of freedom of the system, which in the end shall fix two quantities: the temperature and density of the sample. Now, the Hamiltonian for N bosons is

$$\hat{H}_N = \sum_{i=1}^{N} \left(\frac{\hat{p}_i^2}{2m} + \hat{U}(\mathbf{r}_i) \right) + \sum_{i<j=1}^{N} \hat{V}(\mathbf{r}_{ij}) \tag{3.2.1}$$

$\hat{V}(\mathbf{r}_{ij})$ is the interaction potential between the particles, we can see that when $\hat{V}(\mathbf{r}_{ij}) = 0$ reproduces the *ideal gas* (eq. 3.1.2).

Initially, we start from the assumption that the particles of the gas can be considered as hard spheres of radius a_s, where a_s is known as the *scattering length*. The information about the interaction between particles is introduced in this parameter. If collisions are at low energy the scattering is dominated by s-wave collisions (64). The effective interaction between two atoms at $\mathbf{r}$ and $\mathbf{r}'$ positions, commonly stated in the form

$$\int d^3r' \; V_{eff}(\mathbf{r}', \mathbf{r}) = g \int d^3r' \; \delta\left(\mathbf{r} - \mathbf{r}'\right) = g = \frac{4\pi\hbar^2}{m} a_s, \tag{3.2.2}$$

where V_{eff} is an *effective contact potential*.

3.2.1 Approximation for $T \to 0$

We can build a many-body Hamiltonian for N interacting bosons:

$$\begin{aligned} \hat{H} = \int d^3r \; \hat{\psi}^\dagger\left(\mathbf{r}, t\right) \left(-\frac{\hbar^2}{2m}\nabla^2 + U\left(\mathbf{r}, t\right) \right) \hat{\psi}\left(\mathbf{r}, t\right) \\ + \frac{1}{2} \int d^3r \int d^3r' \; \hat{\psi}^\dagger\left(\mathbf{r}, t\right) \hat{\psi}^\dagger\left(\mathbf{r}', t\right) V_{eff} \hat{\psi}\left(\mathbf{r}, t\right) \hat{\psi}\left(\mathbf{r}', t\right) \end{aligned} \tag{3.2.3}$$

where $\hat{\psi}^\dagger\left(\mathbf{r}\right)$ and $\hat{\psi}\left(\mathbf{r}\right)$ are creation and destruction field operators, respectively. These operators represent fields that obey the canonical commutation relations, given by:

$$\begin{aligned} \left[\hat{\psi}\left(\mathbf{r}, t\right), \hat{\psi}^\dagger\left(\mathbf{r}', t\right)\right] = \delta(\mathbf{r}' - \mathbf{r}), \\ \left[\hat{\psi}^\dagger\left(\mathbf{r}, t\right), \hat{\psi}^\dagger\left(\mathbf{r}', t\right)\right] = \left[\hat{\psi}\left(\mathbf{r}, t\right), \hat{\psi}\left(\mathbf{r}', t\right)\right] = 0. \end{aligned} \tag{3.2.4}$$

Using a Heisenberg's equation of motion:

$$i\hbar \frac{\partial \hat{\psi}\left(\mathbf{r}, t\right)}{\partial t} = \left[\hat{\psi}\left(\mathbf{r}, t\right), \hat{K}\right] = \left[\hat{\psi}\left(\mathbf{r}, t\right), \hat{H} - \mu\hat{N}\right] \tag{3.2.5}$$

where $\hat{K} = \hat{H} - \mu\hat{N}$ is called grand-canonical operator, operator $\hat{H}$ and $\hat{N}$ commute (65). Now, the total number operator is defined as

$$\hat{N} = \int d^3r \, \hat{\psi}^\dagger\left(\mathbf{r}\right) \hat{\psi}\left(\mathbf{r}\right) = \int d^3r \, \hat{n}\left(\mathbf{r}\right) \tag{3.2.6}$$

where $\hat{n}\left(\mathbf{r}\right)$ is the *density operator*. The equation of motion is explicitly:

$$i\hbar \frac{\partial \hat{\psi}\left(\mathbf{r}, t\right)}{\partial t} = \left(-\frac{\hbar^2}{2m}\nabla^2 + U\left(\mathbf{r}\right) - \mu \right) \hat{\psi}\left(\mathbf{r}, t\right) + g\hat{\psi}^\dagger\left(\mathbf{r}, t\right) \hat{\psi}\left(\mathbf{r}, t\right) \hat{\psi}\left(\mathbf{r}, t\right). \tag{3.2.7}$$

We assume that the external potential is independent of time, i.e. $U(\mathbf{r},t) \equiv U(\mathbf{r})$. We can now express the field operators on an another base

$$\hat{\psi}(\mathbf{r},t) = \sum_i \Phi_i(\mathbf{r},t)\,\hat{b}_i, \quad \hat{\psi}^\dagger(\mathbf{r},t) = \sum_i \Phi_i^*(\mathbf{r},t)\,\hat{b}_i^\dagger. \tag{3.2.8}$$

The creation and destruction bosonic operators $\hat{b}_i^\dagger$ and $\hat{b}_i$ satisfy canonical commutation relations similar to eq. (3.2.4). Consider the system of bosons is very close to zero temperature, so that they tend to occupy the lower energy state or the ground state of the system ($i = 0$). Using this approach, we can take the expansion in eq.(3.2.8) as

$$\hat{\psi}(\mathbf{r},t) \simeq \Phi_0(\mathbf{r},t)\,\hat{b}_0, \quad \hat{\psi}^\dagger(\mathbf{r},t) \simeq \Phi_0^*(\mathbf{r},t)\,\hat{b}_0^\dagger. \tag{3.2.9}$$

This approach is also called *mean-field approximation*. Substituting into the equation of motion, we have

$$i\hbar\frac{\partial\Phi_0(\mathbf{r},t)}{\partial t} = \left(-\frac{\hbar^2}{2m}\nabla^2 + U(\mathbf{r}) - \mu\right)\Phi_0(\mathbf{r},t) + g\left|\Phi_0(\mathbf{r},t)\right|^2\Phi_0(\mathbf{r},t). \tag{3.2.10}$$

This equation of motion corresponds to the *time dependent Gross-Pitaevskii equation*. On the other hand, we can use the ansatz $\Phi_0(\mathbf{r},t) = \phi_0(\mathbf{r})$ for stationary problems, and we obtain

$$\mu\phi_0(\mathbf{r}) = \left(-\frac{\hbar^2}{2m}\nabla^2 + U(\mathbf{r})\right)\phi_0(\mathbf{r}) + g\left|\phi_0(\mathbf{r})\right|^2\phi_0(\mathbf{r}). \tag{3.2.11}$$

independent time Gross-Pitaevskii equation (**GPE**). The two differential equations above describe the dynamics of the wave function for the ground state, and will be a valid approximation for a gas with $T \to 0$, i.e. for temperatures far below the critical temperature, T_C. From the eq. (3.2.6) we can see that the term $|\phi_0(\mathbf{r})|^2$ is related to the density. The term $g|\phi_0(\mathbf{r})|^2$ represents an effective potential whose signal depends on the constant a_s. If the scattering lenght is repulsive ($a_s > 0$), the effective energy increases with the density. Otherwise, if the scattering lenght is attractive ($a_s < 0$) a collapse of the condensate can occur (4, 11).

For a large number of condensed atoms, the repulsive interactions lead to a lower density in the cloud, since the atoms are pushed outwards. As a consequence, the quantum pressure has a small influence and only contributes near the boundary surface of the condensate, i.e. the interaction term dominates the dynamics. In this case the GPE gives the solution

$$|\phi_0(\mathbf{r})|^2 \equiv n_q(\mathbf{r}) = \frac{1}{g}\left\{\mu - U(\mathbf{r})\right\}. \tag{3.2.12}$$

In this form, when the quantum pressure can be ignored in the region where $\mu \leq U(\mathbf{r})$, and $n_q(\mathbf{r}) = 0$ outside this region, we have the *Thomas-Fermi approximation* (**TFA**). TFA can only be applied, when $\phi_0(\mathbf{r})$ varies slowly, this means the TFA fails near the

cloud surface. On the other hand, with the boundary of the cloud given by $\mu = U(\mathbf{r})$, and the normalization of the density $N = \int d^3r\, n(\mathbf{r})$, the chemical potential is

$$\mu = \hbar\bar{\omega}\left(\frac{15Na_s}{\bar{a}}\right)^{2/5}, \tag{3.2.13}$$

which is a function of the atom number. From this relation and (3.2.12), the size for each direction of the condensate in a harmonic trap becomes:

$$R_i = \bar{a}\frac{\bar{\omega}}{\omega_i}\left(\frac{15Na_s}{\bar{a}}\right)^{2/5} = \frac{\bar{\omega}^{3/5}}{\omega_i}\left(\frac{15\hbar^2 a_s}{m^2}N\right)^{1/5}, \quad i = x, y, z. \tag{3.2.14}$$

the semi-axes R_i's is known as *Thomas-Fermi radii*. The aspect ratio is given by the inverse ratio of the trap frequencies:

$$\frac{R_i}{R_j} = \frac{\omega_j}{\omega_i}, \quad i, j = x, y, z. \tag{3.2.15}$$

This relation shows that all the interaction energy is transformed into kinetic energy upon release, and anisotropy expansion is thereby further increased (47, 48). This means that the cloud expands faster in the direction of stronger confinement.

3.2.2 Volume, pressure and density

As shown above for the case of an ideal gas, Π and $\mathcal{V}$, are thermodynamic variables, which in principle are the macroscopic parameters that characterize a inhomogeneous system properly. Once identified these variables is pertinent to consider the fluid with interactions and establish a direct connection between the pressure parameter and the grand potential. Again, we start with the grand partition function defined as:

$$\Xi = \mathrm{Tr}\left[\mathrm{e}^{-\hat{K}/k_BT}\right], \tag{3.2.16}$$

the trace of the grand canonical operator $\hat{K} = \hat{H}_N - \mu\hat{N}$. Using the N-body Hamiltonian (3.2.1) and the variable transformation (3.1.18), we have

$$\Xi = \mathrm{Tr}\left[\exp\left[-\frac{1}{k_BT}\left\{\sum_{i=1}^{N}\frac{\hat{p}_i^2}{2m} + \sum_{i=1}^{N}\frac{1}{2}m\mathcal{V}^{-2/3}\hat{r}_i^2 + \sum_{i<j=1}^{N}\hat{V}(\mathbf{r}_{ij}) - \mu\hat{N}\right\}\right]\right]. \tag{3.2.17}$$

We can see that the harmonic external potential was conveniently rewritten in terms of the volume parameter $\mathcal{V}$. Now, we can use the general expression (3.1.8) and calculate

explicity the pressure parameter:

$$\Pi = -\left(\frac{\partial\Omega}{\partial\mathcal{V}}\right)_{\mu,T} = \frac{2}{3\mathcal{V}}\frac{1}{\Xi}\mathrm{Tr}\left[\sum_{i=1}^{N}\frac{1}{2}m\mathcal{V}^{-2/3}\hat{r}_i^2\mathrm{e}^{-\hat{K}/k_BT}\right].$$

Now we can use the next identity

$$\sum_{i=1}^{N}\frac{1}{2}m\bar{\omega}^2\hat{r}_i^2 = \int d^3r\,\frac{1}{2}m\bar{\omega}^2r^2\sum_{i}^{N}\delta\left(\mathbf{r}-\mathbf{r}_i\right). \tag{3.2.18}$$

In this form

$$\Pi = \frac{2}{3\mathcal{V}}\int d^3r\,\frac{1}{2}m\bar{\omega}^2r^2\frac{1}{\Xi}\mathrm{Tr}\left[\sum_{i}^{N}\delta\left(\mathbf{r}-\mathbf{r}_i\right)\mathrm{e}^{-\hat{K}/k_BT}\right].$$

We identify the particle density as

$$n\left(\mathbf{r}\right) = \left\langle\hat{n}\left(\mathbf{r}\right)\right\rangle = \frac{1}{\Xi}\mathrm{Tr}\left[\sum_{i}^{N}\delta\left(\mathbf{r}-\mathbf{r}_i\right)\mathrm{e}^{-\hat{K}/k_BT}\right]. \tag{3.2.19}$$

Finally we have

$$\Pi = \frac{m}{3\mathcal{V}}\int d^3r\,n\left(\mathbf{r}\right)\left(\omega_x^2x^2+\omega_y^2y^2+\omega_z^2z^2\right), \tag{3.2.20}$$

in this form the pressure parameter for a weakly interacting gas is a function of the density and the external potential. According to Romero-Rochín, Π depends entirely of the external potential (60). In this way, we can see that frequencies and volume parameter can be determined experimentally and regardless of the number of atoms and temperature.

In the expression (3.2.20) the pressure is not uniform due to the force exerted by the confinement trap, and the density has a spatial distribution. In an experiment that use diagnostic imaging becomes feasible to determine $n\left(\mathbf{r}\right)$. For equilibrium models it is a simple matter to show that position-dependent systems are determined by density ($\left\langle\hat{n}\left(\mathbf{r}\right)\right\rangle \equiv n\left(\mathbf{r}\right)$) (66, 67). It is worth noting that this density corresponds to the density of the sample inside the trap when $n\left(\mathbf{r}\right)$ reached thermal equilibrium.

Experimentally, we search for measurable quantities describing the response to various external stimuli. These observables are the so-called response functions, or susceptibilities. One of the most important quantities is the *isothermal compressibility*, which is especially of interest in systems with a quantum component (64). One of the most interesting advantages of obtaining an expression with such features as eq. is the possibility of a direct analysis of isothermal compressibility. This topic will be boarded in a later chapter.

3.3 Thermodynamic limit

In a usual thermodynamic bulk system the intensive properties are independent of surface, size, geometry, and volume effects. This means that the determination of macroscopic observables are reduced to a mathematical problem, from the viewpoint of statistical mechanics, where the partition function is converted from summations to integrals. A system with a considerable number of particles (a large system) has a essencially continous energy espectrum because the level spacing is very small. In this way, the right path is to identify correctly the density of states $\rho(\varepsilon)$. This can be done by invoking the so-called *thermodynamic limit*:

$$N \to \infty, \;\; V \to \infty, \;\; \frac{N}{V} \to \text{const.},$$

where N is the number of particles and V the volume. In this case the density $n \equiv N/V$ is finite. The thermodynamic limit ensures the extensivity of quantities and entropy, free energy, etc.

Having a large system does not mean that we can apply the thermodynamic limit directly. A system with a rotating fluid and with the ability to reach BEC were studied by Widom in ref. (68, 69). Consider a rotating bucket: an ideal gas contained in a circular-cylindrical vessel of radius R and height L rotating about its symmetry axis with uniform angular speed $\Omega = v/R$. Intuitively we could consider the thermodynamic limit as $L \to \infty$ for fixed Ω. But a general requirement imposed on the infinite limit by the mathematical processes it is that the ratio of surface area to volume vanishes in the limit (58). As a consequence the appropriate description in the thermodynamic limit: If $L \to \infty$ and $R \to \infty$, we require $\Omega \to 0$, such that $\Omega R \to$ const. i.e. the velocity remains finite. Fundamentally, all spatial dimensions must be scaled appropriately so that the scale no distort the physics.

The thermodynamic limit for an ideal gas trapped in an external harmonic potential depends essentially on the number of particles and the geometric mean of the frequencies (70, 48). We can make a combination such that the product $\bar{\omega}^3 N$ is finite, which is completely analogous to the bulk system. This means that the thermodynamic limit is given as follows

$$N \to \infty, \;\; \bar{\omega}^3 \to 0, \;\; \mathcal{V} \to \infty, \;\; \frac{N}{\mathcal{V}} \to \text{const.}$$

The volume parameter is naturally introduced.

Let us consider a physical situation a thermodynamical system with a given T and $N\mathcal{V}^{-1} = C_1$. If we consider another system with the same T and $N'\mathcal{V}'^{-1} = C_1$, both systems are in the same thermodynamic state even if $N \neq N'$ and $\mathcal{V} \neq \mathcal{V}'$. This can be seen directly using the critical temperature, $k_B T_C = 0.94\bar{\omega}N^{1/3}$(62, 63): if we increase

the number of atoms and we want to keep T_C constant, necessarily have to increase the volume parameter $\mathcal{V}$.

However we have a real system, the thermodynamic limit is never reached (mathematically), because the number of atoms that can be trapped and condensed is not infinite. In addition, the system size is finite for an external harmonic trap. The regime of applicability of this thermodynamic treatment is an important issue, since typical systems consist of cold atoms with 10^4 to 10^6 atoms and geometric frequencies of the order of $\bar{\omega} = 2\pi \times (100\text{Hz})$. If N is a macroscopic quantity $\bar{\omega}$ should become small enough to accommodate many particles (71). Energetically, it means that $\hbar\bar{\omega}$ should be smaller than any other energy scale in the problem, i.e. the energy scale of an atomic transition (71). The corrections between the thermodynamic limit and taking into account the finite size of the gas (72, 73) for an ideal Bose gas are however only a small difference

Chapter 4

Experimental setup

In this chapter we explain briefly the sequence of the experimental process for BEC, which will be detailed over the next few sections. A deeper description of this experimental setup can be found in the refs. (74, 75). The logical sequence of this chapter is the following: Initially we capture $\sim 10^9$ atoms in a *magneto-optical trap* (**MOT**) at a temperature of tens of μK (76) with a pressure arround of $\sim 10^{-11}$Torr. Once loaded the MOT with a sufficiently large number, they are transferred to a purely magnetic trap by switching off the light and increasing the gradient. This trap is called *magnetic quadrupole trap* (**MT**) which is made a first step of evaporation and cooling by radiofrequency waves. After this process, the atoms are partially transferred to *optical dipole trap* (**OT**), in a configuration known as *hybrid trap* (**HT**), where there is an optical evaporation to achieve quantum degeneracy (10). Worthwhile to say that this machine is the second generation of experiments to condense successfully implemented in our laboratory.

4.1 Vaccum system

The experiment possesses a vacuum system with two chambers connected by a thin glass transfer tube with a length of 50 cm and an inner diameter of 4 mm, in a configuration known as a double MOT (77) (Fig. 4.1.1). The region of the first cell is pumped by an ion pump of $55\,\mathrm{l\cdot s^{-1}}$ and the second one by a ion pump of $300\,\mathrm{l\cdot s^{-1}}$. The MOT first chamber (**MOT1**) consists of a rectangular glass cell with dimensions $150 \times 30 \times 30\,\mathrm{mm^3}$. The MOT second chamber (**MOT2**) is a quartz cell from Hellma company with dimensions $150 \times 30 \times 30\,\mathrm{mm^3}$, which has a high optical quality, which is important and necessary to do diagnostic images of atoms.

The first cell has a rubidium dispenser (78), which passes an electrical current to produce a vapor, so that it is possible to perform MOT1 with about 10^9 atoms. Due to the background vapor, the pressure in the first chamber is too high the order of 10^{-9} Torr, this means that the life of the trap is too short to observe condensation. For this reason, the atoms of the first cell are transferred to a second one where the vacuum is about two orders of magnitude lower at around 10^{-11} Torr. The atoms of MOT2 shall be subjected

to other various procedures for achieving quantum regime, this can lead to 50 s (or more) and therefore it is necessary to have such low pressures.

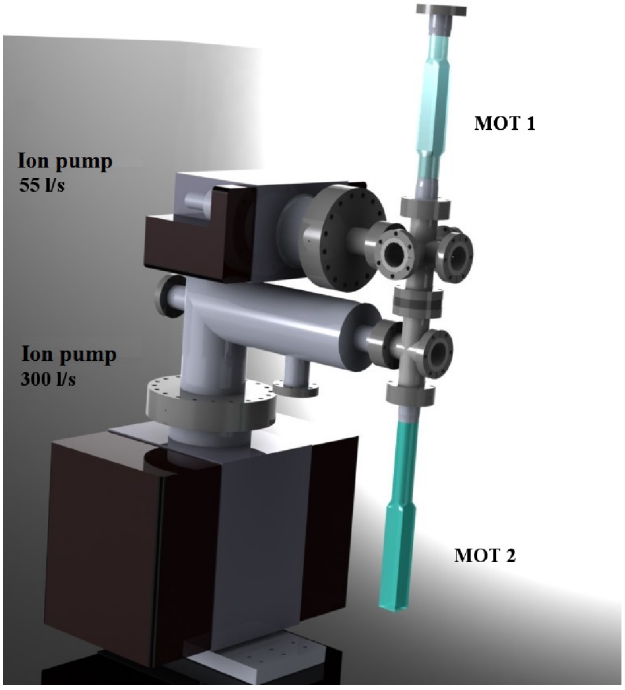

Figure 4.1.1 – The vacuum system has MOT1 chamber pumped by an ion pump of $55\,\mathrm{l}\cdot\mathrm{s}^{-1}$ (at the top) and MOT2 chamber pumped by an ion pump of $300\,\mathrm{l}\cdot\mathrm{s}^{-1}$(at the bottom). Source: elaborated by the author.

4.2 Hyperfine structure of ^{87}Rb

Let us first make a brief introduction of the sample to be studied. We use an alkali atom, the isotope ^{87}Rb, whose electronic structure is: $1S^2 2S^2 2P^6 3S^2 3P^6 3D^{10} 4S^2 4P^6 5S^1$. ^{87}Rb has 37 electrons which have only one electron in the outermost energy level ($5S^1$). Thus, the levels structure is simple in principle and it can be considered as a hydrogenic atom. Rubidium has only two stable isotopes ^{85}Rb and ^{87}Rb, where the last one is almost 28% of rubidium in the natural state. We chose ^{87}Rb to achieve quantum degeneracy by technical simplicity, since the scattering length of ^{85}Rb is negative, while for ^{87}Rb it is positive (13).

The principal quantum number of the last electron^{87}Rb corresponds to level $N = 5$. Therefore, the quantum number of orbital angular momentum is $L = 0, ..., 4$. If we consider the hyperfine structure, i.e. the coupling between the angular momentum and orbital angular momentum spin $\hat{\mathbf{J}} = \hat{\mathbf{L}} + \hat{\mathbf{S}}$, where $\hat{\mathbf{L}}$ and $\hat{\mathbf{S}}$ are the respective operators. We can see that the quantum number associated with this coupling is $|L - S| \leq J \leq L+S$. At this point, the " lonely" electron spin in the last layer whose quantum number is $S = \frac{1}{2}$, so you can take $L = 0$ and $L = 1$ as the ground state and first excited state, respectively.

In the ground state ($L = 0$) the total angular momentum is $J = \frac{1}{2}$, so we call this state as $5^2S_{1/2}$. For the first excited state ($L = 1$) we have $J = \frac{1}{2}, \frac{3}{2}$ two states which we call $5^2P_{1/2}$ e $5^2P_{3/2}$. The transitions $L = 0 \rightarrow L = 1$ are known as the D-lines, which can be classified as:

$$\begin{aligned} D_1 - \text{line} \quad 5^2S_{1/2} &\rightarrow 5^2P_{1/2}, \\ D_2 - \text{line} \quad 5^2S_{1/2} &\rightarrow 5^2P_{3/2}. \end{aligned} \tag{4.2.1}$$

The notation used is $N^{(2S+1)}L_J$.

The coupling of $\hat{\mathbf{J}}$ with the total nuclear angular momentum $\hat{\mathbf{I}}$ generate the hyperfine structure. In ^{87}Rb the nuclear quantum angular number is $I = \frac{3}{2}$. The total atomic angular momentum $\hat{\mathbf{F}}$ is then given $\hat{\mathbf{F}} = \hat{\mathbf{J}} + \hat{\mathbf{I}}$, where $|J - I| \leq F \leq J + I$. The ground state $5^2S_{1/2}$ has $F = 1, 2$ and the first excited state has $5^2P_{1/2}$ (D_1-line) with $F = 1, 2$ and $5^2P_{3/2}$ (D_2-line) with $F = 0, 1, 2, 3$ (Fig. 4.3.1).

4.3 Lasers system

The control of the frequency turns out to be important to cool the atoms. The experiment has three diode lasers of the amplified TOPTICA Photonics model DLX110-L with a wavelength of 780 nm. The diode laser has a line width of only 1 MHz, which is ideal to excite selectively the hyperfine levels of the atoms ^{87}Rb (Fig. 4.3.1).

Two laser transitions $5^2S_{1/2}\,(F = 2) \rightarrow 5^2P_{3/2}\,(F' = 3)$, which we call cooling 1 and 2, are used to generate the optical trapping of MOT1 and MOT2, respectively. The cooling frequencies have a red-detuning of approximately ~ 20 MHz. Another laser transition $5^2S_{1/2}\,(F = 1) \rightarrow 5^2P_{3/2}\,(F' = 2)$ is used to pump the atoms into cooling transition of both MOTs. Lasers can be used in other processes, besides cooling. To transfer the atoms from the first chamber to the second one, we use the push beam from cooling 2 laser, which will have the same frequency detuning trapping. In addition, we have a beam to image the atoms in resonance with $5^2S_{1/2}\,(F = 2) \rightarrow 5^2P_{3/2}\,(F' = 3)$. Finally, we also have two beams that select the state hyperfine $F = 2$ with $m_F = 2$ when the atoms are transferred to the purely magnetic trap, these beams are known as optical pumping beams ($5^2S_{1/2}\,(F = 1) \rightarrow 5^2P_{3/2}\,(F' = 2)$ and $5^2S_{1/2}\,(F = 2) \rightarrow 5^2P_{3/2}\,(F' = 2)$).

During the course of the experiment, it is necessary to vary continuously (or suddenly) the frequency and power of some of the beams, or simply switch-on or switch-off (in some process during the experimental sequence). For this reason, the beams are different by 10 acousto-optical modulators (AOM). An AOM is a crystal in which an acoustic wave is induced radio frequency (RF). When light enters the crystal interacts with a acoustic wave and is diffracted. The diffracted beam has a frequency shift proportional to RF, and

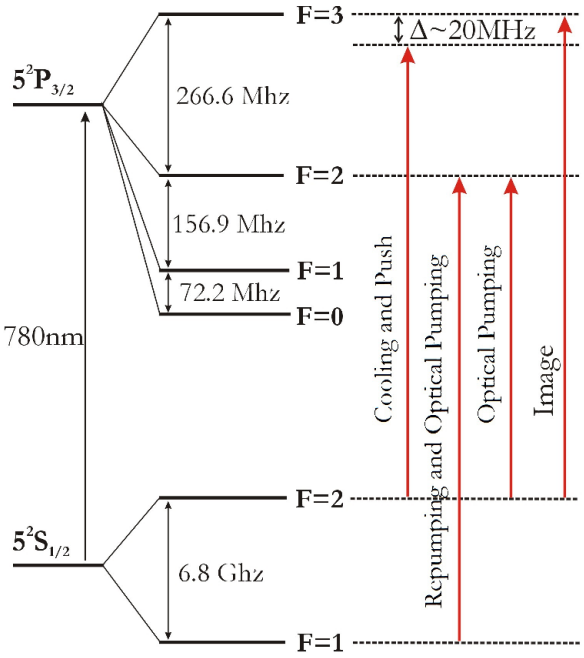

Figure 4.3.1 – Frequencies scheme in the hyperfine structure of ^{87}Rb, which is used for this experimental setup. Source: elaborated by the author.

we can obtain a detuning to blue one or red one, depending on the diffraction order. The AOMs can be disconnected within a few microseconds, or we can sweep the frequency and amplitude quickly or slowly.

4.4 Absorption image diagnosis

Throughout the experimental sequence it is necessary to know the number of atoms of the sample temperatures for either optimization or data collection. Optical diagnostics allow us to obtain useful information on scales of BEC systems, which usually have $< 10^7$ atoms and temperatures below 1 mK. There are different light scattering methods implemented for dilute atomic gases (79), and we use the most common one: the *absorption imaging*.

Considered the most practical for our experiment, the optical absorption consists of lighting up a sample with a collimated laser beam, resonant one with the transition $5^2S_{1/2}\,(F = 2) \rightarrow 5^2P_{3/2}\,(F' = 3)$. The cloud absorbs some of the photons of the beam leaving a dark "shadow" in the beam. Then, the beam passes through a lens system that forms an image of the shadow. This shade corresponds to the absorption profile of the gas and it is proportional to density profile. Experimentally, the cloud is released from the trap and the image is made after the *free expansion* or *time of flight* (**TOF**); all pictures in our experiment are made in this way. Note that this technique allows us to count the number of atoms in the sample, measuring the temperature, and determining the dimensions and geometry of the cloud.

The normalized absorption image can be constructed from the three processing images captured by the CCD camera pixelfly pco.imaging model 270XS which contains a chip with dimension 1392×1024 pixels with $6.45 \times 6.45\,\mu m^2$ by pixel. To capture these images we use a program written in LabView and developed by our group. Three images are captured: an image beam with atoms, an image of the beam without atoms and a dark image with no light. Taken these images to compose the normalized absorption image illustrated in Fig. 4.4.1.

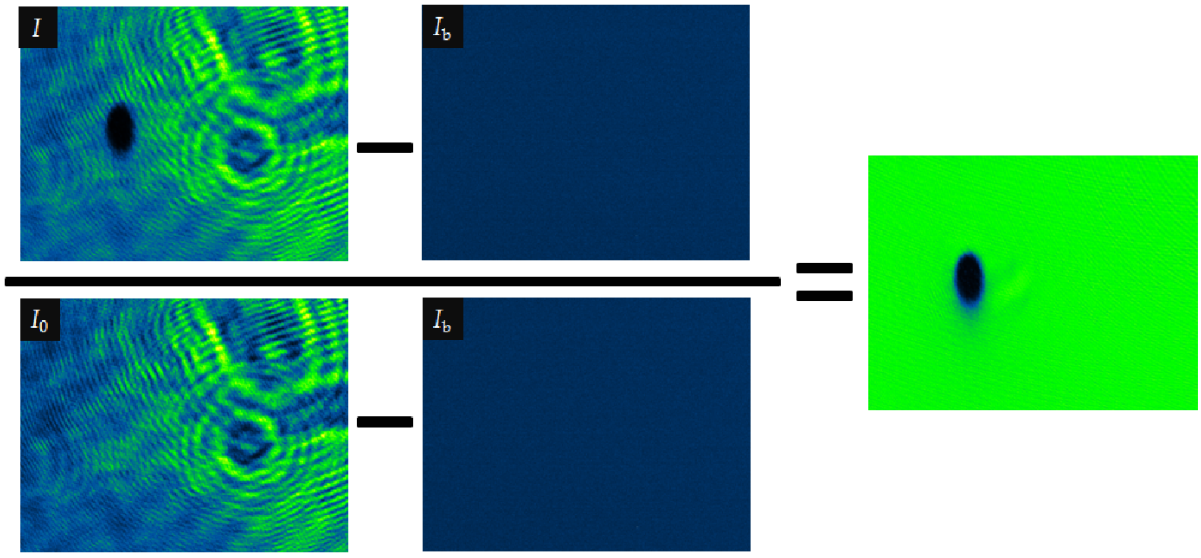

Figure 4.4.1 – Scheme for normalized absorption image. We use three images: I-image is the beam intensity with atoms, I_0-image is the beam intensity without atoms e I_b-image is background without light. Source: elaborated by the author.

The analysis of the cloud is made using the Beer-Lambert law. In this form, we integrate along an axis and we can get the density profile of two-dimensional atomic cloud:

$$n_{2D}(y,z) = \int dx\, n(x,y,z) = -\frac{1}{\sigma_0}\left[\frac{I(y,z) - I_b(y,z)}{I_0(y,z) - I_b(y,z)}\right] \tag{4.4.1}$$

where $n(x,y,z)$ is the three-dimensional density profile of the atomic cloud, σ_0 is the scattering cross section, $I(y,z)$ is the intensity of the beam with atoms, $I_0(y,z)$ is the beam intensity without atoms e $I_b(y,z)$ is the intensity of dark image. The profile $n_{2D}(y,z)$ provide the dimensions, number of atoms and temperature.

The cloud is of order of just a few hundred micrometers in the case of degenerate quantum sample, it is necessary to implement a set of lenses that will amplify the size of the image (79). In turn our experiment has conveniently two different magnifications each with a set of lenses themselves (74). The first one is 5X magnification and the second one

is 2X magnification, labeled as the image axes 1 and 2, respectively. The optical paths of both axes are mutually perpendicular and differ in only 5% in the physical parameters extracted.

4.4.1 Thermal cloud analysis

The density profile of a thermal cloud can be appropriately approximated by a usual Gaussian distribution

$$n_{G2D}(y,z) = \eta_G \exp\left[-\frac{(y-y_0)^2}{2\sigma_y^2} - \frac{(z-z_0)^2}{2\sigma_z^2}\right]. \tag{4.4.2}$$

The size of the cloud can be defined using two widths σ_x and σ_y. y_0 and z_0 are the distribution centers in the image, and η_G is the peak value of the distribution.

The total number of atoms can be calculated also from the gaussian distribution with a simple calculation:

$$N_{th} = \int dydz\, n_{G2D}(y,z), \tag{4.4.3}$$

whose result is

$$N_{th} = \frac{2\pi}{\sigma_0}\eta_G\sigma_y\sigma_z. \tag{4.4.4}$$

This indicates that the total number of particles in a thermal cloud is directly proportional to the product of gaussian widths. It is worth noting that there is a different method to count the number of atoms, either of thermal or condensed clouds. The number counting method is independent of fittings, and it works adding pixel by pixel then it multiplies a factor giving the number of atoms. In our experiment the difference represented less than 2% then simply we use the distribution.

In the unidimensional case, we can relate the speed of expansion with temperature by the expression $\frac{1}{2}mv^2 = \frac{1}{2}k_BT$, where m is the mass of atom and v is the expansion velocity. The profile of the cloud $n_{G2D}(y,z)$ is given by expansion time t_{exp}. Fitting a gaussian distribution in the profile can be achieved width as a function of expansion time $\sigma = \sigma(t_{exp})$. Therefore, the expansion velocity is given by $v = \frac{d\sigma(t_{exp})}{dt_{exp}}$ and we can calculate the temperature using:

$$T = \frac{m}{k_B}\left(\frac{d\sigma(t_{exp})}{dt_{exp}}\right)^2.$$

Once the cloud expands freely, the expansion velocity is constant. Therefore, for a time expansion t_{exp}, the speed of expansion é $v = (\sigma - \sigma^0)/t_{exp}$, where σ^0 is the initial width. For a sufficiently large time expansion (greater than 10 ms), we can assume that $\sigma \gg \sigma^0$.

Then we extract the temperature of the cloud using the expression:

$$T = \frac{m}{k_B}\left(\frac{\sigma}{t_{exp}}\right)^2, \tag{4.4.5}$$

whereσ is the width provided by the normalized image.

4.4.2 Condensed cloud analysis

In the case of a cloud quantum number of atoms may be calculated using a Thomas-Fermi Distribution from eq. (3.2.12) integrated in one direction4.4.6

$$n_{TF2D}(x,y) = \eta_{TF}\max\left[\left(1 - \frac{(y-y_0)^2}{R_y^2} - \frac{(z-z_0)^2}{R_z^2}\right)^{3/2}, 0\right]. \tag{4.4.6}$$

Similarly, integrating over all space we obtain the particle number of the cloud condensed

$$N_0 = \frac{5}{4\sigma_0}\eta_{TF}R_yR_z. \tag{4.4.7}$$

In this case we have that the number is directly proportional to the Thomas-Fermi radii.

The density distribution is obtained from eq. (3.2.12) in the TFA for a pure condensate in a harmonic potential. For this reason in principle condensed cloud has no temperature. However, we can estimate a mean field temperature (80) or use the expression (3.1.35).

4.5 Magneto-optical trap

As its name indicates, it is a trap that combines magnetic fields and light. The MOT technique uses clouds with low densities and it is fundamentally based on the idea that the photon transfers momentum. MOT consists of magnetic confinement for the atoms in a potential generated by two coils in anti-Helmholtz configuration and use coherent light to generate an optical molasses(81). We use lasers to the atom in the cloud absorb the highest amount of photons, so that the force associated with the interaction of the atom with the light strongly depends on the frequency of the laser and its detuning (due to the Doppler effect) (82, 83). When the atom approaches the light source feels a higher frequency otherwise it feels a lower frequency.

We can use a toy model to facilitate the understanding of the operation of MOT (84), consider a one-dimensional system (Fig. 4.5.1) formed by a two-level atom that has a ground state with angular momentum $|F = 0, m_F = 0\rangle$ and an excited state with $|F = 1, m_F = 0, \pm 1\rangle$. Moreover, magnetic field that varies linearly with the position and

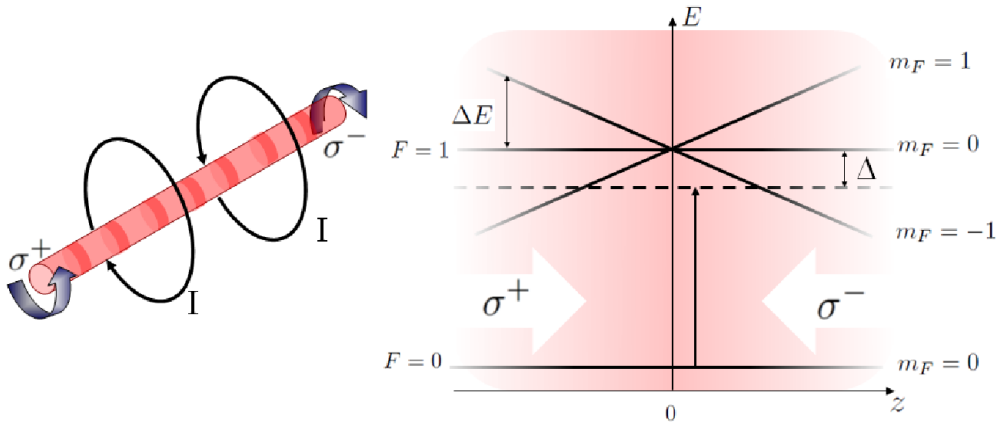

Figure 4.5.1 – Scheme of a one dimensional magneto-optical trap. Source: elaborated by the author.

spacing between the levels is $\Delta E = \mu_B m_F B$, where μ_B is the Bohr magneton, valid for the Zeeman effect in weak magnetic field.

Assume that the atom is exposed to a pair of counterpropagating laser beams along the z-direction with orthogonal circular polarizations and a frequency tuned below resonance in the region where $B = 0$. The zero field defines the region of origin ($z = 0$). Then for positive regions ($z > 0$) the atom absorbs more photons with polarization σ^-, since it induces a transition $\Delta m_F = -1$, thus suffer resultant force toward the origin. Similarly, for negative regions ($z < 0$) the atom absorbs more photons with polarization σ^+ which induces $\Delta m_F = +1$, so again suffer a force for the origin. The atoms remain confined in the system due to the restoring force and colds due to dissipative character of the spontaneous force.

In our experiment, we use six counter-propagating beams with circular polarization, aligned in a single point forming a volume, which functions as a viscous medium. In this region of space the viscous force is known as *optical molasses*. The magnetic field is inhomogeneous for the MOT and the magnetic gradient generated with the coils is around $12\,\mathrm{G} \cdot \mathrm{cm}^{-1}$.

4.6 Magnetic trap

The quadrupole magnetic trap is capable of generating gradients of the order of hundreds of Gauss per centimeter. We know that an atom in the presence of a magnetic field experiences a break degeneracy of energy levels. There are two regimes for the behavior of the hyperfine states (Fig. 4.6.1), the region of weak field regime known as anomalous Zeeman effect, and strong field region known as the Paschen-Back regime. We are interested in the regime of weak field displays, the region to the left of the dotted line in Fig. 4.6.1. We can see that some of the atoms minimize their energy in regions

where the field is minimal and others in the maximum. Thus, it is important to select the hyperfine levels of the atoms to be trapped in the minimum of the external potential. In ^{87}Rb this happens for the states $|2,2\rangle$, $|2,1\rangle$, and $|1,-1\rangle$, in our case we select the state hyperfine $F = 2$ with $m_F = 2$[1].

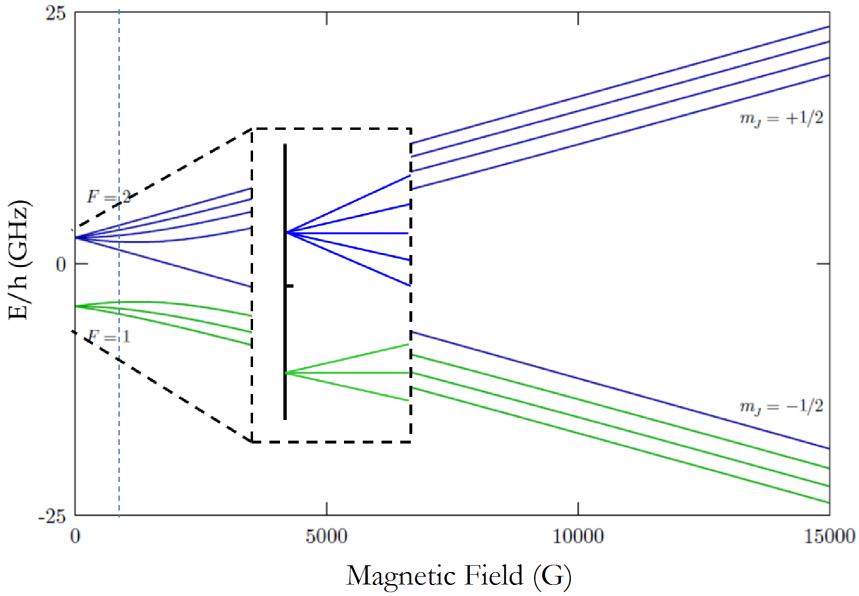

Figure 4.6.1 – Structure of ground state $5^2S_{1/2}$ of ^{87}Rb in a magnetic field. Source: elaborated by the author.

The MT consists of two coils whose currents circulate in opposite directions, i.e. in anti-Helmholtz configuration. These coils have a cooper wire 2 mm in diameter, 9 turns along the radial axis 11 along the axial axis. The profile of the absolute value of the magnetic field generated by the MT is shown in Fig. 4.6.2. We can see that MT has a quasi-linear behavior in all directions near to the zero field. Quadrupole traps have important advantages: The first one, it allow optical access, and the second one it allows trapping with large number of atoms with high densities.

4.6.1 Magnetic trap transference

The MOT technique is effective to cool atoms to temperatures of the order μK. However it is still a temperature that is far from achieving quantum degeneracy. In fact, the minimum temperature achieved by this technique is known as Doppler temperature limit (85), that for our experiment is around 120 μK. Using other procedures in the sample, such as molasses optical reached temperatures even lower known as sub-Doppler temperature (85). Molasses consists of an abrupt shutdown of the field, together with a detuning frequency for red ($\sim$ 60 MHz). At the end of this process, we achieved sub-Doppler temperatures around 40 μK.

[1] To simplify notation in the thesis we do $|F = 2, m_F = 2\rangle \equiv |2,2\rangle$

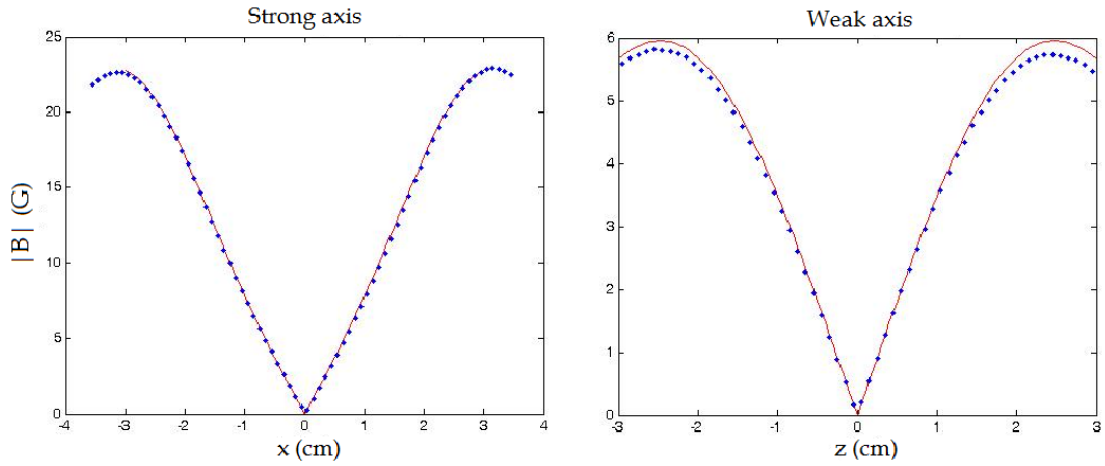

Figure 4.6.2 – The magnetic field generated by MT with a current of 1 A (a) along the x-axis axial and (b) along the z-axis parallel to gravity. The points are experimental data and the solid curve is the simulation. Source: elaborated by the author.

After the sub-Doppler cooling, the cooling light is switched off abruptly and starts the *optical pumping* process (86). With this process it is possible to transfer the atoms into a state that is magnetically trapped, and it is done in two steps. At first step, we transfer the atoms to $F = 2$ ground state $5^2S_{1/2}$, turning off the light leaving the light trapping and repumping connected by the 0.5 ms. At second step, we turn on a weak magnetic field (~ 1 G), which breaks the level degeneracy, and we applied two beams of σ-polarized light, $5^2S_{1/2}\,(F = 1) \rightarrow 5^2P_{3/2}\,(F' = 2)$ and $5^2S_{1/2}\,(F = 2) \rightarrow 5^2P_{3/2}\,(F' = 2)$, during 0.05 ms. After a few cycles of absorption and emission of transfer over 95% efficiency to the ground state $|2, 2\rangle$.

4.6.2 Pure magnetic trapping

When the sub-Doppler temperature is reached, and the atoms have been previously pumped into the hyperfine state $|2, 2\rangle$, the magnetic field is abruptly increased to a gradient of $60\,\mathrm{G} \cdot \mathrm{cm}^{-1}$. Then, the magnetic field is ramped linearly during 500 ms from $60\,\mathrm{G} \cdot \mathrm{cm}^{-1}$ to $160\,\mathrm{G} \cdot \mathrm{cm}^{-1}$. Once the potential is maximum gradient it is highly confining and we can implement the *evaporative cooling* technique. In this type of cooling, the spin-polarized atoms are in strongly attractive potential, we induce a transition such that leaves the atoms in a completely repulsive potential, and escape out of the trap. Inducing selectively transitions, we can remove the most energetic atoms, such a way that the atoms termalize at a lower temperature due to collisions.

In practice, we apply a wave radio-frequency (**RF**), which reverses the spin of the atom releasing the hottest atoms to a not trapped state. This is possible due to the inhomogeneity of the field, since it separates the Zeeman levels, then only the atoms with higher energy shall reach places high field. RF effect can enter into resonance with

the higher levels separated by inducing a transition of spin, so that the hot atoms are removed from the trap. Cooling is continuous and frequency is constantly adjusted leaving the system with ever lower temperatures.

The full form functional magnetic field is calculated in ref. (87), nevertheless we can approximate the potential generated by quadrupole coils, a linear potential of the form:

$$U_{MT}\left(\mathbf{r}\right) = \mu B'_x \sqrt{x^2 + \frac{y^2}{4} + \frac{z^2}{4}} \tag{4.6.1}$$

where $\mu = g_F m_F \mu_B = \mu_B$ is the Bohr's magneton for $|2, 2\rangle$ and B'_x is the gradient along the strong direction. The disadvantage of this format of the field lies in the quadrupole transitions Majorana losses (88). Atoms confined to pass through the center, i.e. the region of zero magnetic field, can quickly change the selected spin state. The change spin effect is more significant when the atoms are very cold. Thus cold atomic clouds, there is a high probability of transitions to not-trapped states, losing significantly atoms and therefore density. Thus, the BEC can not be done in the quadrupole magnetic trap. Our experiment implements two RF linear ramps in MT from 20 MHz to 3.5 MHz during 6 s, before we losses atoms due Majorana transitions.

An important detail for our experiments of thermodynamics is the necessity of knowing so well about the gradient in the region of the atoms. Since B'_x determines the dynamics and frequency in one of the axes of trapping. In ref. (10) and in our experiment at the end of RF evaporation, the gradient is relaxed to the limit to compensate the gravity, then this is ramping up leave compensate one. Note that the value around gravity compensation is determined by the weak axis, which corresponds to $B'_z = B'_x/2$. This introduces an interesting difference in the geometry reported in ref. (10).

Fig. 4.6.2 indicates that there is good agreement between the field of experimental measurements and simulation, however this measure was made with the coils out of the experiment. Our interest is to determine the gradient of the field in the region of the atoms and to know the value. We calibrate the current passing through the quadrupole coils and then we simulate the gradient based on the behavior of atoms. In the first step, it's necessary to calibrate the current source DELTA Elektronica series SM 70-40 and the analog channel AO.0 control program. Fig. 4.6.3(a) shows the linear relation between the current and the voltage value, this lets us know how much current is going through the two quadrupole coils.

Using absorption imaging we know that for a current of 4.3998 A the gradiente exactly compensates the gravity. A simulation where the separation between the coils was 3.85 cm, so that for a current of 4.3998 A generates a gradient of $15.26\,\mathrm{G}\cdot\mathrm{cm}^{-1}$ in the direction of gravity. Gradient calibration as function of current is shown in Fig. 4.6.3(b).

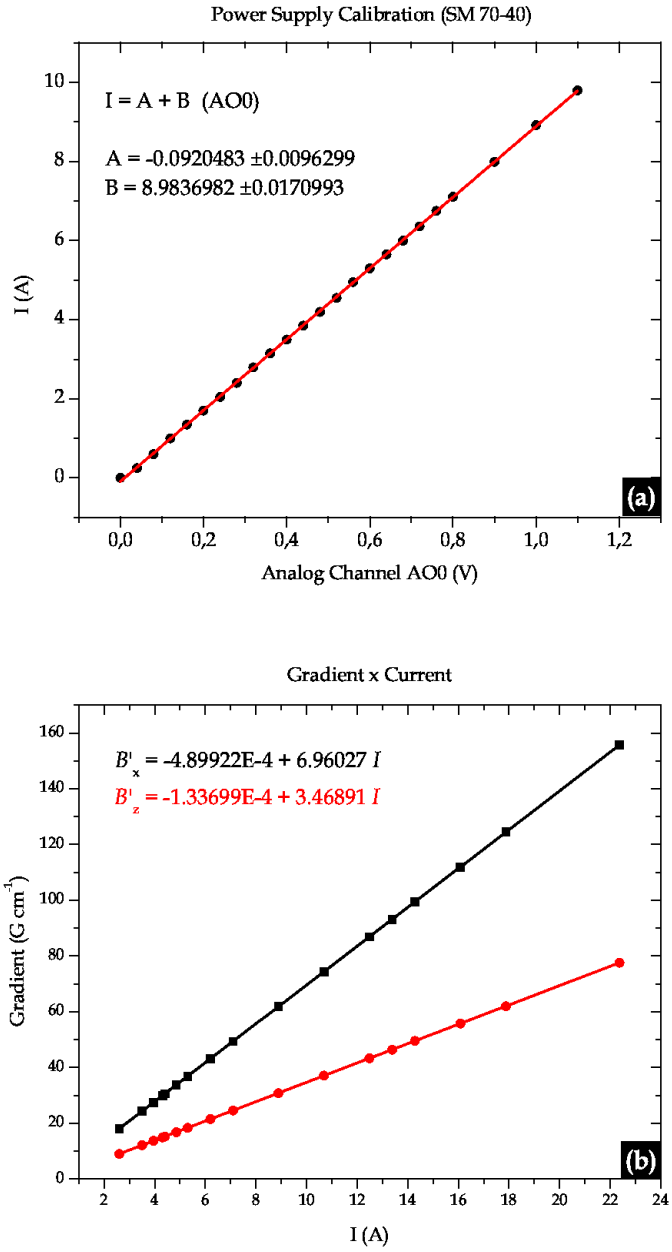

Figure 4.6.3 – Gradient of the magnetic trap: (a) Calibration of power supply current as function of voltage of control analog channel, and (b) simulation of the gradients along the strong axis and weak axis as function of the current. Source: elaborated by the author.

4.7 Hybrid trap

Note that the potential has to be soft to suppress channel loss as Majorana transitions. There are different ways to get around this problem by using different configurations of traps reported in the literature (5, 6, 7, 89, 90, 8, 9). Our experiment produces BEC using the HT, which is a composition of a magnetic field produced by MT and an electric

field produced by a focused beam of OT, similar to used by Lin in Ref. (10). The OT has the advantage that the atoms need not be spin polarized and can be prepared in any one of the hyperfine ground state. However OT inherently have a smaller volume in comparison with a magnetic trap. The HT is a 3D trap ideal for experiments in thermodynamics, since it allows us to control the frequency of the bottom of the potential well, and thus allows us to control the volume of the sample.

4.7.1 Optical dipole trap

The trap for light confinement is based on the interaction of electric dipole of the atom with the electric field of the incident light (91, 92). The frequency of this ligth is far-detuned from the resonance transition of the atoms, in our case a red-detuned laser with a wavelength of 1064 nm Ytterbium fiber of IPG PHOTONICS. There are many ways to trap atoms with lasers, using blue or red detuned lasers or a combination of both. An atom placed in a OT experiences two kinds of forces: A dipole force and a scattering force. The scattering force originates from the associated momentum of light; usually this force is negligible as compared to the dipole force.

The model describes the interaction of atoms and light fields has the next Hamiltonian (93, 94)

$$\hat{H}_{DA} = \hat{H}_{\text{int}} + \hat{H}_{\text{field}} + \hat{U}_D,$$

this model is known as the *dressed atom model*. $\hat{H}_{\text{int}}$ is the Hamiltonian for internal degrees of freedom of atom. $\hat{H}_{\text{field}}$ is the Hamiltonian representing free oscillation modes of the electromagnetic field. In this model the states are a direct product of atom state and photon state $|\text{atom}\rangle \otimes |\text{photon}\rangle$, respectively. In fact, an atom is not a pure two-level system, but has many energy levels which interact with the light, but for simplicity we consider the two-level model. $|g, n+1\rangle$ and $|e, n\rangle$ represent as the ground state and the excited state, respectively, where n is the number of photons.

The linear combination of photon and atom states allows us to diagonalize the entire Hamiltonian by taking $\hat{U}_D$ as a operator of second order perturbation. $\left\langle \hat{U}_D \right\rangle = \langle e, n| \hat{U}_D |g, n+1\rangle$ reprensents a atomic transition from ground to excited state. Essencially $\hat{U}_D = \hat{\mathbf{p}}(\mathbf{r}, t) . \mathbf{E}(\mathbf{r}, t)$ which is coupled to an external electromagnetic field $\mathbf{E}(\mathbf{r}, t)$ and its induced dipole moment $\hat{\mathbf{p}}(\mathbf{r}, t)$. The transition due to this interaction is proportial to Rabi oscillation frequency Ω_R:

$$\left\langle \hat{U}_D \right\rangle = \frac{1}{2}\hbar\Omega_R = \sqrt{\frac{3\pi\hbar c^2\Gamma}{2\omega_0^3} I(\mathbf{r})},$$

where $I(\mathbf{r})$ is the intensity of electric field which varies with the position. ω_0 and Γ are the resonance frequency and decay width of the state, respectively. The energies are therefore position dependent for inhomogeneous light fields. The general expression for the dipole

potential for transition $|i\rangle \rightarrow |j\rangle$ is

$$U_{OT}(\mathbf{r}) = \sum_{i \neq j} \frac{\left|\langle j|\hat{U}_D|i\rangle\right|^2}{E_i - E_j} = \frac{3\pi\hbar c^2}{2\omega_0^3}\frac{\Gamma}{\Delta} I(\mathbf{r})$$

where the detuning is $\Delta = \omega - \omega_0$. In a red detuned ($\Delta < 0$) the energy of the ground state decreases proportional to the increasing intensity of the laser, as a result, the atom moves to the potential minimum (91).

Clearly the spatial geometry of the potential is determined by $I(\mathbf{r})$, in this manner the simplest way to trap atoms is by focussing a red detuned single gaussian laser beam (95). The potential generated is as follows

$$U_{OT}(\mathbf{r}) = -\frac{U_0}{(1 + y^2/y_R^2)} \exp\left[\frac{-2(x^2 + z^2)}{w_0^2(1 + y^2/y_R^2)}\right]. \tag{4.7.1}$$

$U_0 \equiv U_0(P, \Delta)$ is function of powe laser P and detuning Δ. y is the direction of propagation of the beam and y_R is called the *Rayleigh range*. w_0 is the beam waist size which is determined experimentally by optics. The potential depth is usually below 1 mK, which implies a limitation on the amount of catch compared to a magnetic trap. Nevertheless, the capture volume can have different configurations in a controlled manner.

4.7.2 Optical trap transference

Hybrid trap basically uses the MT as a reservoir for loading directly to OT. The process is as follows: Once the atoms are transferred to the maximum gradient of MT we use RF evaporation temperature decrease and increase the phase space density . During the RF process, the beam of optical trap is switched on increases the efficiency of evaporation (10). The OT waist is aligned 300 μm down the quadrupole center (zero) in the direction of gravity. The alignment of the minimum potential guarantees a harmonic confinement in three directions.

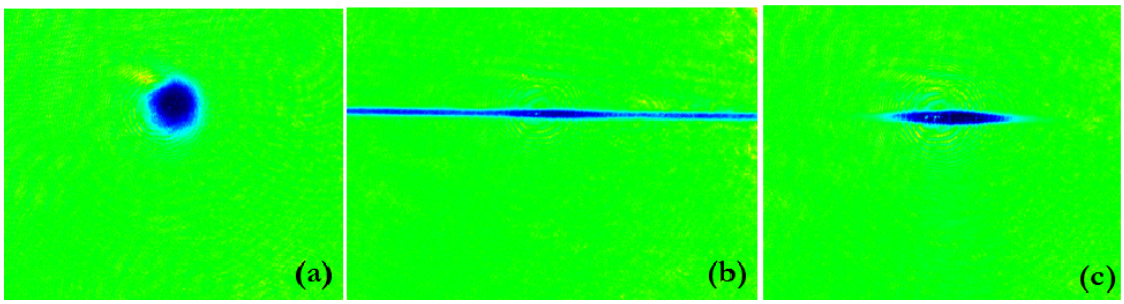

Figure 4.7.1 – Image (a) the quadrupole trap and (b) the optical dipole trap generating (c) the hybrid trap. Source: elaborated by the author.

The gradient of the quadrupole is relaxed slowly until the magnetic field. This

does not compensate more gravity, while the atoms are transferred to the optical trap. Once done transfer adiabatic way, we finally evaporated in optical trap (without turning off the magnetic field) again increasing the density in phase space. The depth of the potential depends directly on the laser power, so we can do an evaporation changing this depth. At this point we can achieve the density and temperature required for the quantum degeneracy.

We have implemented a series of four ramps evaporation, so that each ramp atoms termalize at a lower temperature due to elastic collisions. Our experiment starts with a power of 6 W approximately and ends on the order of 40 mW focused on the region of atoms approximately 75 μm in diameter ($w_0 = 75\mu m$).

The functional form of the effective potential for an atom in a hybrid trap is a composition of the magnetic component (4.6.1) and the optical component (4.7.1), including the gravity we have:

$$U(\mathbf{r}) = \mu B'_x \sqrt{x^2 + \frac{y^2}{4} + \frac{z^2}{4}} - \frac{U_0}{(1 + y^2/y_R^2)} \exp\left[-\frac{2x^2 + 2(z - z_0)^2}{w_0^2 (1 + y^2/y_R^2)}\right] + mg(z - z_0) + E_0, \tag{4.7.2}$$

where z_0 is the offset between the dipole beam trap depth and the zero-field of quadrupole trap. E_0 is the energy difference between the zero-field point absent the dipole trap and the total trap minimum (10). In the Fig. 4.7.2 we represent two experimental situations: Fig. 4.7.2(a) a gradient of the magnetic field around $150\,\mathrm{G \cdot cm^{-1}}$ and a power of 5 W similar to the initial configuration of the HT. The Fig. 4.7.2(b) shows a similar configuration to the final stage for condensing. In this case the magnetic field is relaxed and ceases to compensate the gravity[2], on the other hand the power is around 40 mW. We can see that in profile shown in Fig. 4.7.2(b) around minimum, the potential is smooth and harmonic, which allow us to achieve the quantum degeneracy smoothly.

The eq. (4.7.2) helps us to establish the nomenclature of coordinates or directions used for thesis data later (Fig. 4.7.3). The strong axis of the quadrupole has been labeled with the variable x. The direction of propagation of the beam has been labeled with the variable y. Finally, the direction of gravity will be labeled with z. The radial confinement of OT will be in the xz-plane, while the confinement due to the magnetic field will be in the y-direction.

4.8 ^{87}Rb Condensate

In the late stage of evaporative cooling in the optical trap, we are able to achieve quantum degeneracy. HT is reproducible, which is an important feature for systems such as ours. The final en la default setting for the OT has a power of 40.4 mW with a depth of

[2]The gradient that compensates the gravity for the ground state $|2, 2\rangle$ is $15.26\,\mathrm{G \cdot cm^{-1}}$.

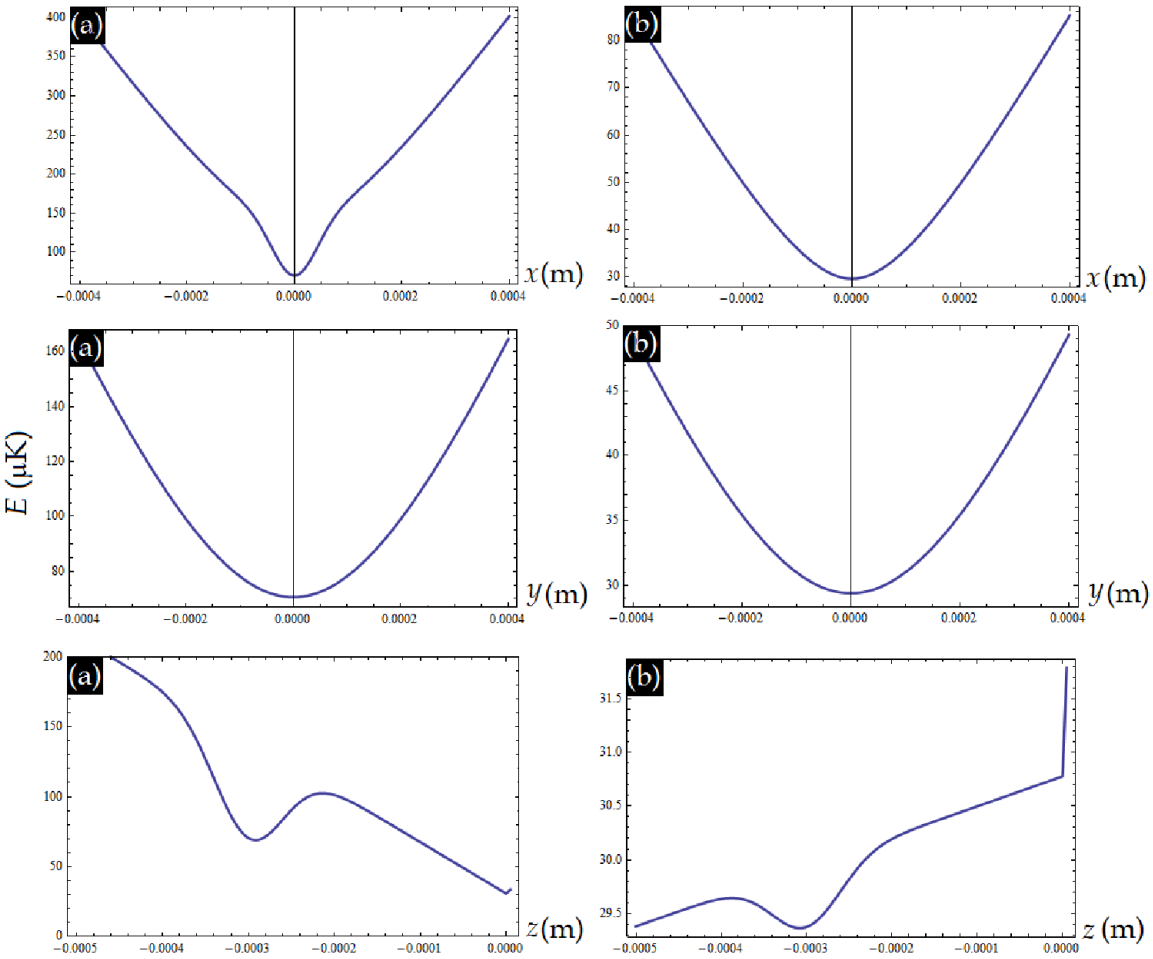

Figure 4.7.2 – Hybrid trap potential for two configurations: (a) high gradient and high power and (b) gradient relaxed to not compensate the gravity and low power (see text). Source: elaborated by the author.

0.8 μK. The final gradient magnetic is 29.98 G$\cdot$cm^{-1} in the strong axis, which corresponds to a value below the gradient of gravity compensation. With these parameters we are able to produce a BEC with a condensate fraction $> 80\%$ to a temperature of 80 nK, and a total number of atoms 8×10^4.

Previous experiments performed in our laboratory (96) showed the possibility of constructing phase diagrams (37). However, changes in the frequencies imply non-trivial changes in the evaporating cooling, therefore this experiments have a limitation on variations of the volume parameter. The hybrid trap resolves the problem to vary the volume parameter. As shown in Fig. 4.8.1 geometry of the cloud condensed varies depending on the frequency of the trap, this conclusion is derived from the eq. (3.2.15). Usually, the samples are *bicomponent*, this means that they have a thermal part and another part condensed. The atomic density which describes a gas reached quantum degeneracy follows a *bimodal distribution*. Experimentally the bimodal distribution is the setting of a Gaussian profile (eq. (4.4.2)) and a Thomas-Fermi profile (eq. (4.4.6)). The Fig. 4.8.1 shows different samples under different conditions of temperature and a condensed fraction with

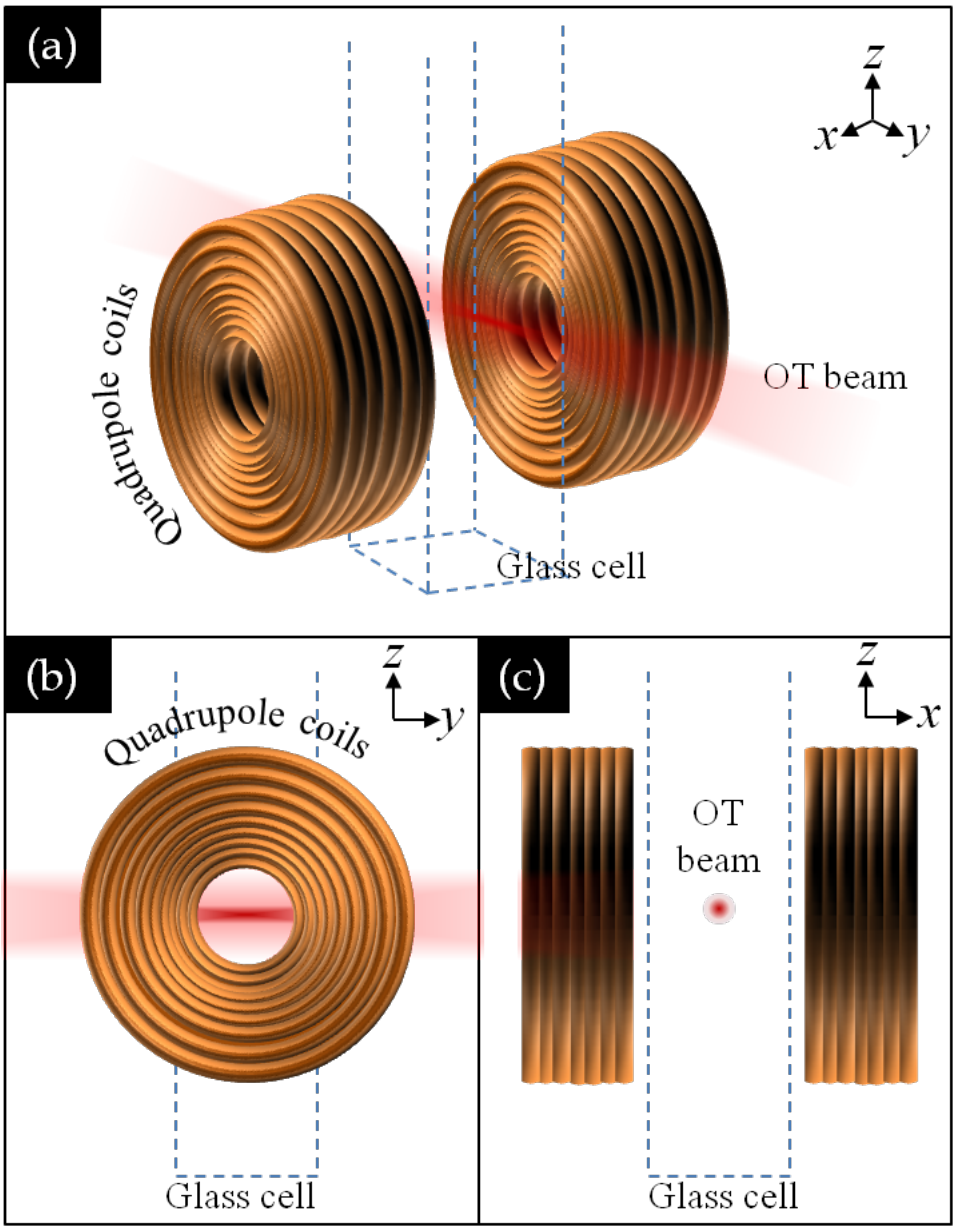

Figure 4.7.3 – (a) Hybrid trap 3D scheme. We see the image planes (b) yz and (c) xz used for diagnostic and the measurements of this thesis. Source: elaborated by the author.

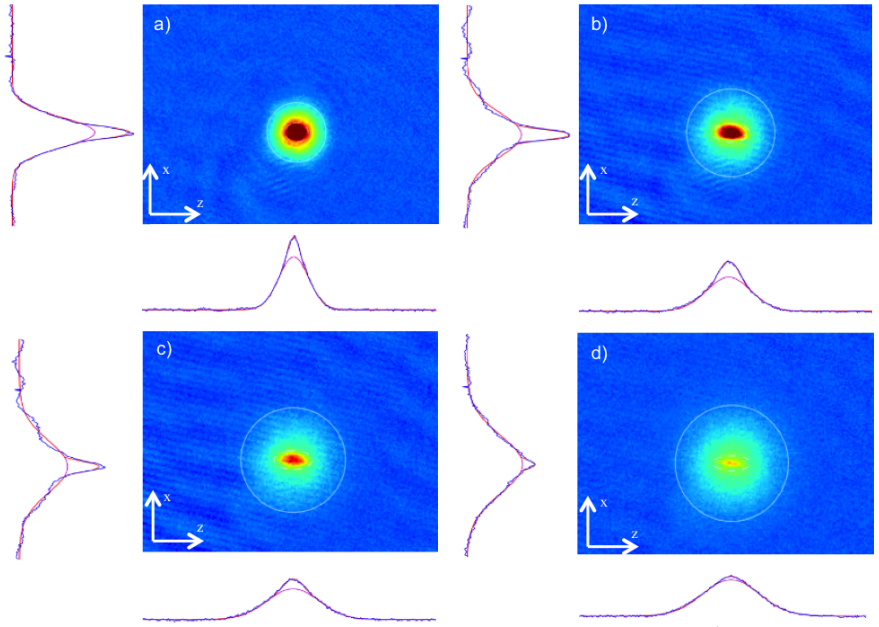

Figure 4.8.1 – Condensate clouds for different power configurations of OT: (a) 30 mW, (b) 43 mW, (c) 90 mW, and (d) 400 mW . The geometry of the trap change if we change the OT laser power. Source: elaborated by the author.

corresponding bimodal adjustments.

Images of the condensed cloud at different times of free expansion can be obtained simply by turning off the trap in a time shorter than 50 μs. The cloud displays a very important signature revealing the Bose-Einstein: the *aspect ratio inversion*, which only happens when the system presents quantum degeneracy. This change depends on the initial conditions of the cloud inside the trap (Fig. 4.8.3). The condensed clouds are released from the trap, in the direction where they are more confined they expand faster. This means that the expansion is *anisotropic* (Fig. 4.8.2(a)). On the other hand, the thermal clouds expand in the same way in all directions, i.e. the expansion is *isotropic* (Fig. 4.8.2(b)).

The frequencies of the hybrid trap and how these are related to the expansion dynamics of the sample will be studied in detail in the following chapters.

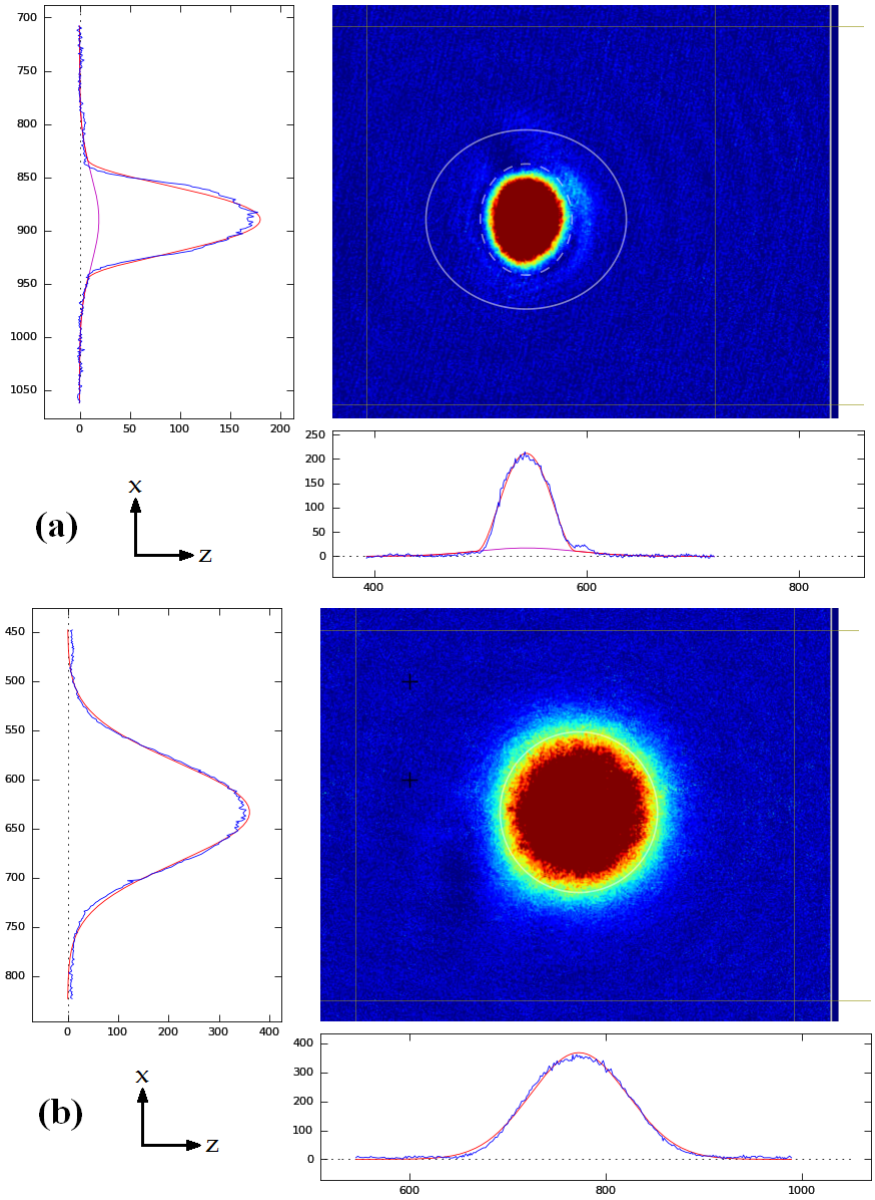

Figure 4.8.2 – This figure essentially shows the kinds of clouds obtained in our experiments. For example, the condensated cloud (a) is clearly anisotropic, where $R_y = 71.6\,\mu$m and $R_z = 59.1\,\mu$m with 8×10^4 atoms. On the other hand, the thermal cloud (b) is totally isotropic, where $\sigma_y = 63.2\,\mu$m and $\sigma_z = 63.2\,\mu$m with 2.55×10^5 atoms. Source: elaborated by the author.

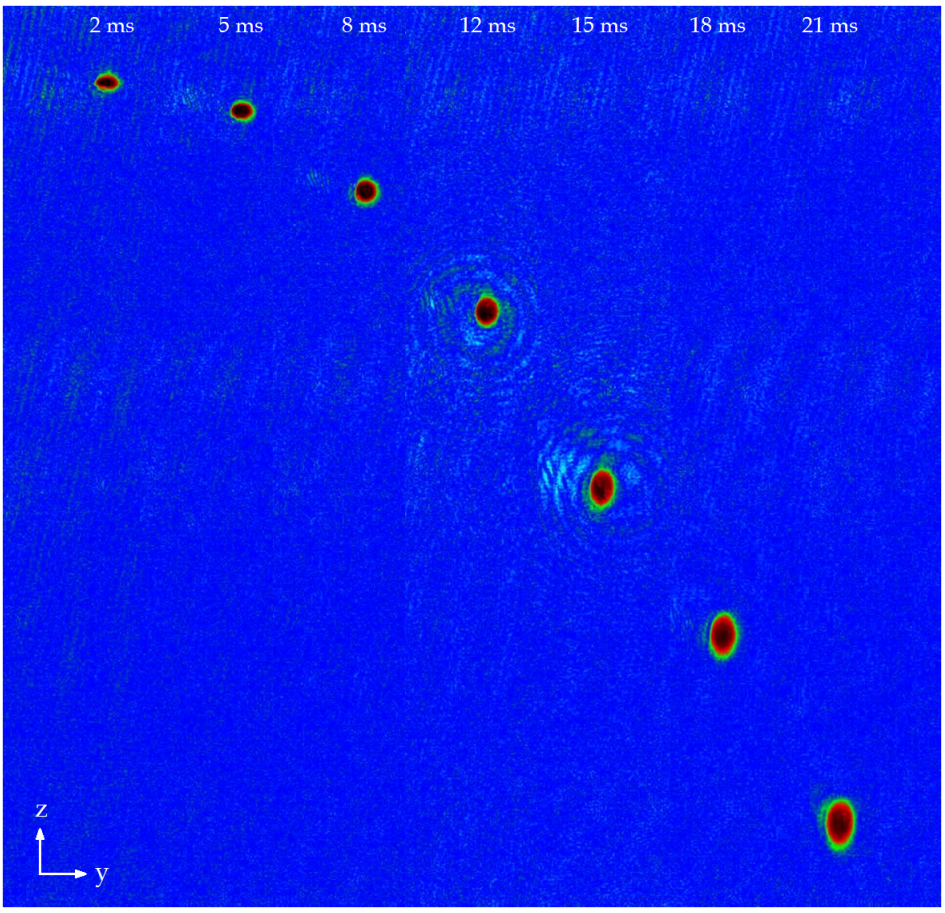

Figure 4.8.3 – Aspect ratio inversion for different time of flights of a condensed cloud. Source: elaborated by the author.

Chapter 5

Volume parameter and critical temperature

For the experiments of thermodynamics is convenient to make a more rigorous characterization of the trapping potential. This chapter aims to show how to perform this characterization, making a complete analysis of the frequencies of our system, which lead us to establish the volume parameter, $\mathcal{V}$. Let us remember that the choice of $\mathcal{V}$ as a thermodynamic quantity is not arbitrary, it meets the criteria of extensivity (97). We measure six different volume parameters, where we varied the usual physical quantities in the samples such as number of atoms, temperature and condensed fraction. When we cover a broad range of parameters we will be able to construct *phase diagrams* (37).

We will show in subsequent sections the measure of critical temperature T_C, which has a close to ideal gas behavior. The critical temperature is an essential measure to understand the phase transition from thermal phase to quantum phase. Using new global variables in the formalism of Romero-Rochín (37), we clearly observe the phase transition around T_C.

5.1 System characterization

We know that the HT allows a 3D-harmonic confinement, where the effective potential for atoms (eq. 4.7.2):

$$U(\mathbf{r}) = \mu B'_x \sqrt{x^2 + \frac{y^2}{2} + \frac{z^2}{2}} - \frac{U_0}{(1 + y^2/y_R^2)} \exp\left[-\frac{2x^2 + 2(z - z_0)^2}{w_0^2 (1 + y^2/y_R^2)}\right] + mg(z - z_0) + E_0$$

At low temperatures we basically have a well near to the equilibrium point. In this form, we can approximate to an harmonic trap from the HT effective potential, expanding $U(\mathbf{r})$

until second order in a Taylor series

$$\begin{aligned} U(\mathbf{r}) \simeq & \frac{1}{2}\mu B'_x z_0 - U_0 + E_0 + \left(\frac{1}{2}\mu B'_x + mg\right)(z - z_0) \\ & + \frac{1}{2}\left(\frac{4U_0}{w_0^2} + \frac{2\mu {B'}_x}{|z_0|}\right)x^2 + \frac{1}{2}\left(\frac{\mu B'}{2\,|z_0|} + \frac{2U_0}{y_R^2}\right)y^2 + \frac{1}{2}\left(\frac{4U_0}{w_0^2}\right)(z - z_0)^2 \\ & + \mathcal{O}\left(x^3, y^3, z^3\right). \end{aligned}$$

We consider $y/y_R \ll 1$ and we can identify the frequencies as

$$\omega_x = \sqrt{\frac{4U_0}{mw_0^2} + \frac{2\mu {B'}_x}{m\,|z_0|}},\ \ \omega_y = \sqrt{\frac{\mu {B'}_x}{2m\,|z_0|}},\ \ \omega_z = \sqrt{\frac{4U_0}{mw_0^2}}. \tag{5.1.1}$$

where the radial frequencies have a strong contribution of OT and the axial frequency depends only of magnetic field. The principal advantage of HT is that we can easily change the radial frequencies by varying the power laser, in this form it is possible to change the trap geometry, i.e. the volume parameter shown in eq. (3.1.31). In our experimental setup ω_y is approximately constant because the gradient is held fixed, but for higher powers of OT this would no longer be true.

5.1.1 Trap frequencies

From the eq. (5.1.1) we know that there is a direct dependence of the radial frequencies with the OT power. To ensure that the experiment is reproducible, it is necessary to make a calibration of the OT laser power as a function of voltage value in the control program AO.1. This measurement can be made by measuring the power in a reference position, which will be crucial to ensure reproducibility. In the Fig. 5.1.1 can see the calibration laser power in Watts according to following fit

$$P = A_2 + (A_1 - A_2)\left\{1 + \left(\frac{\mathrm{AO1}}{x_0}\right)^p\right\}^{-1}. \tag{5.1.2}$$

A_1 and A_2 are the minimum and maximum powers, respectively. The values shown in Fig. 5.1.1 were previously fitted using all experimental points. However, we need more accuracy at low power values, where the quantum degeneracy appears in our system, for this reason the data were readjusted.

The reference position is located before the optical elements and dichroic one vacuum cell. Thus, the calibration (5.1.2) has been considered to losses due to the dichroic and the faces of MOT2 cell. The windows of the cell have no coating for the wavelength 1064 nm. The value of these losses reduce the power of the beam by 11%.

To measure the frequencies we apply a magnetic field pulse with extra coil placed along the axis where we wanted to measure the frequency. When we turn on abruptly a

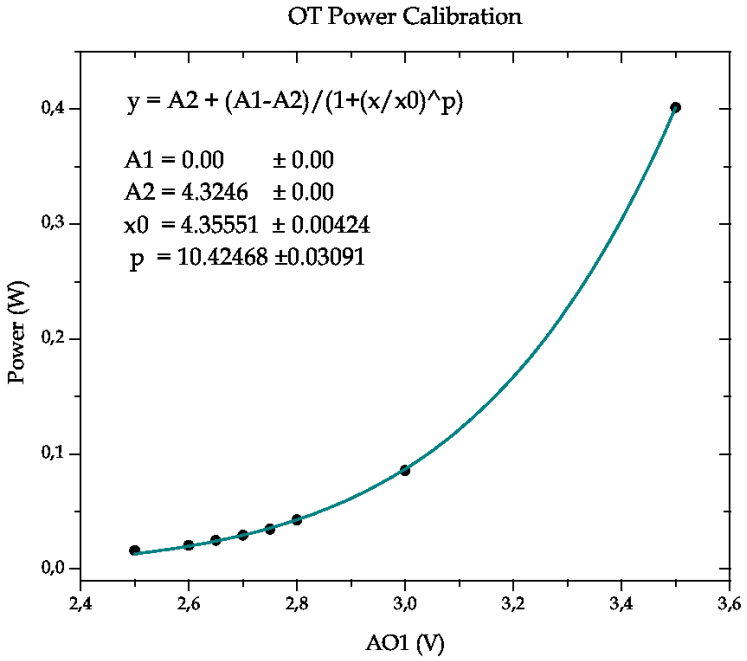

Figure 5.1.1 – Optical trap power calibration. Source: elaborated by the author.

pulse of magnetic field, the dipolar mode is excited and the condensate cloud oscillates with the frequency of the trap in the direction of applied field (47, 98, 99). The pulse duration ranged from 5 ms to 10 ms with around a magnetic field strength1 G to 5 G. The oscillations take place inside the trap and they are very small. Our experiment does not have enough resolution to detect this collective mode within the trap (47, 98, 99). To solve this problem, we do a typical image of cloud with TOF and we see the changes of the center of mass position for different waiting times, this procedure generates a graph as shown in Fig. 5.1.2.

Once the frequencies were measured independently, we can establish a relation between the frequency and the parameters of the trap. From eq. (5.1.1) we know that ω_x and ω_z strongly depend on the power and ω_y on the gradient. Thus, the calibration (5.1.2) serves us to find a relation between the radial frequencies and OT power. On the other hand, the gradient is kept fixed, and it is independent of the power, therefore we expect a constant behavior. Thus, we can use a fit as

$$\omega_i = 2\pi \left(a_i + b_i(P - c_i)^d\right), \quad i = x, y, z,$$

where the fitting parameters a_i, b_i, and c_i depend on the coordinate. We use different calibrations for each of the frequency, choosing the best fit curves to the experimental points, based on the features provided by each of them in eq. (5.1.1). For example, ω_z depends only on power, then $c_z = 0$ while ω_x has a magnetic field component in this case

$c_x \neq 0$. The summary of the fittings obtained are in the Table 5.1. We also construct the corresponding graphs shown in Fig. (5.1.3).

Table 5.1 – Frequency fittings for hybrid trap

	a	$\pm\Delta a$	b	$\pm\Delta b$	c	$\pm\Delta c$	d
$\omega_x = 2\pi\times$	-7.74556	0	263.35245	2.13702	-0.02575	0.00172	$\frac{1}{2}$
$\omega_y = 2\pi\times$	21.16541	0.00533	0.94113	0.02371	0	0	1
$\omega_z = 2\pi\times$	-7.74556	0.25693	235.22088	0.84675	0	0	$\frac{1}{2}$

The y-axis frequency had less variation with the power because we kept fixed the magnetic gradient. An interesting test to be done is to calculate the gradient through a special low frequency value, i.e. $P = 0.29379\,\mathrm{W}$ equivalent to AO.1 = 2.7, where power effects are negligible. Thus, taking $\omega_y = 21.19\,\mathrm{rad}\cdot\mathrm{s}^{-1}$ and $z_0 = 300\,\mu\mathrm{m}$ approximately, we have

$$B'_x = \frac{2m\,|z_0|\,\omega_y^2}{\mu} \approx 16.55 \pm 2.56\,\mathrm{G}\cdot\mathrm{cm}^{-1},$$

which is within the estimated error for the gradient in the weak axis. The theoretical value was $14.95\,\mathrm{G}\cdot\mathrm{cm}^{-1}$ in the simulation, which corresponds to an error of 9.68%.

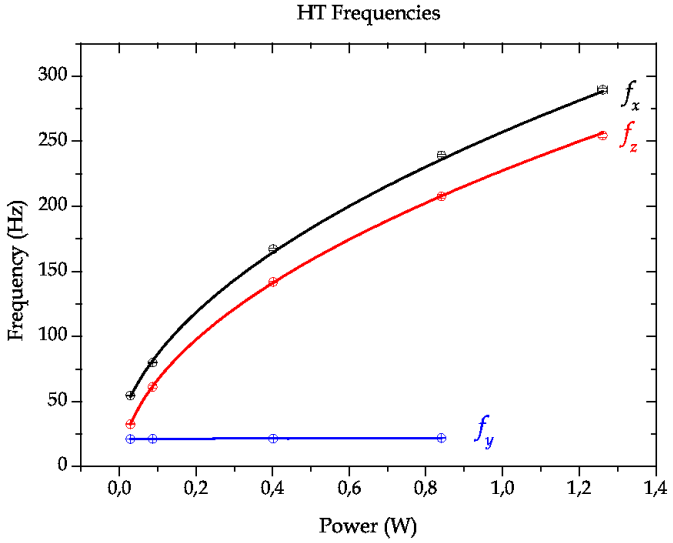

Figure 5.1.3 – Frequency calibrations as function of power. Source: elaborated by the author.

5.1.2 Volume parameter

Once frequencies have been calibrated, as we noticed in the previous section, we choose six different conditions performed with about 600 runs for each one, with which we build geometric means, which at the same time shall serve to define the parameters of volume. In this way each set of frequencies form a volume labeled as $\mathcal{V}_i$, where $i = 1, ..., 6$. We summarize the volume parameters in the Table 5.2, where each of them has its respective error propagation.

Table 5.2 – Frequencies and the volume parameter for the totally anisotropic 3D trap

	ω_x	$\pm\Delta\omega_x$	ω_y	$\pm\Delta\omega_y$	ω_z	$\pm\Delta\omega_z$
	$\text{rad}\cdot\text{s}^{-1}$	$\text{rad}\cdot\text{s}^{-1}$	$\text{rad}\cdot\text{s}^{-1}$	$\text{rad}\cdot\text{s}^{-1}$	$\text{rad}\cdot\text{s}^{-1}$	$\text{rad}\cdot\text{s}^{-1}$
$\mathcal{V}_1$	304.74	9.53	133.10	0.036	159.65	2.36
$\mathcal{V}_2$	1828.37	16.48	140.44	0.22	1611.00	7.59
$\mathcal{V}_3$	901.65	10.19	134.78	0.79	766.33	4.55
$\mathcal{V}_4$	506.79	8.75	133.50	0.046	387.09	3.18
$\mathcal{V}_5$	1175.87	11.86	136.07	0.078	1019.04	5.45
$\mathcal{V}_6$	678.06	9.14	133.97	0.058	555.55	3.79

Source: elaborated by the author.

The Table 5.3 summarizes the volume parameters obtained from the fitted frequencies of the Table 5.2. Note $\mathcal{V}_2 < \mathcal{V}_5 < \mathcal{V}_3 < \mathcal{V}_6 < \mathcal{V}_4 < \mathcal{V}_1$ which is an important relation for our analysis. The greatest variation of temperature and number of atoms was obtained by changing the time and power of optical evaporation. Often, volume parameters were reduced beyond the final value, to evaporate most of the cloud and achieve a higher fraction condensed, then this sample was re-compressed (with ramps of 200 to 800 ms) to the correct volume. The trapped atomic cloud was maintained for approximately 300 ms or more with aims of thermalization.

Table 5.3 – Volume parameters for the anisotropic 3D trap

	$\bar{\omega}^{(3D)}$	$\pm\Delta\bar{\omega}^{(3D)}$	$\mathcal{V}^{(3D)}$	$\pm\Delta\mathcal{V}^{(3D)}$
	$\text{rad}\cdot\text{s}^{-1}$	$\text{rad}\cdot\text{s}^{-1}$	s^3	s^3
$\mathcal{V}_1$	186.39	2.87	1.54×10^{-7}	7.16×10^{-9}
$\mathcal{V}_2$	745.11	3.80	2.42×10^{-9}	3.70×10^{-11}
$\mathcal{V}_3$	453.28	2.69	1.07×10^{-8}	1.91×10^{-10}
$\mathcal{V}_4$	296.97	2.55	3.82×10^{-8}	9.86×10^{-10}
$\mathcal{V}_5$	546.31	2.96	6.13×10^{-9}	9.97×10^{-11}
$\mathcal{V}_6$	369.55	2.55	1.98×10^{-8}	4.11×10^{-10}

Source: elaborated by the author.

In theory it is easy to do the cylindrical approximation, i.e. $\omega_x \simeq \omega_z = \omega_\rho$, however our trap is clearly anisotropic especially for low OT power. In this case, conveniently we can make the approximation of an average radius for the condensed cloud, so we adjust the dynamics to an average frequency[1], as follows:

$$\omega_\rho = \frac{1}{2}\left(\omega_x + \omega_z\right). \tag{5.1.3}$$

This approach greatly simplifies the calculations without losing much physical information, i.e. the final results are not very affected by the approximation. For practical reasons we use the approximation of cigar-shape (ω_ρ) for thermodynamic analysis in this thesis.

We must find a way to compare the frequencies ω_x and ω_y. For this purpose we can define a new quantity which we will call *anisotropy parameter* which has the following form :

$$\lambda_{\omega_i/\omega_j} = \frac{|\omega_i - \omega_j|}{(\omega_i\omega_j)^{\frac{1}{2}}}. \tag{5.1.4}$$

$\lambda_{\omega_i/\omega_j}$ meausure the degree of anisotropy in a trap. When $\lambda_{\omega_i/\omega_j} < 1$ we can do the approximation of the eq. (5.1.3). Besides this, $\lambda_{\omega_i/\omega_j}$ is calculated using the geometric mean of the frequencies in the denominator because it is very sensitive to differences. For example, in our experiment the higher anisotropy is in $\mathcal{V}_1$ with $\lambda^{(1)}_{\omega_z/\omega_x} = 0.66$, while the lowest is in $\mathcal{V}_2$ with $\lambda^{(2)}_{\omega_z/\omega_x} = 0.13$.

Using ω_ρ we have a new set of volume parameters which are shown in Table 5.4. the approximation of the eq. (5.1.3). Another interesting consequence, that somehow validates our approach is the geometric mean and the volume parameter. We can compare $\mathcal{V}_1^{(3D)}$ with $\mathcal{V}_1$ which is our asymmetric volume and see that the difference is only 10%.

Table 5.4 – Frequencies and the volume parameter in the cigar-shape approximation.

	ω_y	$\Delta\omega_y$	ω_ρ	$\Delta\omega_\rho$	$\bar{\omega}$	$\Delta\bar{\omega}$	$\mathcal{V}$	$\Delta\mathcal{V}$
	$\text{rad}\cdot\text{s}^{-1}$	$\text{rad}\cdot\text{s}^{-1}$	$\text{rad}\cdot\text{s}^{-1}$	$\text{rad}\cdot\text{s}^{-1}$	$\text{rad}\cdot\text{s}^{-1}$	$\text{rad}\cdot\text{s}^{-1}$	s^3	s^3
$\mathcal{V}_1$	133.10	0.036	232.20	5.95	192.89	3.31	1.39×10^{-7}	7.18×10^{-9}
$\mathcal{V}_2$	140.44	0.22	1719.68	12.00	746.10	3.87	2.41×10^{-9}	3.75×10^{-11}
$\mathcal{V}_3$	134.78	0.79	833.99	7.37	454.28	2.76	1.07×10^{-8}	1.95×10^{-10}
$\mathcal{V}_4$	133.50	0.046	446.94	5.96	298.76	2.69	3.75×10^{-8}	1.01×10^{-9}
$\mathcal{V}_5$	136.07	0.078	1097.45	8.66	547.22	3.03	6.10×10^{-9}	1.01×10^{-10}
$\mathcal{V}_6$	133.97	0.058	616.81	6.46	370.77	2.64	1.96×10^{-8}	4.20×10^{-10}

Source: elaborated by the author.

[1]We may also replace the arithmetic mean by the geometric mean, but the changes are insignificant.

5.2 Measuring the critical temperature

Determining and measuring the critical temperature (T_C) of an atomic sample in a harmonic potential is necessary for the haracterization of the system and the study of thermodynamics. We can determine the transition temperature, knowing the condensed fraction from eqs. (3.1.34) and (3.1.35). Thus, T_C depends essentially on two quantities: the oscillation frequencies and the number of atoms.

Experimentally for each volume, we group numbers of atoms in intervals, so that we can build graphics of the condensed fraction as a function of temperature and compare to eq. (3.1.35). We determine the critical temperature as a function of the total number of atoms using the eq. (3.1.34). Fig. 5.2.1-5.2.5 shows the experimental data points and the expression (3.1.34) using the Table 5.2. Let us note that this data analysis was performed using the expressions for the ideal gas, assuming that the behavior is quite close.

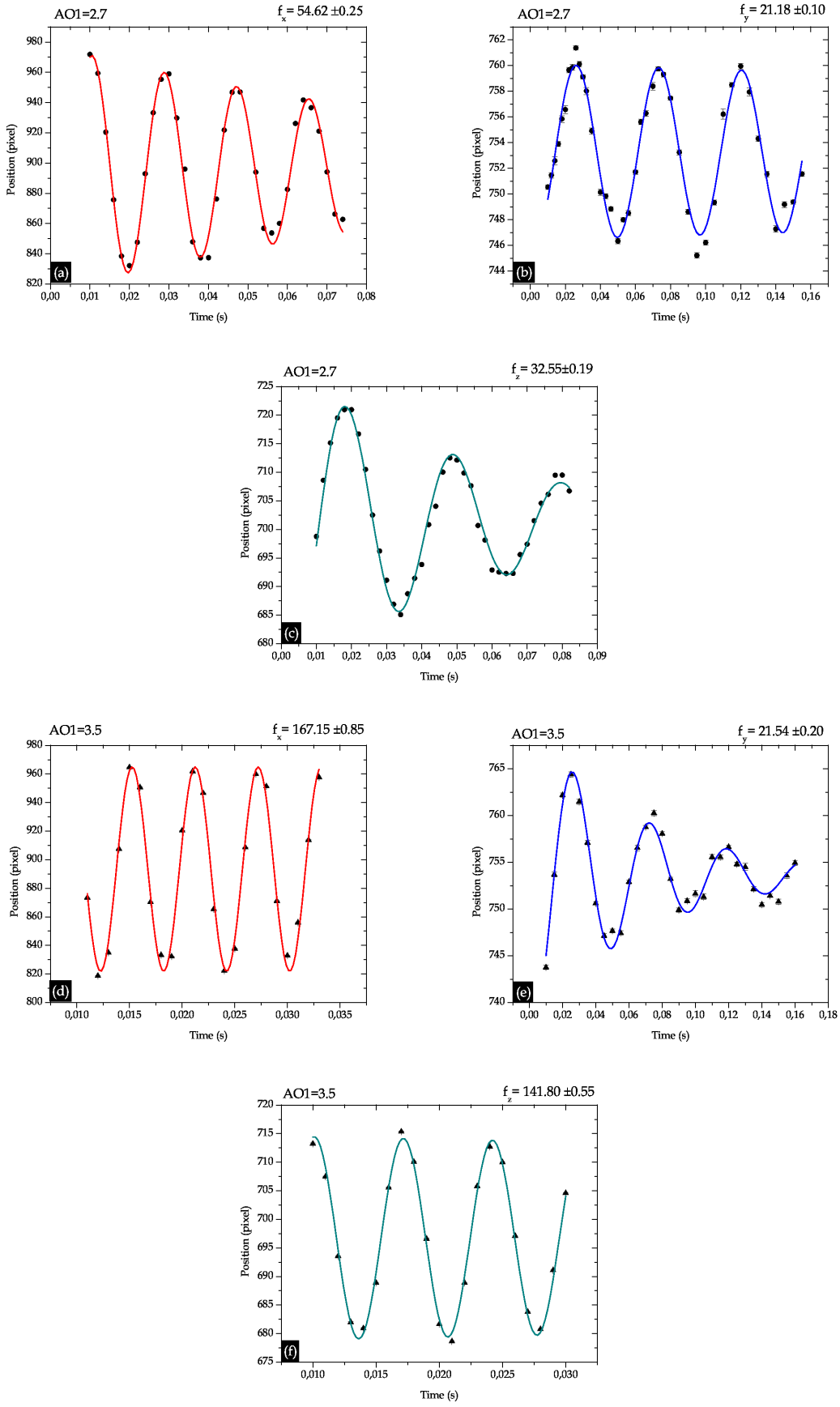

Figure 5.1.2 – Frequencies of the hybrid trap in the three directions for different power configurations: (a-c) 41.86 mW and (d-f) 401.66 mW. Source: elaborated by the author.

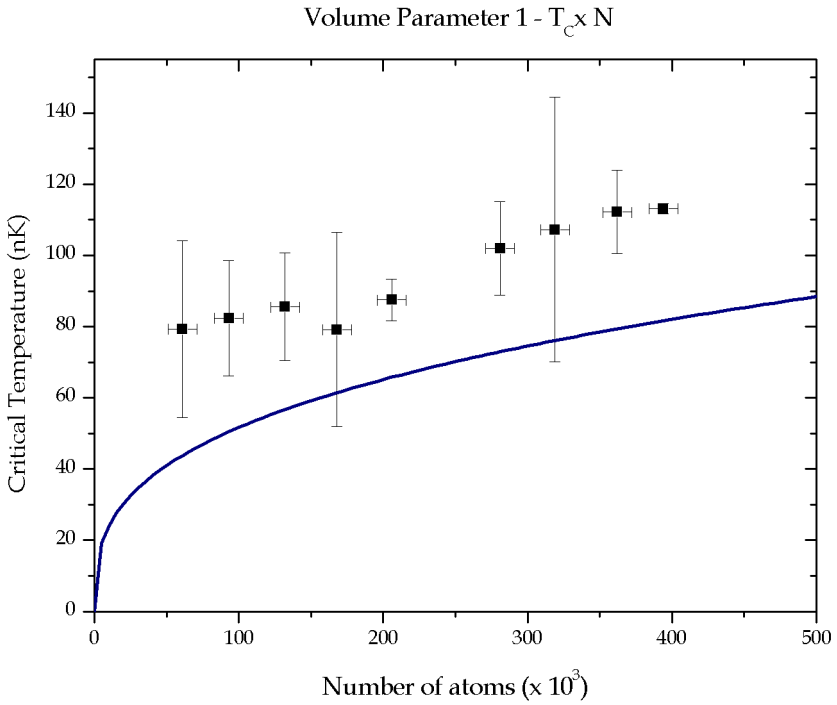

Figure 5.2.1 – Experimental data points and theoretical prediction (solid line) of critical temperature temperature as function of total number of atoms. Source: elaborated by the author.

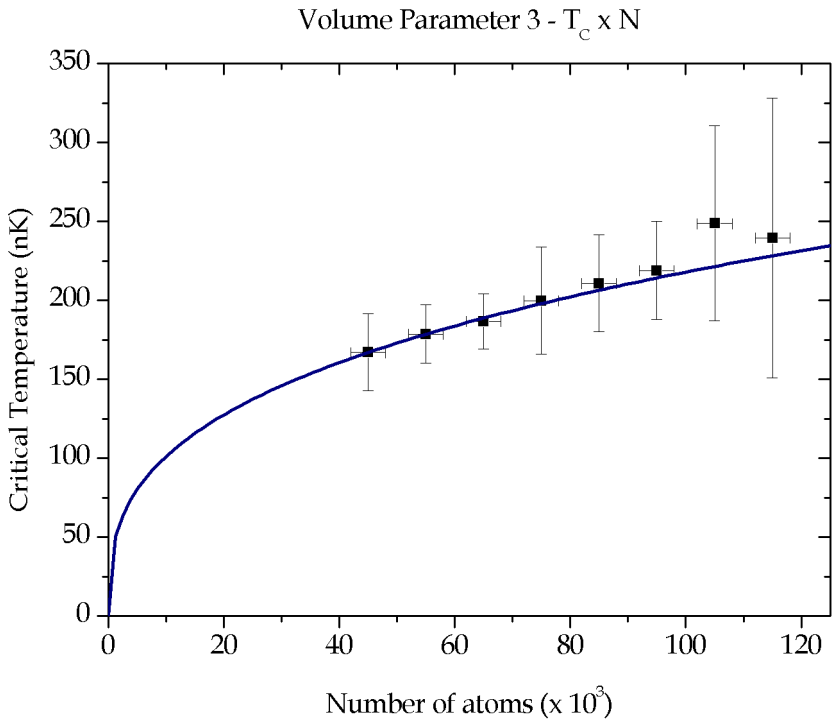

Figure 5.2.2 – Experimental data points and theoretical prediction (solid line) of critical temperature temperature as function of total number of atoms. Source: elaborated by the author.

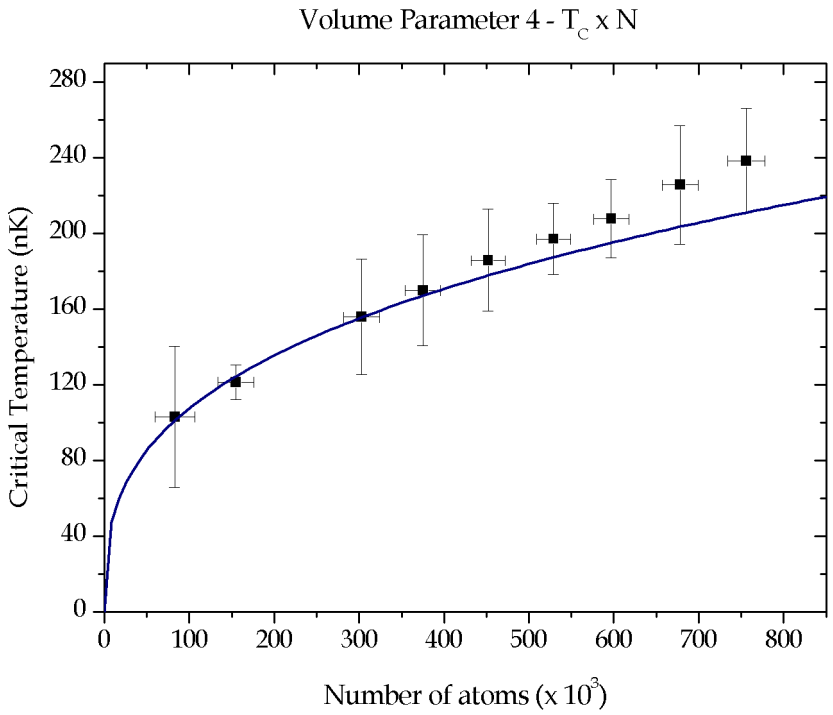

Figure 5.2.3 – Experimental data points and theoretical prediction (solid line) of critical temperature temperature as function of total number of atoms. Source: elaborated by the author.

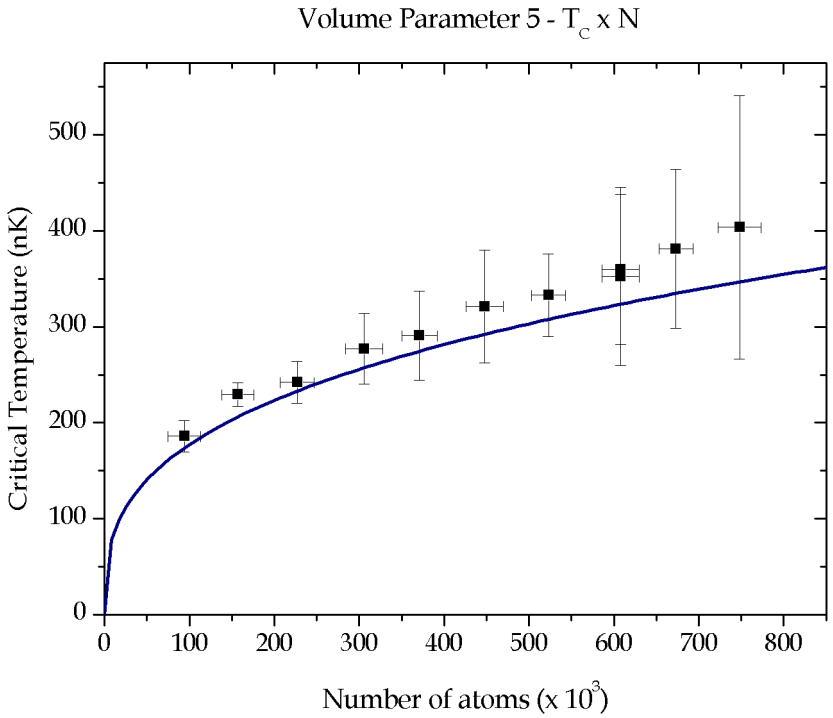

Figure 5.2.4 – Experimental data points and theoretical prediction (solid line) of critical temperature temperature as function of total number of atoms. Source: elaborated by the author.

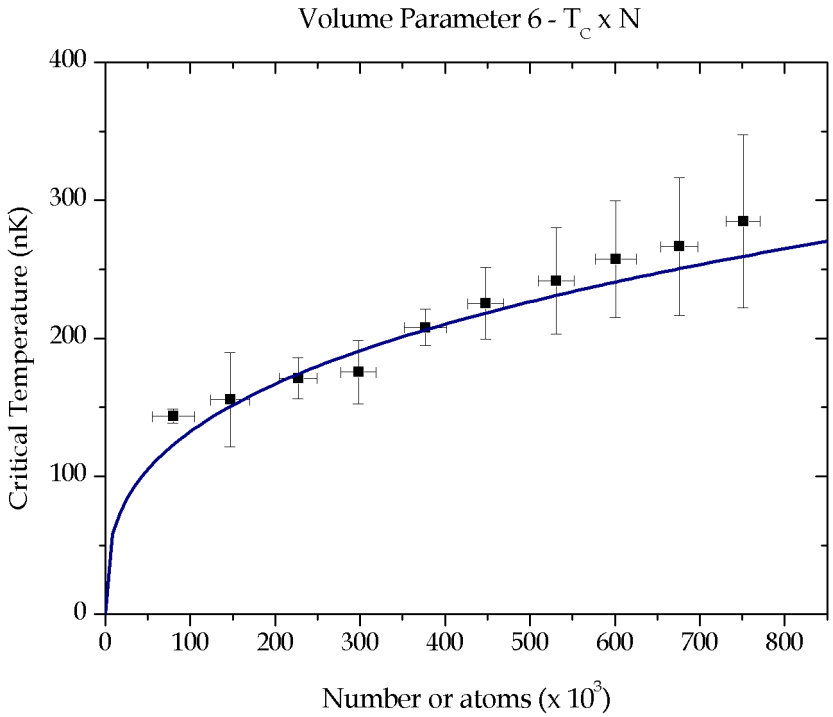

Figure 5.2.5 – Experimental data points and theoretical prediction (solid line) of critical temperature temperature as function of total number of atoms. Source: elaborated by the author.

Chapter 6

Pressure parameter and compressibility

To determine the pressure parameter Π of the equation (3.2.20), it is necessary to characterize and define two important quantities: the confinement potential and the atomic density. The external potential was discussed and characterized in the previous chapter. Consequently our first objective in this chapter is to obtain the density $n(\mathbf{r})$ from the experimental data. We explain how to recover the size of the sample inside the trap from images in free expansion.

Once the density is determined, we can calculate the pressure parameter. That will be used to construct the phase diagrams in terms of natural thermodynamic variables of the system, as the number of atoms and temperature. In the subsequent sections we study the evolution of this parameters using different phase diagrams. In the last section we will show how to obtain the isothermal compressibility parameter and some physical consequences of its behaviour.

6.1 Expansion dynamics

In a real situation, it is hard to produce completely pure condensates, in fact, there is a coexistence of atoms in the ground state and excited states, i.e., condensed and uncondensed part. The pressure parameter in the eq. (3.2.20) is a functional of density $n(\mathbf{r})$ and it must reflect this two-phase mixture, that is, the total atomic density is a superposition of two densities, which is knowed as *bimodal distribution*,

$$n(\mathbf{r}) = n_q(\mathbf{r}) + n_{th}(\mathbf{r}). \tag{6.1.1}$$

$n_q(\mathbf{r})$ corresponds to the density which has quantum degeneracy and $n_{th}(\mathbf{r})$ is the thermal density. Remember also that both clouds are in thermal equilibrium. Also, it is important to note that the equation for the pressure parameter indicates that information about interactions are embedded within the density.

The density corresponds to that inside the trapping potential; then the thermodynamic analysis of the cloud should be inside the trap. In the literature it is commonly called *in situ* sample. Usually, inside the trap the optical density of the bosonic ultra-cold sample is too high for a reliable absorption image, i.e. without defects or artifacts. The free expansion decreases the optical density so that the image is not saturated. Our system has not *in situ* image diagnosis (12, 79, 100) but this does not mean that the density cannot be analyze. We also have an important advantage: the TOF has a advantage that the fit allows us to measure directly the temperature. All diagnoses of the sample are made using absorption imaging on a CCD camera after 21 ms of TOF.

In this section we explain the procedures to recover the dimensions of the cloud in situ from images taken in time of flight. The evolution of the expanding cloud has been extensively studied in the literature for both thermal (48, 47) to the condensed part (101, 102). All dynamic procedures require knoledge of the trap frequencies, that were already characterized in the previous chapter to perform this task also.

6.1.1 Thermal cloud

The density of the thermal cloud obeys a gaussian distribution approximation (103)[1]

$$n_{th}(\mathbf{r}) = \frac{N_{th}}{(2\pi)^{3/2}\sigma_x^0\sigma_y^0\sigma_z^0}\exp\left[-\frac{1}{2}\left(\frac{x}{\sigma_x^0}\right)^2-\frac{1}{2}\left(\frac{y}{\sigma_y^0}\right)^2-\frac{1}{2}\left(\frac{z}{\sigma_z^0}\right)^2\right] \tag{6.1.2}$$

where σ_x^0, σ_y^0, and σ_z^0 are the insitu widths. N_{th} corresponds to non-condensed number of particles. Let us remember that this distribution was integrated along an axis and as a result we have a two-dimensional Gaussian distribution in eq. (4.4.2).

When the trap is switched off, the atoms fly ballistically in every direction with resulting in an isotropic expansion for long times. In this particular case, the virial theorem allows us to recover easily the dimensions of the *in situ* thermal cloud from the images with TOF. The virial theorem provides a general equation relating the total kinetic energy (temperature) with the total potential energy (the external forces). The external force in this case comes from a harmonic potential, then:

$$2\langle E_k\rangle = \langle \mathbf{r}.\nabla U\rangle = \left\langle m\omega^2 r^2\right\rangle.$$

The E_k provides the width in TOF σ_i and $\langle \mathbf{r}.\nabla U\rangle$ provides the width in situ σ_i^0. In this way we have:

$$\sigma_i^0 = \frac{\sigma_i}{\omega_i t_{exp}}, \tag{6.1.3}$$

where ω_i is the frequency in the i-direction and t_{exp} is the time expansion of the thermal

[1] The gaussian distribution is a approximation because the Bose statistics distort the density.

cloud. Note that σ_i is related with the temperature as seen in eq. (4.4.5). This expression also shows that the shape of the distribution is preserved (104) and the width only have a scale factor.

6.1.2 Condensed cloud

A pure quantum degenerated cloud obeys the GPE, where the interaction energy is much stronger than the kinetic energy, and therefore it is represented by the Thomas-Fermi distribution

$$n_q(\mathbf{r}) = \frac{15N_0}{8\pi R_x^0 R_y^0 R_z^0} \max\left[1 - \left(\frac{x}{R_x^0}\right)^2 - \left(\frac{y}{R_y^0}\right)^2 - \left(\frac{z}{R_z^0}\right)^2, 0\right], \tag{6.1.4}$$

where R_x^0, R_y^0, and R_z^0 are in situ Thomas-Fermi radii. N_0 is the condensed number of particles. The distribution integrated along one direction results in eq. (4.4.2).

The free expansion for the condensate is dominated by interactions and the dynamical response is very different to thermal cloud. When the trapping potential is anisotropic the expansion is anisotropic too, since it is related with the interaction energy that is converted in to kinetic energy. Thus, the inversion of the aspect ratio is the most evident behavior of the expansion of a condensate.

A good assumption is that the functional form of the density is preserved when the cloud is released from the trap. Then, as in the thermal cloud we need to know the scale parameter of the in situ condensate radius R_i^0's, which is

$$R_i(t) = R_i^0 b_i(t) = \sqrt{\frac{2\mu}{m\omega_i(0)}} b_i(t). \tag{6.1.5}$$

where μ is the chemical potential and $\omega_i(0)$ is the frequency in the i-direction ($i = x, y, z$). The time dependent scaling factor $b_i(t)$ has the initial conditions

$$b_i(0) = 1, \;\; \dot{b}_i(0) = 0. \tag{6.1.6}$$

Using the time dependent GPE (102), we obtain the dynamics of $b_i(t)$ governed by the differential equation

$$\ddot{b}_i(t) + \omega_i^2(t) b_i(t) = \frac{\omega_i^2(0)}{b_i(t) b_x(t) b_y(t) b_z(t)}, \tag{6.1.7}$$

which requires a numerical solution. However, in the cigar-shape trap symmetry where two trap frequencies are approximately equal, the equation has an analytical solution (101). In the specific case of hybrid trap, we have three different frequencies, hence a simulation for 600 data for each volume parameter takes a long time.

We can compare the aspect ratio inversion after 21 ms of TOF for each $\mathcal{V}_i^{(3D)}$ with $\mathcal{V}_i$ of Table 5.3 and Table 5.4, respectively. The results are shown in the Fig. 6.1.1, where we plotted $R_z(t)/R_y(t)$ in the anistropic case, and $R_\rho(t)/R_y(t)$ in the cigar-shape approximation. This result does not show a significant difference in the inversion aspect with the exception of the first volume parameter $\mathcal{V}_1^{(3D)}$ with $\mathcal{V}_1$. The behavior for this volume was already expected, since lambda is $\lambda^{(1)}_{\omega_z/\omega_x} = 0.66$, but for thermodynamics what matters is the geometric mean and the product of the Thomas-Fermi radius with its corresponding frequency $(\omega_i R_i)$, as discussed below.

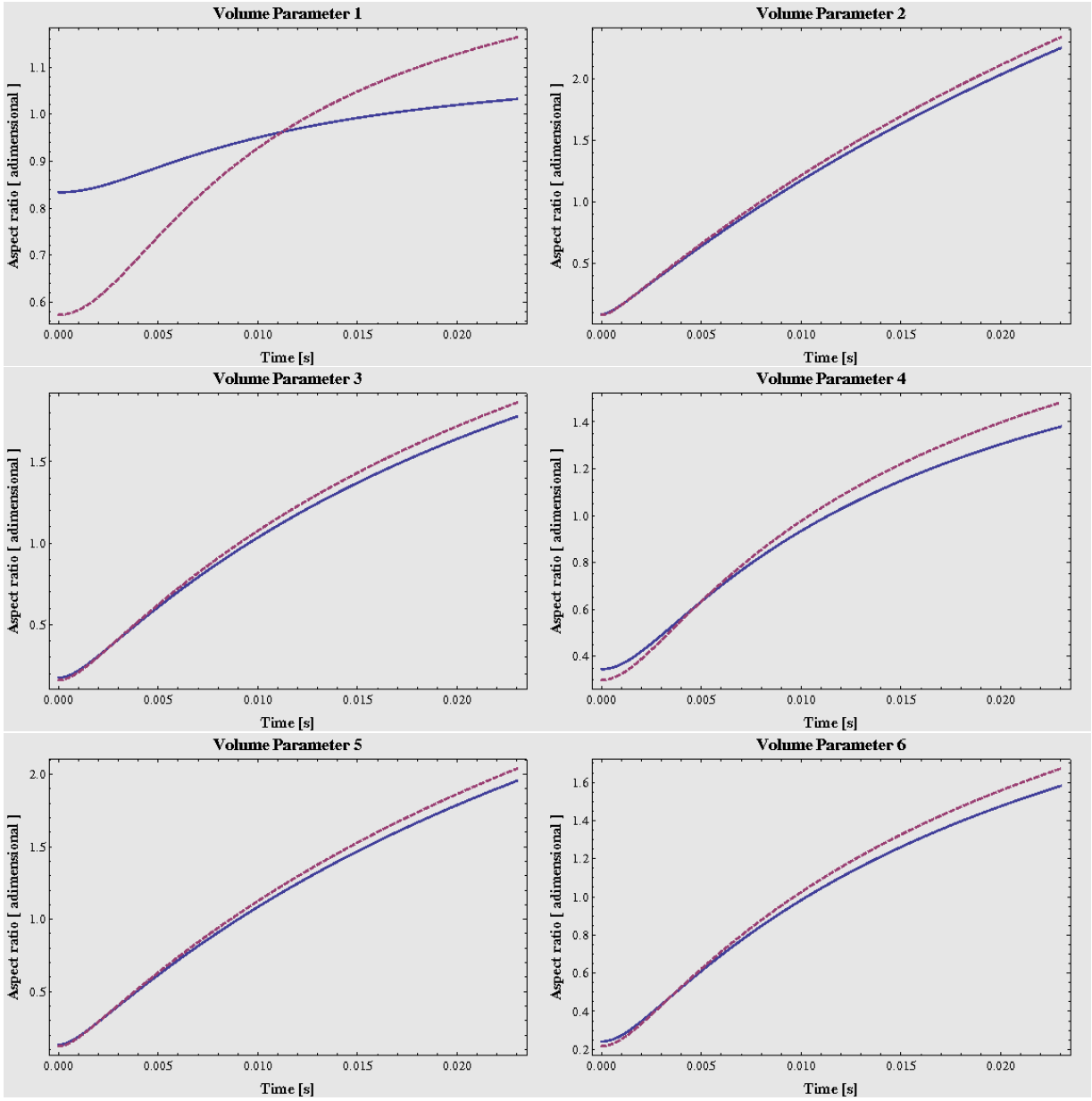

Figure 6.1.1 – Aspect ratio for each volume parameter as a function of time of flight: $R_z(t)/R_y(t)$ in the anistropic case (solid lines), and $R_\rho(t)/R_y(t)$ in the cigar-shape approximation (dashed lines). Source: Elaborated by the author.

6.2 Pressure parameter

We know that the density is bimodal then the pressure parameter in the eq. (3.2.20) is the sum of partial pressure parameters:

$$\Pi = \Pi_q + \Pi_{th} = \int d^3r\, n_q\left(\mathbf{r}\right) U\left(\mathbf{r}\right) + \int d^3r\, n_{th}\left(\mathbf{r}\right) U\left(\mathbf{r}\right). \tag{6.2.1}$$

The form of Π is completely analytics, replacing the harmonic potential and using the densities of eqs. (6.1.2) and (6.1.4), we obtain

$$\Pi_q^{(3D)} = \frac{mN_0}{21\mathcal{V}}\left(\omega_x^2\left(R_x^0\right)^2 + \omega_y^2\left(R_y^0\right)^2 + \omega_z^2\left(R_z^0\right)^2\right), \tag{6.2.2}$$

$$\Pi_{th}^{(3D)} = \frac{mN_{th}}{3\mathcal{V}}\left(\omega_x^2\left(\sigma_x^0\right)^2 + \omega_y^2\left(\sigma_y^0\right)^2 + \omega_z^2\left(\sigma_z^0\right)^2\right). \tag{6.2.3}$$

Again we have to validate our approach (5.1.3), especially for condensed cloud. In this form, we have

$$\Pi_q = \frac{mN_0}{21\mathcal{V}}\left(2\omega_\rho^2\left(R_\rho^0\right)^2 + \omega_y^2\left(R_y^0\right)^2\right), \tag{6.2.4}$$

$$\Pi_{th} = \frac{mN_{th}}{3\mathcal{V}}\left(2\omega_\rho^2\left(\sigma_\rho^0\right)^2 + \omega_y^2\left(\sigma_y^0\right)^2\right). \tag{6.2.5}$$

The difference between Π_0 and $\Pi_0^{(3D)}$ is hardly 7% for the extreme case $\mathcal{V}_1$ vs. $\mathcal{V}_1^{(3D)}$, this result does not alter the qualitative results of the pressure and phase diagrams. This leads us to believe that the pressure parameter is truly global and it does not depend on quantum behavior.

The eq. (6.2.5) is totally equivalent to equation of state for an ideal Bose gase. This fact can be verified using the equipartition theorem, where $\frac{1}{2}m\omega_i^2\sigma_i^2 = \frac{1}{2}k_BT$, then

$$\Pi_{th}\mathcal{V} = N_{th}k_BT, \tag{6.2.6}$$

that relates all state variables defined in this formalism.

We can find an equation similar to the equation of state (6.2.6) for the bimodal phase. We use the TFA for the condensate fraction besides the expression (3.2.14), the condensate fraction (3.1.35), and the critical temperature (3.1.34). Substituing all expression in the eq. (6.2.4) we arrive at a completely analytical expression for $\Pi_q(N/\mathcal{V}, T)$:

$$\Pi_q = \frac{1}{7}\left[15a_s\hbar^2\sqrt{m}\left[\frac{N}{\mathcal{V}} - \left(\frac{k_BT}{0.94\hbar}\right)^3\right]^{7/2}\right]^{2/5} \tag{6.2.7}$$

6.3 Phase diagrams

The usual representation in equilibrium thermodynamics for the phase diagram is a chart of the different phases. The phases are typically delimited by equilibrium lines where two or more phases can coexist in thermodynamic equilibrium. When we mention phases in this thesis we refer to the property of the bosons to occupy the ground state and excited states, i.e. a quantum phase and classical phase, respectively. The equilibrium lines in this kind of system are typically represented by critical lines where quantum degeneresence begins to occur. A *phase transition* occurs when we go from one region to another through a critical line.

After defining the appropriate thermodynamic quantities, we study the evolution of these parameters using different phase diagrams $\Pi \times T$, $\Pi \times N$, $\Pi \times \mathcal{V}$, etc, where we leave fixed a few parameters, that gives isothermal, isochoric, isodensity, etc. diagrams. The theoretical diagrams can be found in refs. (43, 1) and the Fig. , where it is possible to determine the phase transition from thermal cloud to condensed cloud.

In a previous experimental work of our group in ref. (37) it was apresented the transition in a $\Pi \times T$ phase diagram (isodensity), agreeing with theoretical predictions. In that experiment (37) the volume parameter is fixed.

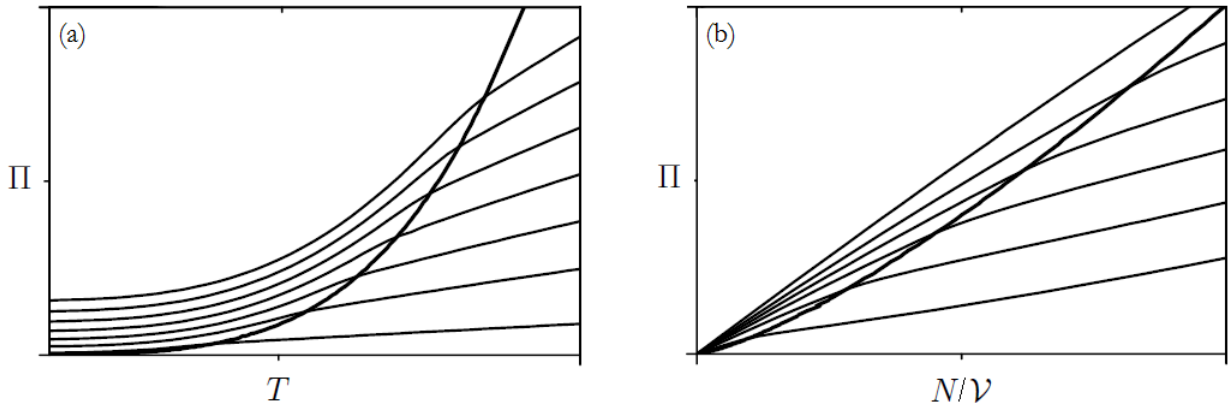

Figure 6.3.1 – Phase diagramas for a Bose gas in a harmonic trap, where it shows the (a) isochoric curves and (b) isodensity curves. Source: Elaborated by Romero-Rochín in the Ref. (1)

6.3.1 Isodensity

We know that the parameter Π is a function of number of particles N, temperature T, and volume parameter $\mathcal{V}$. It is possible to construct a $\Pi \times T$ diagram grouping sets of number of atoms for each volume, i.e. we maintain $N/\mathcal{V}$ fixed. $N/\mathcal{V}$ is equivalent to N/V in usual phase diagrams in the literature, for this reason we call isodensity curves. The diagrams for these curves are shown in Figs. 6.3.2-6.3.6.

Each chart in Fig. 6.3.2 represents a $\Pi \times T$ diagram for the volume parameters $\mathcal{V}_1$ to $\mathcal{V}_6$, respectively (see table 5.4). We expect that above the critical temperature ($T > T_C$) the interactions are negligible, so that Π shall be linear with temperature because it obeys the equation of state of an ideal gas, eq. (6.2.6). The charts in Figs. 6.3.2-6.3.6 shows the thermal phase (gray dots) following the theoretical behavior of the ideal gas (dotted lines). The density of the experimental points in the charts is very high, therefore we can see the complete charts in the appendix **A**. On the other hand, below the critical temperature ($T < T_C$) the interaction effects are remarkable and the parameter pressure begins to be affected. The isodensity curves drop due to the atoms that begin to occupy the ground state. Crossing below T_C in Figs. 6.3.2-6.3.6, the bicomponent phase (color dots) is extrapoled with a exponential fitting (solid lines). We can comparate the theoretical and experimental phase diagrams using the Fig. 6.3.1 and Figs. 6.3.2-6.3.6, respectively. Note that extrapolation shows that Π is not zero for $T \to 0$ due to the role of interactions, as predicted by Romero-Rochín in the ref. (1). We shall discuss this fact in a subsequent chapter.

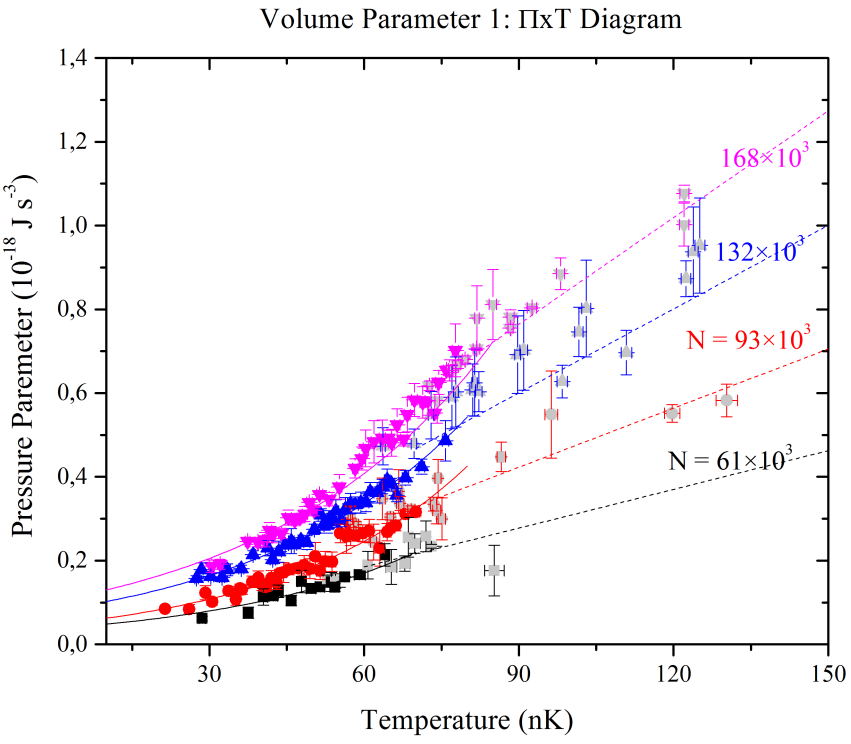

Figure 6.3.2 – $\Pi \times T$ diagram for $\mathcal{V}_1$. The thermal phase in gray dots follows the behavior of ideal gas in dotted lines. The quantum phase in color dots creates a depletion on the curve because the atoms begin to fill the ground state. The best fit for the lines in quantum phase are fittings of a exponential function. Source: Elaborated by the author.

We can extract the critical values for each isodensity curve as shown in the example

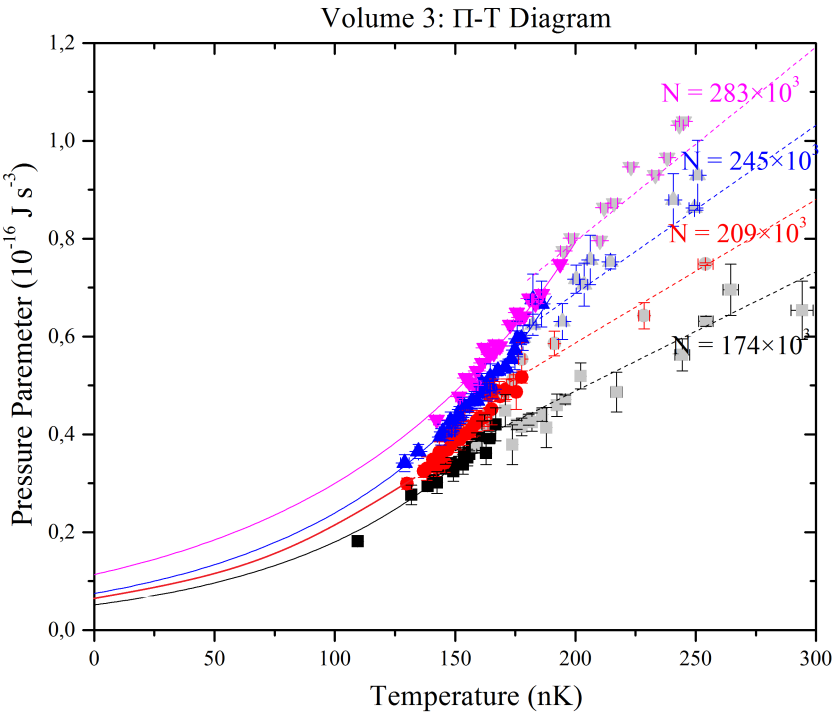

Figure 6.3.3 – $\Pi \times T$ diagram for $\mathcal{V}_3$. The thermal phase in gray dots follows the behavior of ideal gas in dotted lines. The quantum phase in color dots creates a depletion on the curve because the atoms begin to fill the ground state. The best fit for the lines in quantum phase are fittings of a exponential function. Source: Elaborated by the author.

of Fig. 6.3.7 from Fig. 6.3.4. We build a critical transition line as seen in eq. (3.1.36), collecting each pair (T_C, Π_C) for each isodensity curve.

An interesting point about the expression of critical line is

$$\Pi_C = \left(3.34284 \times 10^{10}\right) T_C^4 \rightarrow \Pi T^{-4} = \text{const.}$$

which is independent of volume parameter and number of atoms. By taking all critical points of all volume parameters and plotting them in the same chart we obtain the Fig. 6.3.8. Our results evidence that the critical line highlights the limit transition from a classical gas to degenerated quantum gas (solid line). This line reminds us the famous λ-transition in ^{4}He, that represents the phase transformation from liquid to superfluid (105). The order of the phase transition in ^{4}He has been widely discussed in the Refs. (106, 107), which in bulk systems is believed to be of second order. Thus, for a harmonically confined gas the equivalent to λ-line (if we calculate the thermal compressibility) also indicates that a transformation is "continuous", however transition order requires a more delicate study.

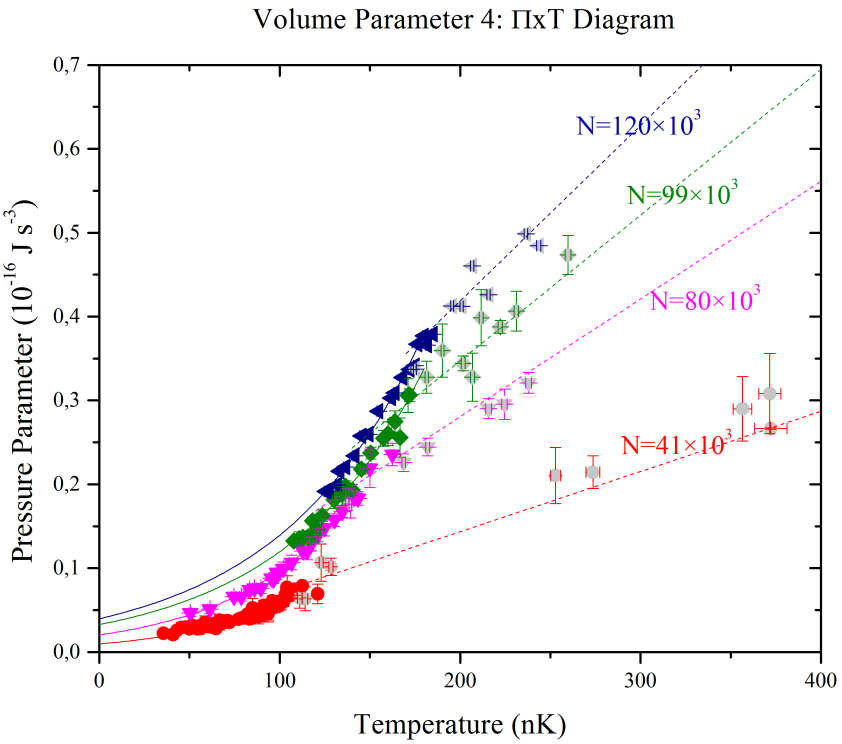

Figure 6.3.4 – $\Pi \times T$ diagram for $\mathcal{V}_4$. The thermal phase in gray dots follows the behavior of ideal gas in dotted lines. The quantum phase in color dots creates a depletion on the curve because the atoms begin to fill the ground state. The best fit for the lines in quantum phase are fittings of a exponential function. Source: Elaborated by the author.

6.3.2 Isothermal

Since Π is a function $\Pi\left(N/\mathcal{V}, T\right)$ we can make $\Pi \times N$ diagrams as showed in Fig. 6.3.9-6.3.11. The isothermal plots, in the same way $\Pi \times T$ diagrams, show the transition from the quantum phase regime to the classical regime. In this case we group sets of temperature for each volume for different number of atoms.

The pressure parameter is linear with the number below a critical number, ie $N < N_C$. This fact is expected since the BEC phenomenon depends on phase space density. This means that, if we keep the volume parameter constant and increase the number, the system will find a way to fill the ground state to keep the temperature, and the result is BEC. Once again, interactions dominate above the critical number ($N > N_C$). In this diagrams the transition line obeys the relation for an ideal gas, $\Pi N^{-4/3} = \text{const}$.

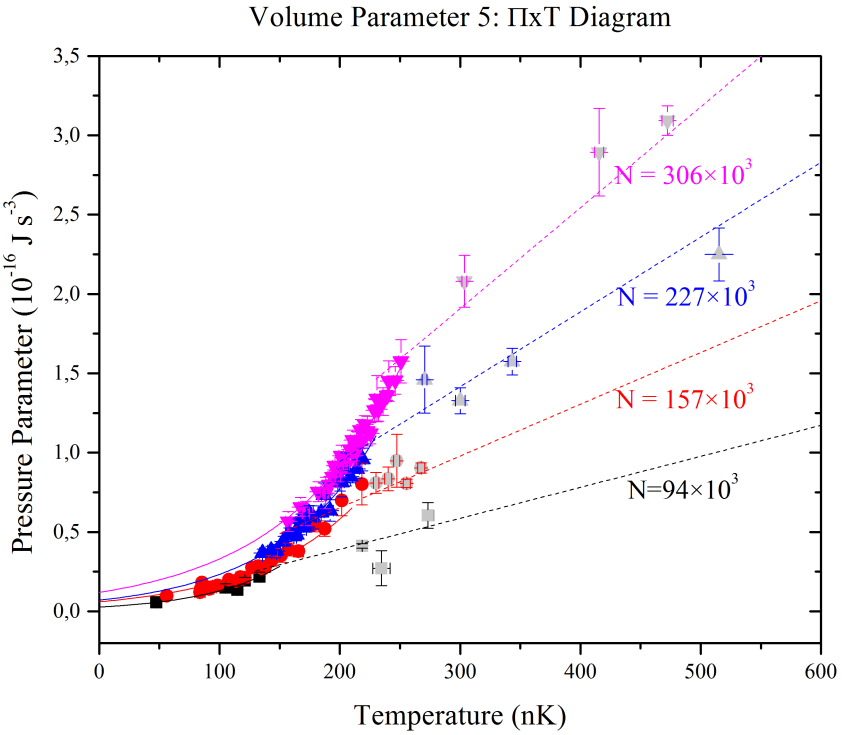

Figure 6.3.5 – $\Pi \times T$ diagram for $\mathcal{V}_5$. Source: elaborated by the author.

6.4 Compressibility

As was already mentioned changes in the system due to any external force result in a change of temperature or displacement force. These changes can be represented by several thermodynamic quantities that show the mechanical response, thermal compressibility is one of them. In ^{4}He, e.g. the phase transformation is caracterized by divergence in the isothermal compresibility and represents an evidence of a second-order phase transition (108). Analogously, we can define the isothermal compressibility parameter k_T as a function $k_T\left(N/\mathcal{V}, \Pi\right)$.

First, we consider the behavior of k_T along the transition to a condensed phase considering an ideal gas. The isothermal compressibility is given by

$$k_T = -\frac{1}{\mathcal{V}}\left(\frac{\partial \mathcal{V}}{\partial \Pi}\right)_{T,N} = \frac{\mathcal{V}}{N^2}\left(\frac{\partial N}{\partial \mu}\right)_{T,\mathcal{V}} = \frac{\mathcal{V}}{N k_B T}\frac{g_2\left(z\right)}{g_3\left(z\right)} \tag{6.4.1}$$

for $T > T_C^+$, where we used the Maxwell relations of thermodynamics. k_T for high temperatures have the Curie law-like behavior of an ideal classical gas. Note that $g_2\left(1\right) = \pi^2/6$ around the critical temperature. Since k_T is related to the density or particle fluctuations, relating the eqs. (3.1.37) and (6.4.1)

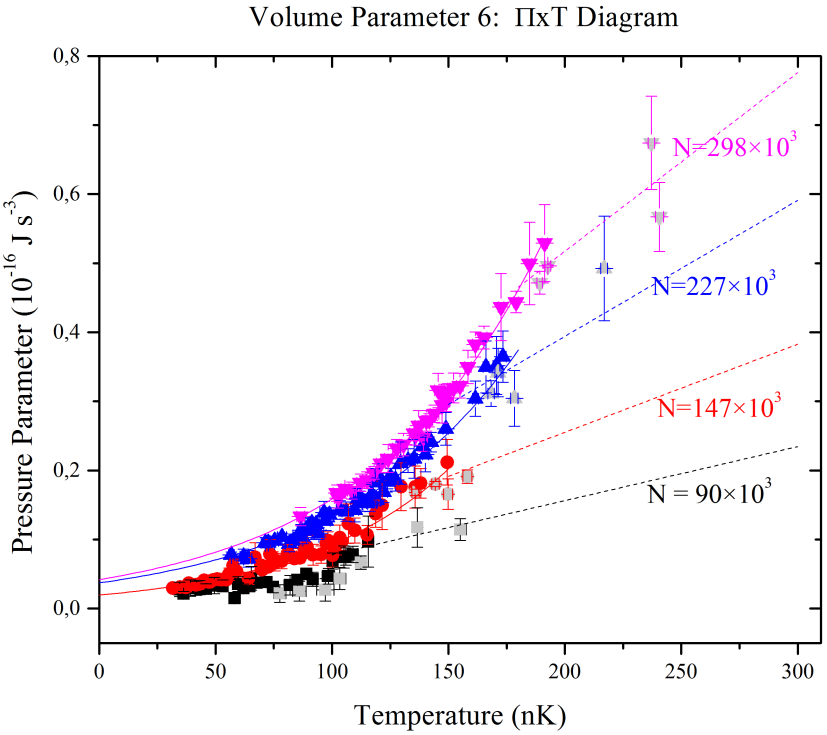

Figure 6.3.6 – $\Pi \times T$ diagram for $\mathcal{V}_6$. The thermal phase in gray dots follows the behavior of ideal gas in dotted lines. The quantum phase in color dots creates a depletion on the curve because the atoms begin to fill the ground state. The best fit for the lines in quantum phase are fittings of a exponential function. Source: Elaborated by the author.

$$k_T = \frac{\mathcal{V}}{N}\left(\frac{\partial \Pi}{\partial\,(N/\mathcal{V})}\right)^{-1} = \frac{1}{k_B T}\frac{\mathcal{V}}{N}\frac{\Delta^2 N}{N}. \tag{6.4.2}$$

A stable equilibrium system requires that its compressibility be positive and finite, $0 < k_T < \infty$. This restriction was extensively studied by Yukalov in references (109, 110). Yukalov indicates that the ideal uniform Bose gas is unstable, since it has anomalous fluctuations. The opposite case to the instability of the ideal gas is the interacting gas, which always has only normal fluctuations. This happens a similar manner to a BEC inside an external potential, i.e. a non-uniform gas.

The pressure parameter variation as a function of $N/\mathcal{V}$ can be experimentally obtained. In this way we are able to get k_T. Now, we have a phase diagram for $k_T \times T$ from Fig. 6.3.9, e.g. taking $\mathcal{V}_4$ we obtain the Fig. 6.4.1. Below T_C, the behavior of the compressibility parameter changes when the interactions start to dominate.

Taking up again the argument about the order of the phase transition, according to Paul Ehrenfest, phase changes can be ranked by the free energy derivative. Thus, they can be classified into two classes: the first one which are accompanied by a discontinuous changes of state (first order derivative) are called first-order phase transitions; and the

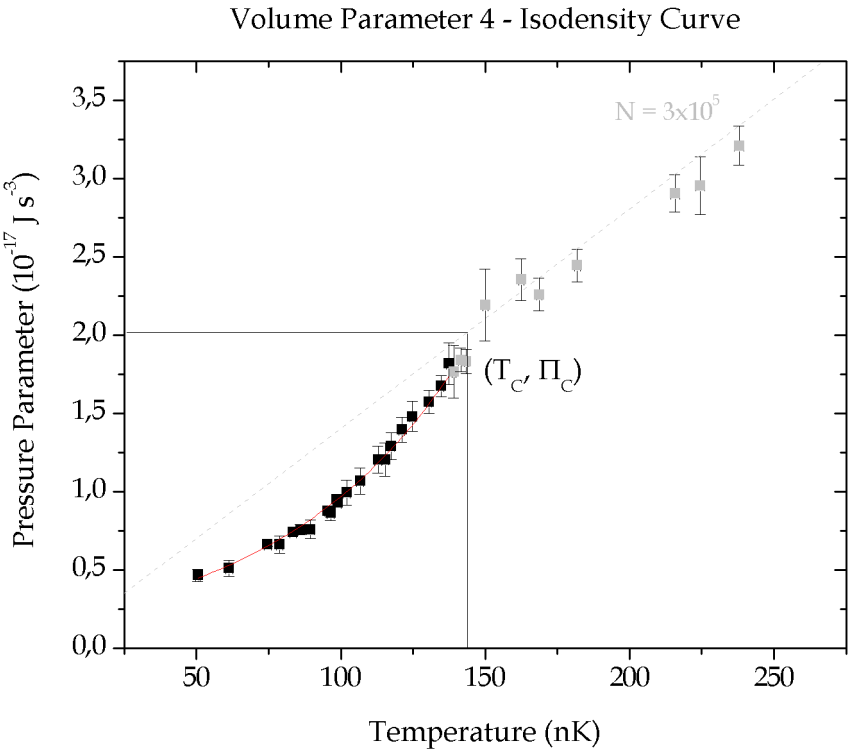

Figure 6.3.7 – Isodensity curve ($N = 3.03 \times 10^5$) for $\mathcal{V}_4$ showing the critical values Π_C and T_C. Source: elaborated by the author.

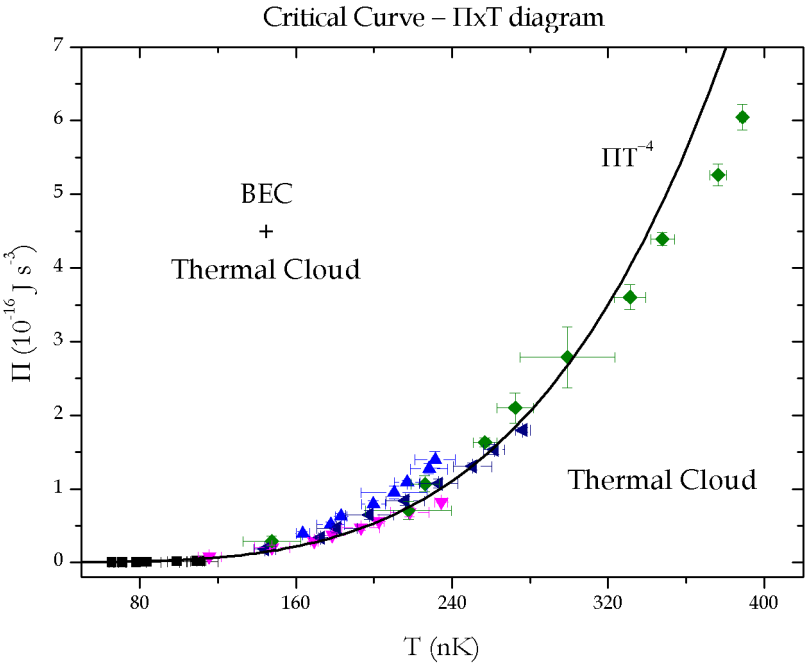

Figure 6.3.8 – $\Pi \times T$ diagram of the BEC transition. Source: elaborated by the author.

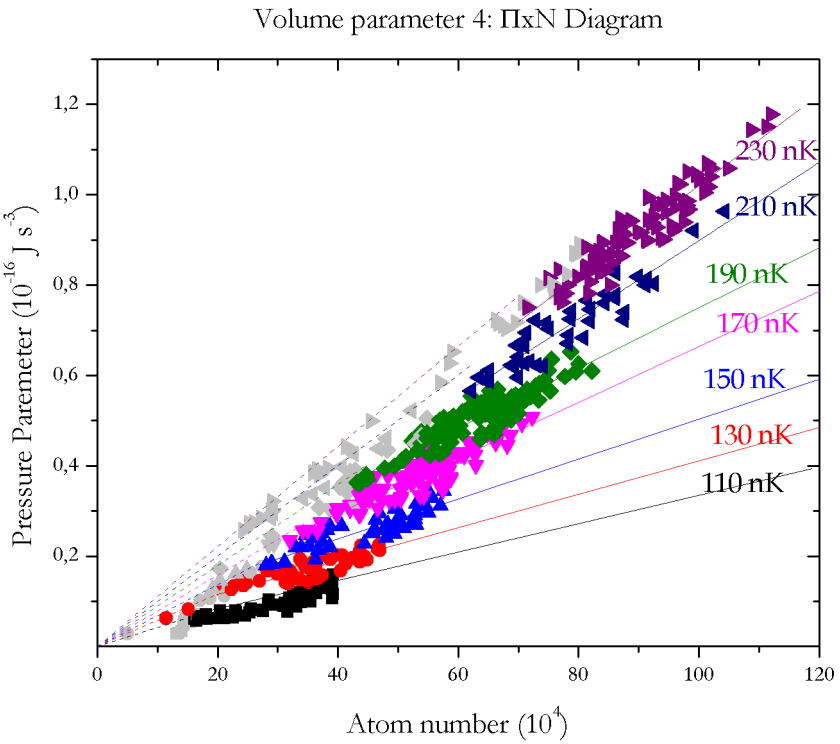

Figure 6.3.9 – $\Pi \times N$ diagram for $\mathcal{V}_4$. The thermal phase ($N < N_C$) in gray dots follows a linear behavior of an ideal gas. On the other hand, the quantum phase ($N > N_C$) in color dots has a different behavior to classical regime. Source: Elaborated by the author.

second one transitions which are accompanied by a continuous changes of state are called continuous phase transitions (discontinuous higher-order derivatives).

In phase transitions, if one of the free energies diverge, we can say that the others also diverge in the same way that its derivatives. In our case, we have:

$$\begin{aligned}\left(\frac{\partial k_T}{\partial T}\right)_{N/\mathcal{V}} &= -\left(\frac{N}{\mathcal{V}k_T}\right)^2 \frac{\partial^3}{\partial T \partial \left(N/\mathcal{V}\right)^2}\left(\frac{G}{\mathcal{V}}\right) \\ &= \left(\frac{N}{\mathcal{V}}\right)^2 \frac{k_B^2 T}{\hbar^3}\frac{1}{g_2(z)}\left\{2g_2^2(z) - 3g_1(z)\, g_3(z)\right\}, \end{aligned} \tag{6.4.3}$$

where G is the Gibbs energy. The eq. (6.4.3) indicates a divergence in second derivate of Gibbs energy because $g_1(1) \to \infty$, around the critical temperature.

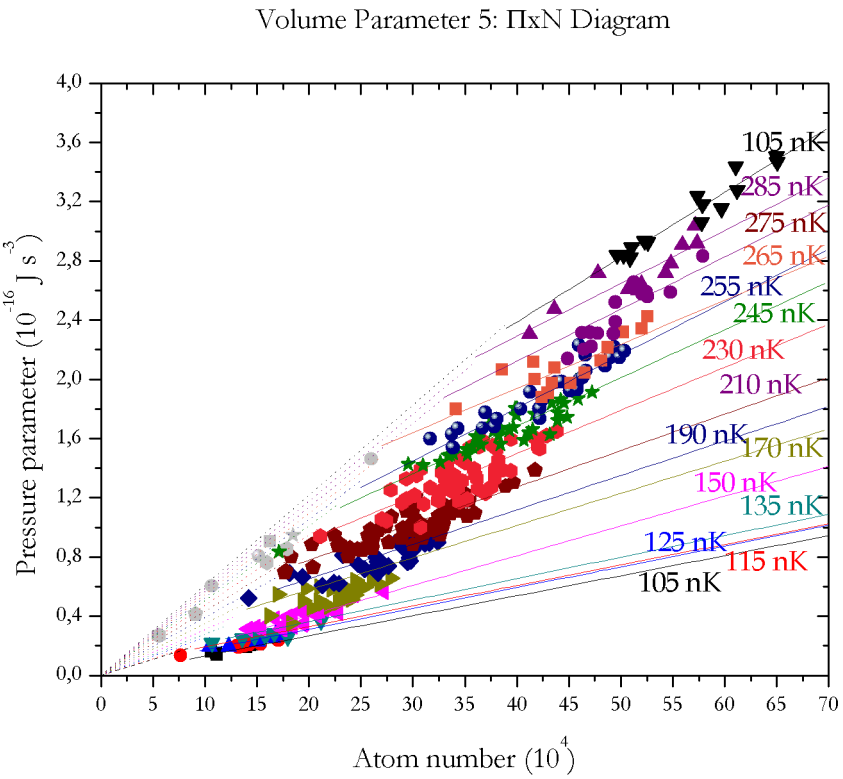

Figure 6.3.10 – $\Pi \times N$ diagram for $\mathcal{V}_5$. The thermal phase ($N < N_C$) in gray dots follows a linear behavior of an ideal gas. On the other hand, the quantum phase ($N > N_C$) in color dots has a different behavior to classical regime. Source: Elaborated by the author.

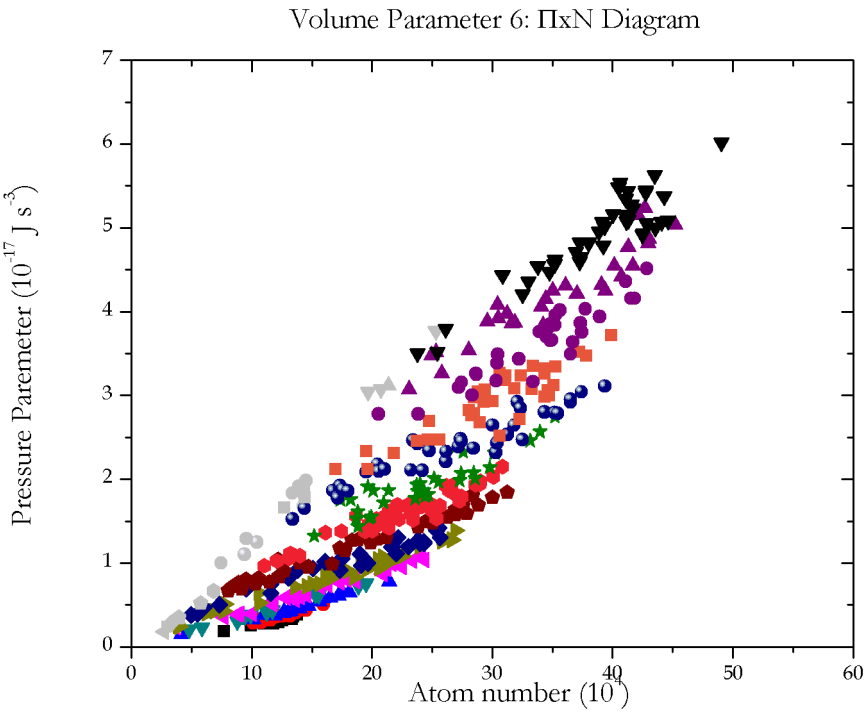

Figure 6.3.11 – $\Pi \times N$ diagram for $\mathcal{V}_6$. The thermal phase ($N < N_C$) in gray dots follows a linear behavior of an ideal gas. On the other hand, the quantum phase ($N > N_C$) in color dots has a different behavior to classical regime. Source: Elaborated by the author.

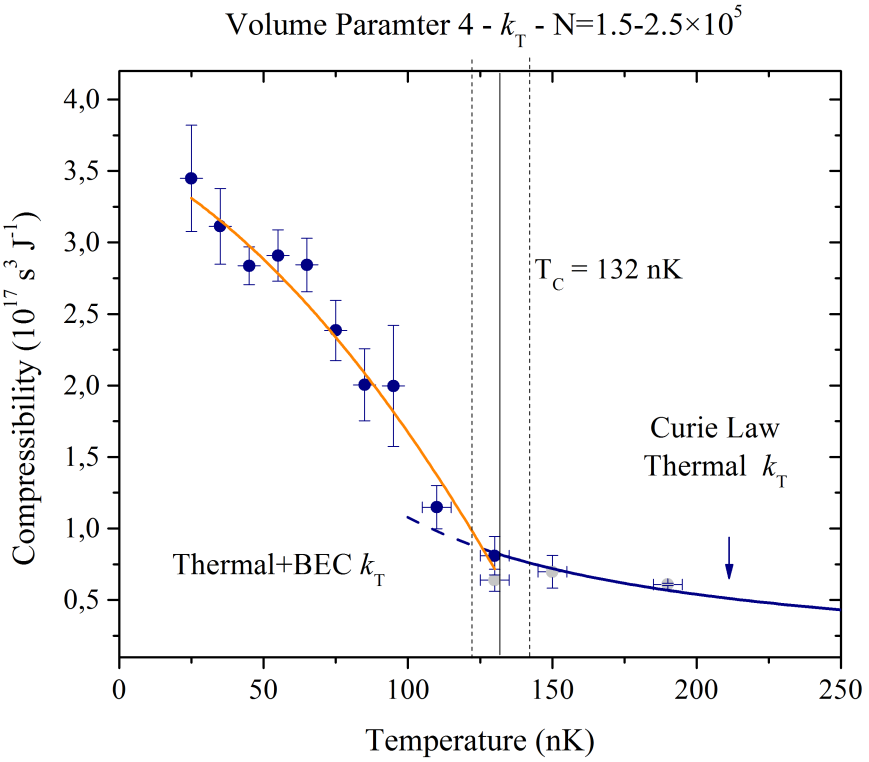

Figure 6.4.1 – $k_T \times T$ diagram. As expected, k_T above T_C obeys the Curie law (solid line). Source: elaborated by the author.

Chapter 7

Zero-point pressure

The study of the pressure parameter as $T \to 0$ and $N \to 0$, Π_0^Q, was done from the $\Pi \times T$ phase diagram for different total number of atoms in each of the six volume parameters. By calculating the pressure parameter from eq. (6.2.1) with the right density distribution it was possible to group the images by their total number of atoms. The conventional curve of the pressure parameter as a function of T for a specific total number of trapped atoms is displayed in Fig. 6.3.7. Between T_C and $T = 0$ the pressure parameter is composed by two contributions: one from the thermal cloud and another from the Thomas-Fermi cloud. As $T \to 0$ the condensate contribution becomes dominant until we obtain the pressure parameter of the pure quantum gas, Π_0' at $T = 0$. Equivalent curves were obtained for different number of atoms at different $\mathcal{V}$ allowing the determination of $\Pi_0(N)$ for each studied $\mathcal{V}$.

The solid lines are exponential curves that best fits in the experimental data below T_C. From these curves the extrapolated value for the pressure parameter Π_0 at $T = 0$. In this form, from eq. (6.2.7) we have

$$\Pi_q\left(T \to 0\right) \equiv \Pi_0 = \frac{1}{7}\left(15 a_s \hbar^2 \sqrt{m}\right)^{2/5} \left(\frac{N}{\mathcal{V}}\right)^{7/5}. \tag{7.0.1}$$

where a_s is the s-wave scattering length of the atomic cloud. We can see that for $T = 0$ Π_0 will depend only to the scattering length of the cloud and its total number of atoms, as shown in eq. (7.0.1).

In the simplified analytical analysis $\Pi_0(N \to 0) \equiv \Pi_0^Q = 0$, nevertheless due to the confining potential a residual fully *quantized pressure* is present in the limit $N \to 0$ and $T \to 0$. From the data of Figs. 6.3.2-6.3.6 we obtain the experimental curve of Π_0 for each volume parameter. The result is displayed in Fig. 7.0.1-7.0.5. The solid curve is the fitting of eq. (7.0.1) plus a constant term, Π_0^Q. The experimental data is in good agreement with the expect values for Π_0, as expressed in eq. (7.0.1). The points with high N show some divergence that can be explained by the fact that the extrapolation for getting Π_0 gets less precise as the temperature increases. From the constant term, Π_0^Q, we obtained the *zero-point pressure parameter* which follows plotted on Fig. 7.0.6.

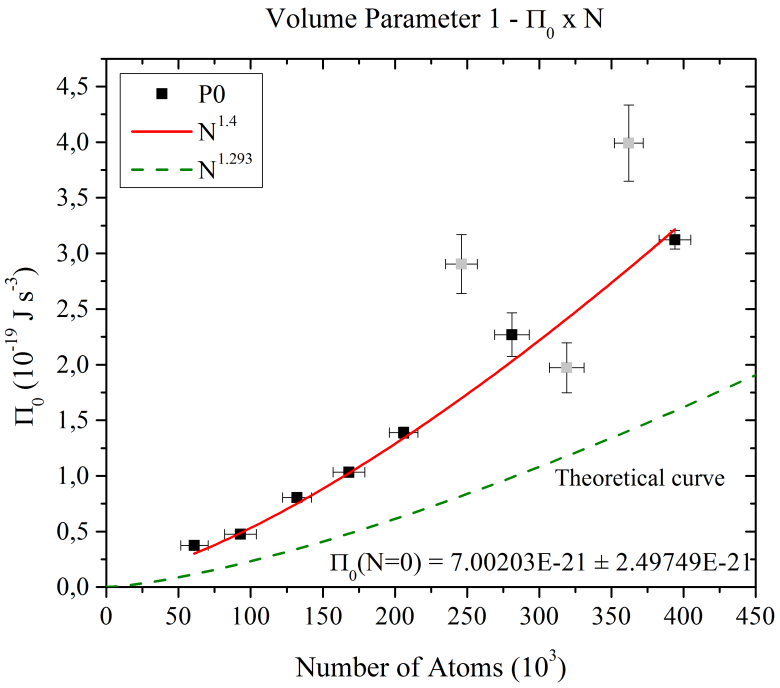

Figure 7.0.1 – Pressure parameter for $T = 0$, Π_0 for $\mathcal{V}_1$ as a function of the total number of atoms, N . The dash curve represents the curve of Eq. (7.0.1) in each case. The solid curve is the best experimental adjust proportional to $N^{7/5}$ at low number. Source: elaborated by the author.

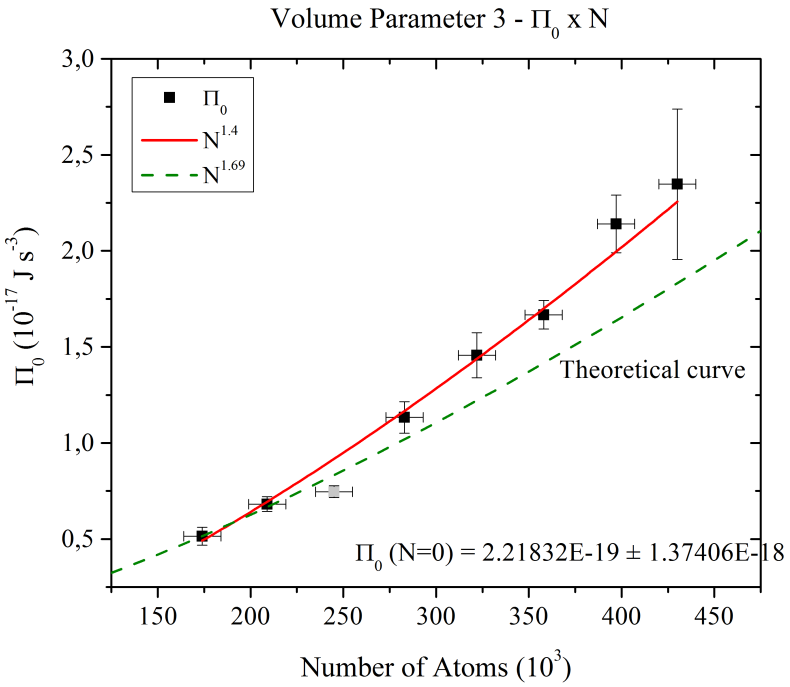

Figure 7.0.2 – Pressure parameter for $T = 0$, Π_0 for $\mathcal{V}_3$ as a function of the total number of atoms, N. The dash curve represents the curve of Eq. (7.0.1) in each case. The solid curve is the best experimental adjust proportional to $N^{7/5}$ at low number. Source: elaborated by the author.

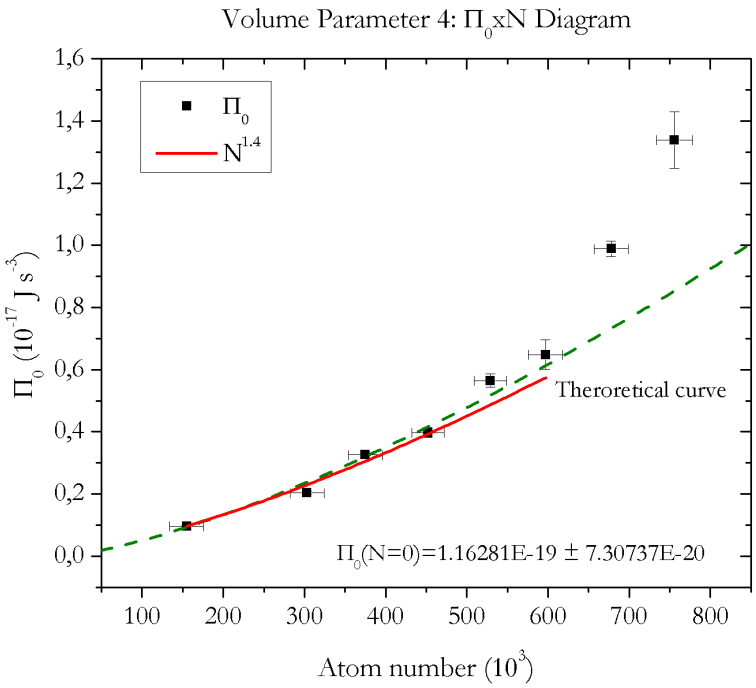

Figure 7.0.3 – Pressure parameter for $T = 0$, Π_0 for $\mathcal{V}_4$ as a function of the total number of atoms, N . The dash curve represents the curve of Eq. (7.0.1) in each case. The solid curve is the best experimental adjust proportional to $N^{7/5}$ at low number. Source: elaborated by the author.

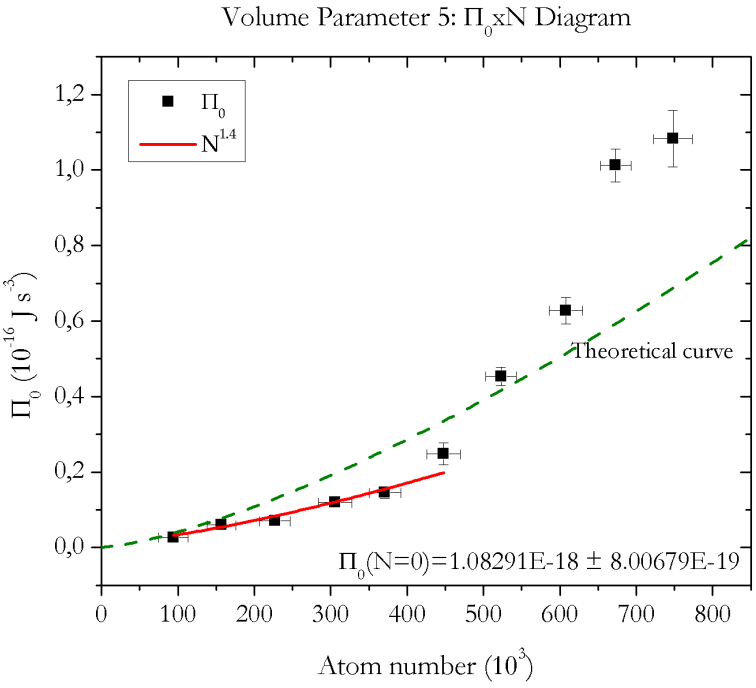

Figure 7.0.4 – Pressure parameter for $T = 0$, Π_0 for $\mathcal{V}_5$ as a function of the total number of atoms, N . The dash curve represents the curve of Eq. (7.0.1) in each case. The solid curve is the best experimental adjust proportional to $N^{7/5}$ at low number. Source: elaborated by the author.

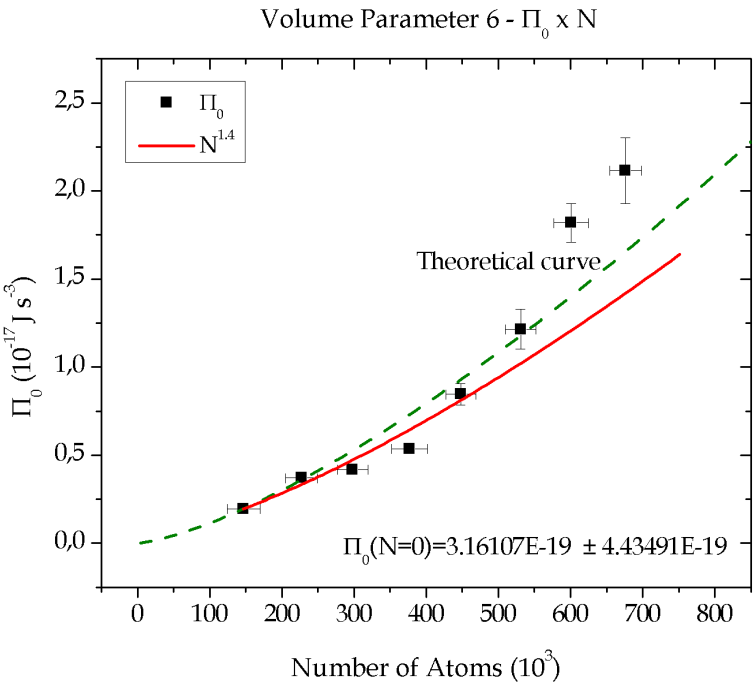

Figure 7.0.5 – Pressure parameter for $T = 0$, Π_0 for $\mathcal{V}_6$ as a function of the total number of atoms, N. The dash curve represents the curve of Eq. (7.0.1) in each case. The solid curve is the best experimental adjust proportional to $N^{7/5}$ at low number. Source: elaborated by the author.

One estimation of the pressure of quantum nature can be done considering the existence of just one trapped atom. The density profile used to calculate Π in eq. (6.2.1) can be evaluated for the equation of ground state of the harmonic oscillator given by

$$n(\vec{r}) = \left(\frac{m}{\pi\hbar}\right)^{3/2} (\omega_x\omega_y\omega_z)^{1/2} \exp\left[-\frac{m}{\hbar}\left(\omega_x x^2 + \omega_y y^2 + \omega_z z^2\right)\right]. \tag{7.0.2}$$

Using such density, Π_0^Q can be calculated as

$$\Pi_0^Q = \frac{1}{3}\frac{E_0}{\mathcal{V}} \tag{7.0.3}$$

where $E_0 = \frac{1}{2}\hbar(\omega_x + \omega_y + \omega_z)$ corresponds to the energy of ground state of the harmonic oscillator. The dependence of Π_0^Q/E_0 is a curve proportional to $\mathcal{V}^{-1}$, which fits well in our experimental points. It can be seen on Fig. 7.0.6.

The contribution Π_0^Q is due to the confinement as indicated by the Heisenberg Uncertainty Principle. Normally this contribution is small when compared with the pressure due to interactions (related with the Thomas-Fermi cloud). This fact somehow justify our conventional interpretation in which the expansion of the cloud is mainly due to the interaction between its particles. This is in agreement with our measurements since the estimated *zero-point pressure parameter* is at least in one order of magnitude smaller then the smaller Π_0 measured for each $\mathcal{V}$. The existence of Π_0^Q may be a relevant fact on the

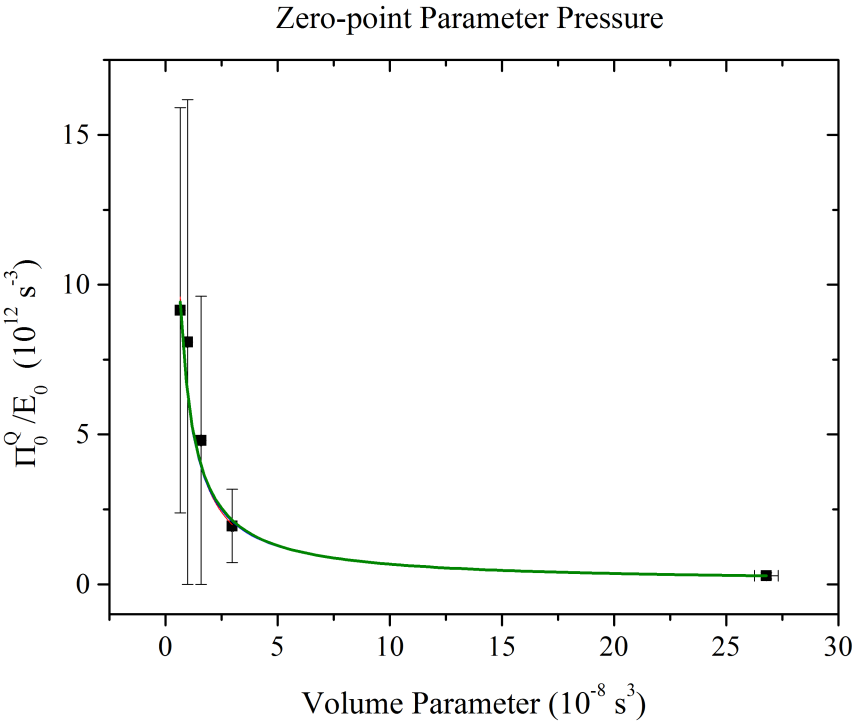

Figure 7.0.6 – Pressure parameter as a function $\mathcal{V}$, for $T \to 0$ and $N \to 0$, Π_0^Q is divided by E_0, $\Pi_0^Q/E_0 \sim \mathcal{V}^{-1}$. Source: elaborated by the author.

development of new techniques where the transport of atomic quantum fluids is relevant.

The Π_0^Q is normally related to the zero point motion. Considering l, a spatial variation of the wave-function for the condensate, the quantum pressure can be estimated as $\hbar^2/ml^3$ consistent with the expected dependence of $1/\mathcal{V}$ obtained with the experiment. The experimental determination of Π_0^Q gives some other interesting property of the condensate related with its quantum nature, but it is not relevant in conventional experimental situations. In such conditions the *pressure parameter* is dominated by the interaction term with a dependence of $a_s^{2/5}$ and $N^{7/5}$. The length scale of the spatial variation in the wave-function became smaller then the coherent length ($\epsilon \approx \hbar/(mna_s)^{1/2}$).

Chapter 8

Conclusions

In this work was demonstrated that it is possible to deal with thermodynamic quantities for a external harmonic potential equivalent to the pressure and volume (1, 43). In the Chapter 2, we define theoretically two new conjugated variables: an extensive variable known as *volume parameter* ($\mathcal{V}$), and another intensive variable known as *pressure parameter* (Π). We noticed in Chapters 5 and 6, that these variables can be obtained experimentally and independently. Experiments to reach this conclusion were implemented in a hybrid trap (HT), which is composed of magnetic trap (MT) and a an optical dipole trap (OT). This kind of trap is advantageous over a magnetic traps used in our group, because the OT allows us change of controled in a manner the geometry of the confinement potential.

The volume parameter $\mathcal{V}$, discussed in Chapter 5, it is a quantity related to the spatial extension of the sample. $\mathcal{V} = (\omega_x\omega_y\omega_z)^{-1}$ is the inverse of product of the frequencies of the harmonic trap, in fact this is directly proportional to the inverse cube of the geometric mean frequency. These frequencies were measured and calibrated as function of the OT power. $\mathcal{V}$ allowed us to characterize some of the physical parameters and some interesting aspects of the hybrid trap itself. One of the fundamental physical parameters is the *critical temperature* (T_C) as a function of number of atoms and the volume parameter.

The pressure parameter Π is a functional of density distribution of the atoms, we discussed Π in the Chapter 6. On the other hand, the density is bimodal because we have two components in the ultracold sample: the thermal cloud and condensate cloud. The thermal component obeys a usual equation of state for ideal gases in a harmonic trap. On the other hand, below T_C the interactions between atoms begin to be significant changing in the global behaviour of the sample. Following this path, we can construct phase diagrams $\Pi \times T$ and $\Pi \times N$ and we observe the isodensity and isothermal curves, respectively. We have demonstrated that Π and $\mathcal{V}$ are the appropiate thermodynamic variables for an inhomogeneous quantum gas a confined harmonic trap.

The $\Pi \times N$ diagram allows us to define the *isothermal compressibility parameter* k_T, which is related with the order of the transition. However, this last aspect requires a more detailed study of the experimental points. However, this diagram gives us an indication

that the compressibility no diverges at the transition. This behavior of the transition order is not reported in the literature (**??**).

In this work we have measured for the first time the *zero-point pressure* due to the quantum nature Π_0^Q, of an atomic cloud trapped in a harmonic potential (**??**). From the isodensity curves in the $\Pi \times T$ diagram we did exponential fits of those data below T_C the pressure parameter at $T = 0$ (Π_0). In this form,we have constructed a new phase-diagram $\Pi_0 \times N$, which was discussed in the Chapter 7. From this last diagram we extracted the extrapolated value for Π_0^Q for each of the studied volume parameters. Finally, the dependence with $\mathcal{V}$ of this pressure is fully quantum, and it was compared with a simplified analytic model confirming it to be proportional to $\mathcal{V}^{-1}$.

In summary, the results obtained using the HT indicate that we have a useful tool to face the complex problem of thermodynamics in trapped gases. Although there is still much to be explored, the first ideas that it is possible converge in a macroscopic characterization of ultracold BEC systems. In this way, we get a thermodynamic description of a sample, where the interactions play an important role, without losing the heterogeneous properties of the sample. Finally we could say that we have achieved a small progress in the understanding of MQPh.

Chapter 9

Perspectives

In a real ultracold gas the static and dynamic properties of the sample are governed by interactions. Usually, the collisions of the gas components are approximated using short-range isotropic potential. In the condensation stage, the potential should be repulsive to maintain system stability, otherwise the system collapses (11)[1]. Potentials that are attractive can be controlled in the laboratory using Feshbach resonances, and they can be brought to repulsive interaction regime (111).

The experimental observation of dipolar quantum gases,^{52}Cr (112), ^{164}Dy (24) and ^{168}Er (25), it opens a new way in the formalism and physical consequences to identify the thermodynamic variables. In a gas the dipolar interaction potential $\hat{V}(r)$ of the Hamiltonian in the eq. (3.2.1) is a composition of two types of interaction: a contact interaction, which is short-range, and an nonlocal anisotropic interaction, which is long-range. Without doubt the most unique features (113) where the thermodynamic defined above does not apply.

The potential of the form r^{-n} (n is a positive integer) remains an apex research. The thermodynamic properties of a system for hard spheres lying in the presence of a dipolar potential was numerically studied by Elfimova in ref. (114). The effects of dimension in this type of systems have been studied by Minina in ref. (115). In the two last references, the system is above the critical temperature of condensation, that is, the equation of state is deduced for a classical system. On the other hand, the quantum effects for low-dimensional systems are studied in more detail in ref. (116).

The formal tools used so far in the literature to study thermodynamics are made using the usual volume and pressure, which are not set properly due to the external potential. Implement a formalism with global variables in the style of Romero-Rochín (1) taking into account the effects of dipolar interaction with the external potential, so we can deduce the properties and thermodynamic equation of state. Remember that the thermodynamics of finite systems is still a fact open to discussion and new contributions in the field of atomic and molecular physics and the like.

Another interesting consideration in the formalism is an extension due to influence

[1] The influence of the interaction has been extensively studied with ^{7}Li .

of internal degrees of freedom such as hyperfine spin. A system has several projections of the hyperfine spin is known in the literature as spinors. In fact, the dynamics of collisions and exchange of spins will have a selection rule determined by the hyperfine state. These ultracold collisions still belong to the interaction of low energy, i.e. below a certain critical temperature. This type of system has been widely studied theoretically in the refs. (117, 118), and experimentally in the refs. (9, 119, 120). The presence of several spin states allows us to make a long and explore the possibility of "spin-polarized gas mixture" quantum degenerate. This topic has been well studied by different authors considering non-interacting gases in homogeneous potentials (121, 122). We know that the interaction between spin components of an overwhelming physical features of these systems, especially in the interactions nature in finite systems (123). Importantly, a gas naturally dipole has components of spin and so it is natural to study the internal degrees of freedom.

References

1 ROMERO-ROCHÍN, V. Equation of state of an interacting bose gas confined by a harmonic trap: The role of the harmonic pressure. *Physical Review Letters*, v. 94, n. 13, p. 130601, 2005.

2 ANDERSON, M. H. et al. Observation of bose-einstein condensation in a dilute atomic vapor. *Science*, v. 269, n. 5221, p. 198–201, 1995.

3 DAVIS, K. B. et al. Bose-einstein condensation in a gas of sodium atoms. *Physical Review Letters*, v. 75, n. 22, p. 3969–3973, 1995.

4 BRADLEY, C. C. et al. Evidence of bose-einstein condensation in an atomic gas with attractive interactions. *Physical Review Letters*, v. 75, n. 9, p. 1687–1690, 1995.

5 PRITCHARD, D. E. Cooling neutral atoms in a magnetic trap for precision spectroscopy. *Physical Review Letters*, v. 51, n. 15, p. 1336–1339, 1983.

6 RAAB, E. L. et al. Trapping of neutral sodium atoms with radiation pressure. *Physical Review Letters*, v. 59, n. 23, p. 2631–2634, 1987.

7 MYATT, C. J. et al. Production of two overlapping bose-einstein condensates by sympathetic cooling. *Physical Review Letters*, v. 78, n. 4, p. 586–589, 1997.

8 ESSLINGER, T.; BLOCH, I.; HÄNSCH, T. W. Bose-einstein condensation in a quadrupole-ioffe-configuration trap. *Physical Review A*, v. 58, n. 4, p. R2664–R2667, 1998.

9 BARRET, M. D.; SAUER, J. A.; CHAPMAN, M. S. All-optical formation of an atomic bose-einstein condensate. *Physical Review Letters*, v. 87, n. 1, p. 010404, 2001.

10 LIN, Y.-J. et al. Rapid production of ^{87}Rb bose-einstein condensates in a combined magnetic and optical potential. *Physical Review A*, v. 79, n. 6, p. 063631, 2009.

11 BRADLEY, C. C.; SACKET, C. A.; HULET, R. G. Bose-einstein condensation of lithium: Observation of limited condensate number. *Physical Review Letters*, v. 78, n. 6, p. 985–989, 1997.

12 FRIED, D. G. et al. Bose-einstein condensation of atomic hydrogen. *Physical Review Letters*, v. 81, n. 18, p. 3811–3814, 1998.

13 CORNISH, S. L. et al. Stable ^{85}Rb bose-einstein condensates with widely tunable interactions. *Physical Review Letters*, v. 85, n. 9, p. 1795–1798, 2000.

14 SANTOS, F. P. D. et al. Bose-einstein condensation of metastable helium. *Physical Review Letters*, v. 86, n. 16, p. 3459–3462, 2001.

15 ROBERT, A. et al. A bose-einstein condensate of metastable atoms. *Science*, v. 292, n. 5516, p. 461–464, 2001.

16 ROATI, G. et al. ^{39}K bose-einstein condensate with tunable interactions. *Physical Review Letters*, v. 99, n. 1, p. 010403, 2007.

17 MODUGNO, G. et al. Bose-einstein condensation of potassium atoms by sympathetic cooling. *Science*, v. 294, n. 5545, p. 1320–1322, 2001.

18 WEBER, T. et al. Bose-einstein condensation of cesium. *Science*, v. 299, n. 5604, p. 232–235, 2003.

19 FUKUHURA, T.; SUGAWA, S.; TAKAHASHI, Y. Bose-einstein condensation of an ytterbium isotope. *Physical Review A*, v. 76, n. 5, p. 051604(R), 2007.

20 TAKASU, Y. et al. Spin-singlet bose-einstein condensation of two-electron atoms. *Physical Review Letters*, v. 91, n. 4, p. 040404, 2003.

21 GRIESMAIER, A. et al. Bose-einstein condensation of chromium. *Physical Review Letters*, v. 94, n. 16, p. 160401, 2004.

22 KRAFT, S. et al. Bose-einstein condensation of alkaline earth atoms: ^{40}Ca. *Physical Review Letters*, v. 103, n. 13, p. 130401, 2009.

23 STELLMER, S. et al. Bose-einstein condensation of strontium. *Physical Review Letters*, v. 103, n. 20, p. 200401, 2009.

24 LU, M. et al. Strongly dipolar bose-einstein condensate of dysprosium. *Physical Review Letters*, v. 107, n. 19, p. 190401, 2011.

25 AIKAWA, K. et al. Bose-einstein condensation of erbium. *Physical Review Letters*, v. 108, n. 21, p. 210401, 2012.

26 BLOCH, I.; DALIBARD, J.; ZWERGER, W. Many-body physics with ultracold gases. *Review of Modern Physics*, v. 80, n. 3, p. 885–964, 2008.

27 CRONIN, A. D.; SCHMIEDMAYER, J.; PRITCHARD, D. E. Optics and interferometry with atoms and molecules. *Review of Modern Physics*, v. 81, n. 3, p. 1051–1129, 2009.

28 DEREVIANKO, A.; KATORI, H. Colloquium: physics of optical lattice clocks. *Review of Modern Physics*, v. 83, p. 331–347, 2011.

29 HENN, E. A. L. et al. Emergence of turbulence in an oscillating bose-einstein condensate. *Physical Review Letters*, v. 103, n. 4, p. 045301, 2009.

30 KLAERS, J. et al. Bose-einstein condensation of photons in an optical microcavity. *Nature*, v. 468, n. 9567, p. 545–548, 2010.

31 NIKUNI, T. et al. Bose-einstein condensation of dilute magnons in $TlCuCl_3$. *Physical Review A*, v. 84, n. 25, p. 5868–5871, 2000.

32 DEMOKRITOV, S. O. et al. Bose-einstein condensation of quasi-equilibrium magnons at room temperature under pumping. *Nature*, v. 443, n. 5117, p. 430–433, 2006.

33 LONDON, F. The λ-phenomenon of liquid helium and the bose-einstein degeneracy. *Nature*, v. 141, p. 643–644, 1938.

34 HORIKOSHI, M. et al. Measurement of universal thermodynamic functions for a unitary fermi gas. *Science*, v. 327, n. 5964, p. 442–445, 2010.

35 YEFSAH, T. et al. Exploring the thermodynamics of a two-dimensional bose gas. *Physical Review Letters*, v. 107, n. 13, p. 130401, 2011.

36 PASQUIOU, B. et al. Thermodynamics of a bose-einstein condensate with free magnetization. *Physical Review Letters*, v. 108, n. 4, p. 045307, 2012.

37 ROMERO-ROCHÍN, V. et al. Observation of bose-einstein condensation in an atomic trap in terms of macroscopic thermodynamic parameters. *Physical Review A*, v. 85, n. 2, p. 023632, 2012.

38 SILVA, R. R. et al. Definition and measurement of global thermodynamic variables for laser-cooled trapped gas. *Laser Physics*, v. 16, n. 4, p. 687–692, 2006.

39 HENN, E. A. L. et al. Thermodynamics of cold trapped atoms and bose-einstein condensates described by global variables. *Journal of Electron Spectroscopy and Related Phenomena*, v. 156, p. LVIII, 2007.

40 MEPPELINK, R. et al. Thermodynamics of bose-einstein-condensed clouds using phase-contrast imaging. *Physical Review A*, v. 81, n. 5, p. 053632, 2010.

41 NASCIMBÈNE, S. et al. Exploring the thermodynamics of a universal fermi gas. *Nature*, v. 463, n. 8814, p. 1057–1060, 2010.

42 KU, M. J. H. et al. Revealing the superfluid lambda transition in the universal thermodynamics of a unitary fermi gas. *Science*, v. 335, n. 6068, p. 563–567, 2012.

43 ROMERO-ROCHÍN, V.; BAGNATO, V. S. Thermodynamics of an ideal gas of bosons harmonically trapped: Equation of state and susceptibilities. *Brazilian Journal of Physics*, v. 35, n. 3A, p. 607–613, 2005.

44 LONDON. *Superfluids:* macroscopic theory of superfluid helium . New York: Dover Publications, 1954.

45 GENNES, P. D. *Superconductivity of metals and alloys*. New York: Advanced Book Program, Perseus Books, 1999. (Advanced book classics).

46 TINKHAM, M. *Introduction to superconductivity*. New York: Dover Publications, 2004. (Dover books on physics and chemistry).

47 PETHICK, C. J.; SMITH, H. *Bose-Einstein condensation in dilute gases*. Cambridge: Cambridge University Press, 2002.

48 PITAEVSKII, L.; STRINGARI, S. *Bose-Einstein condensation*. Oxford: Oxford University Press, 2003.

49 KAPITZA, P. Viscosity of liquid helium below the λ-point. *Nature*, v. 141, n. 3558, p. 74–74, 1938.

50 ALLEN, J. F.; MISENER, A. D. Flow of liquid helium ii. *Nature*, v. 141, n. 3558, p. 75–75, 1938.

51 LONDON, F. On the bose-einstein condensation. *Physical Review*, v. 54, n. 11, p. 947–954, 1938.

52 PUTTERMAN, S. J. *Superfluid hydrodynamics*. Amsterdam: North-Holland, 1974. (North-Holland series in low temperature physics).

53 GARROD, C.; SIMMONS, C. Rigorous statistical mechanics for nonuniform systems. *Journal of Mathematical Physics*, v. 13, n. 8, p. 1168, 1972.

54 MARCHIORO, C.; PRESUTTI, E. Thermodynamics of particle systems in the presence of external macroscopic fields. *Communications in Mathematical Physics*, v. 27, n. 2, p. 146–154, 1972.

55 MARCHIORO, C.; PRESUTTI, E. Thermodynamics of particle systems in the presence of external macroscopic fields. *Communications in Mathematical Physics*, v. 29, n. 4, p. 265–284, 1973.

56 HUANG, K. *Statistical mechanics*. New York: John Wiley and Sons, Inc, 1963.

57 REICHL, L. E. *A modern course in statistical physics*. New York: Wiley, 2009.

58 GRANDY, W. T. J. *Foundations of statistical mechanics:* equilibrium theory. Dordrecht: Springer, 1987.

59 FUJIWARA, I.; HAAR, D. t. ter; WERGELAND, H. Fluctuations in the population of the ground state of bose systems. *Journal of Statistical Physics*, v. 2, n. 4, p. 329–346, 1970.

60 SANDOVAL-FIGUEROA, N.; ROMERO-ROCHÍN, V. Thermodynamics of trapped gases: generalized mechanical variables, equation of state, and heat capacity. *Physical Review E*, v. 78, n. 6, p. 061129, 2008.

61 ZIFF, R. M.; UHLENBECK, G. E.; KAC, M. The ideal bose-einstein gas, revisited. *Physics Reports*, v. 32, n. 4, p. 169–248, 1977.

62 BAGNATO, V.; PRITCHARD, D. E.; KLEPPNER, D. Bose-einstein condensation in an external potential. *Physical Review A*, v. 35, n. 10, p. 4354–4358, 1987.

63 BAGNATO, V.; KLEPPNER, D. Bose-einstein condensation in low-dimensional traps. *Physical Review A*, v. 44, n. 11, p. 7439–7441, 1991.

64 LEGGETT, A. *Quantum liquids:* bose condensation and cooper pairing in condensed-matter systems. Oxford: Oxford University Press, 2006. (Oxford graduate texts in mathematics).

65 GRANDY, W. T. J. *Foundations of statistical mechanics:* nonequilibrium phenomena. Dordrecht: Springer, 1988.

66 MERMIN, N. D. Thermal properties of the inhomogeneous electron gas. *Physical Review*, v. 137, n. 5A, p. A1441–A1443, 1965.

67 HOHENBERG, P.; KOHN, W. Inhomogeneous electron gas. *Physical Review*, v. 136, n. 3B, p. B864–B871, 1964.

68 WIDOM, A. Statistical mechanics of rotating quantum liquids. *Physical Review*, v. 168, n. 1, p. 150–155, 1968.

69 WIDOM, A. Superfluid phase transitions in one and two dimensions. *Physical Review*, v. 176, n. 1, p. 254–257, 1968.

70 GROOT, S. R. de; HOOYMAN, G. J.; SELDMAN, C. A. T. On the bose-einstein condensation. *Proceedings of the Royal Society A*, v. 203, n. 1073, p. 266–286, 1950.

71 ROMERO-ROCHÍN, V. About generalized pressure and volume. Private communication.

72 KETTERLE, W.; DRUTEN, N. J. v. Bose-einstein condensation of a finite number of particles trapped in one or three dimensions. *Physical Review A*, v. 54, n. 1, p. 656–660, 1996.

73 KIRSTEN, K.; TOMS, D. J. Bose-einstein condensation of atomic gases in a general harmonic-oscillator confining potential trap. *Physical Review A*, v. 54, n. 5, p. 4188–4203, 1996.

74 SEMAN, J. A. *Study of excitations in a Bose-Einstein condensate.* 2011. 189 p. Tese (Doutorado) — Instituto de Física de São Carlos, Universidade de São Paulo, São Carlos, 2011.

75 CASTILHO, P. C. M. *Termodinâmica de condensados aprisionados em armadilhas óptico - magnéticas.* 2012. 107 p. Dissertação (Mestrado) — Instituto de Física de São Carlos, Universidade de São Paulo, São Carlos, 2012.

76 HELMERSON, K.; MARTIN, A.; PRITCHARD, D. E. Laser cooling of magnetically trapped neutral atoms. *Journal of Optical Society of America B*, v. 9, n. 11, p. 1988–1996, 1992.

77 MYATT, C. J. et al. Multiply loaded magneto-optical trap. *Optics Letters*, v. 21, n. 4, p. 290–292, 1996.

78 RAPOL, U. D.; WASAN, A.; NATARAJAN, V. Loading of a rb magneto-optic trap from a getter source. *Physical Review A*, v. 64, n. 2, p. 023402, 2001.

79 KETTERLE, W.; DURFEE, D. S.; STAMPER-KURN, D. M. Making, probing and understanding bose-einstein condensates. In: INGUSCIO, M.; STRINGARI, S.; WIEMAN, C. (Ed.). *Bose-Einstein condensation in atomic gases*. Varenna: IOS Press, 1999. (International School of Physics Enrico Fermi, v. 140).

80 STANLEY, H. *Introduction to phase transitions and critical phenomena*. Oxford: Oxford University Press, 1971. (International series of monographs on physics).

81 BERGEMAN, T.; EREZ, G.; METCALF, H. J. Magnetostatic trapping fields for neutral atoms. *Physical Review A*, v. 35, n. 4, p. 1535–1546, 1987.

82 COOK, R. J. Atomic motion in resonant radiation: an application of ehrenfest's theorem. *Physical Review A*, v. 20, n. 5, p. 224–227, 1979.

83 COOK, R. J. Theory of resonance-radiation pressure. *Physical Review A*, v. 22, n. 3, p. 1078–1098, 1980.

84 METCALF, H. J.; STRATEN, P. V. D. *Laser cooling and trapping*. New York: Springer-Verlag GmbH, 1999. (Graduate texts in contemporary physics).

85 FOOT, C. *Atomic physics*. Oxford: Oxford University Press, 2005.

86 SUTER, D. *The physics of laser - atom interactions*. Cambridge: Cambridge University Press, 1997. (Cambridge studies in modern optics).

87 SMYTHE, W. *Static and dynamic electricity*. New York: McGraw-Hill, 1967. (International series in pure and applied physics).

88 BERGEMAN, T. H. et al. Quantized motion of atoms in a quadrupole magnetostatic trap. *Journal of Optical Society of America B*, v. 6, n. 11, p. 2249–2256, 1989.

89 PETRICH, W. et al. Stable, tightly confining magnetic trap for evaporative cooling of neutral atoms. *Physical Review Letters*, v. 74, n. 17, p. 3352–3355, 1995.

90 MEWES, M. O. et al. Bose-einstein condensation in a tightly confining dc magnetic trap. *Physical Review Letters*, v. 77, n. 3, p. 416–419, 1996.

91 GRIMM, R.; WEIDEMÜLLER, M.; OVCHINNIKOV, Y. B. Optical dipole traps for neutral atoms. *Advances In Atomic, Molecular, and Optical Physics*, v. 42, p. 95–170, 2000.

92 NES, J. *Cold Atoms and Bose-Einstein condensates in optical dipole potentials.* 2008. 89 p. Tese (Doutorado) — Vom Fachbereich Physik , Technischen Universität Darmstadt, Darmstadt, 2008.

93 COHEN-TANNOUDJI, C.; REYNAUD, S. Dressed-atom description of resonance fluorescence and absorption spectra of a multi-level atom in an intense laser beam. *Journal of Physics B:* atomic, molecular and optical physics, v. 10, n. 3, p. 345, 1977.

94 DALIBARD, J.; COHEN-TANNOUDJI, C. Dressed-atom approach to atomic motion in laser light: the dipole force revisited. *Journal of Optical Society of America B*, v. 2, n. 11, p. 1707–1720, 1985.

95 CHU, S. et al. Experimental observation of optically trapped atoms. *Physical Review Letters*, v. 57, n. 3, p. 314–317, 1986.

96 HENN, E. A. L. et al. Bose-einstein condensation in ^{87}Rb characterization of the brazilian experiment. *Brazilian Journal of Physics*, v. 38, n. 2, p. 279–286, 2008.

97 MAYER, J. E.; MAYER, M. G. *Statistical mechanics*. New York: Wiley, 1977.

98 STRINGARI, S. Collective excitations of a trapped bose-condensed gas. *Physical Review Letters*, v. 77, n. 12, p. 2360–2363, 1996.

99 SHENOY, V. B.; HO, T. L. First and second sound modes of a bose-einstein condensate in a harmonic trap. *Physical Review Letters*, v. 80, n. 18, p. 3895–3898, 1998.

100 ANDREWS, M. R. et al. Direct, nondestructive observation of a bose condensate. *Science*, v. 273, n. 5271, p. 84–87, 1996.

101 CASTIN, Y.; DUM, R. Bose-einstein condensates in time dependent traps. *Physical Review Letters*, v. 77, n. 27, p. 5315–5319, 1996.

102 KAGAN, Y.; SURKOV, E. L.; SHLYAPNIKOV, G. V. Evolution of a bose gas in anisotropic time-dependent traps. *Physical Review A*, v. 55, n. 1, p. R18–R21, 1997.

103 COURTEILLE, P. W.; BAGNATO, V. S.; YUKALOV, V. I. Bose-einstein condensation of trapped atomic gases. *Laser Physics*, v. 11, n. 6, p. 659–800, 2001.

104 PIZA, T. A. F. R. *Mecânica quântica*. São Paulo: Edusp, 2009.

105 LANDAU, L.; L., L. *Statistical physics*. Oxford: Butterword-Heinemann, 2000.

106 LIEB, E. H.; SEIRINGER, R.; YNGAVASON, J. Justification of c-number substitutions in bosonic hamiltonians. *Physical Review Letters*, v. 94, n. 8, p. 080401, 2005.

107 YUKALOV, V. I. Bose-einstein condensation and gauge symmetry breaking. *Laser Physics Letters*, v. 4, n. 9, p. 632–647, 2007.

108 MA, S.-K. *Modern theory of critical phenomena*. New York: Westview Press, 2000.

109 YUKALOV, V. I. Fluctuations of composite observables and stability of statistical systems. *Physical Review E*, v. 72, n. 6, p. 066119, 2005.

110 YUKALOV, V. I. Number-of-particle fluctuations in systems with bose-einstein condensate. *Laser Physics Letters*, v. 2, n. 3, p. 156–161, 2005.

111 KHAYKOVICH, L. et al. Formation of a matter-wave bright soliton. *Science*, v. 296, n. 5571, p. 1290–1293, 2002.

112 LAHAYE, T. et al. Strong dipolar effects in a quantum ferrofluid. *Nature*, v. 448, n. 6036, p. 672–675, 2007.

113 LAHAYE, T. et al. The physics of dipolar bosonic quantum gases. *Reports on Progress in Physics*, v. 72, n. 12, p. 126401, 2009.

114 ELFIMOVA, E. A.; IVANOV, A. O.; CAMP, P. J. Thermodynamics of dipolar hard spheres with low-to-intermediate coupling constants. *Physical Review E*, v. 86, n. 2, p. 021126, 2012.

115 MININA, E.; KANTOROVICH, S. The influence of dimensionality on the behavior of magnetic dipolar soft spheres: calculation of the pressure. *Journal of Physics:* condensed Matter, v. 25, n. 15, p. 155102, 2013.

116 ASTRAKHARCHIK, G. E.; LOZOVIK, Y. E. Super-tonks-girardeau regime in trapped one-dimensional dipolar gases. *Physical Review A*, v. 77, n. 1, p. 013404, 2008.

117 HO, T. L. Spinor bose condensates in optical trap. *Physical Review Letters*, v. 81, n. 4, p. 742–745, 1998.

118 KAWAGUCHI, Y.; UEDA, U. Symmetry classification of spinor bose-einstein condensates. *Physical Review A*, v. 84, n. 5, p. 053616, 2011.

119 GORLITZ, A. et al. Sodium bose-einstein condensates in the $f = 2$ state in a large-volume optical trap. *Physical Review Letters*, v. 90, n. 9, p. 090401, 2003.

120 CHANG, M.-S. et al. Coherent spinor dynamics in a spin-1 bose condensates. *Nature Physics*, v. 1, n. 153, p. 111–116, 2005.

121 DAVIDSON, N. *Statistical mechanics*. New York: McGraw-Hill, 1962.

122 FAY, J. A. *Molecular thermodynamics*. Massachusetts: Addison-Wesley publishing company, 1965.

123 HUHTAMÄKI, J. A. M. et al. Spin textures in condensates with large dipole moments. *Physical Review A*, v. 81, n. 6, p. 063623, 2010.

Appendix A

Complete phase diagrams

Diagrams of the pressure parameter as function of temperature to study the transition from the classical regime to quantum regime (see chapter **6**).

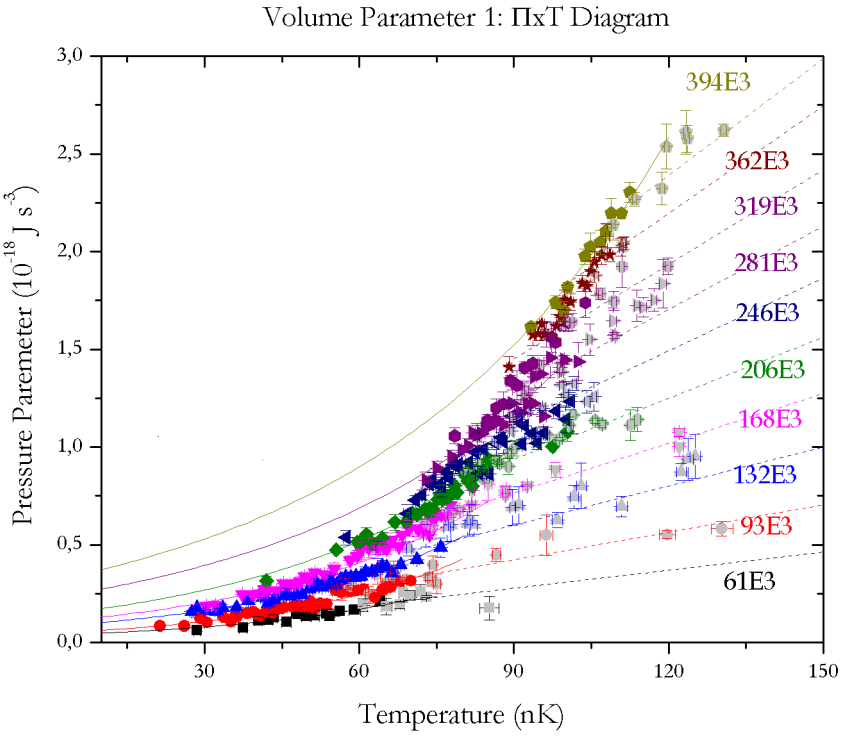

Figure A.0.1 – $\Pi \times T$ diagram for $\mathcal{V}_1$. Source: Elaborated by the author.

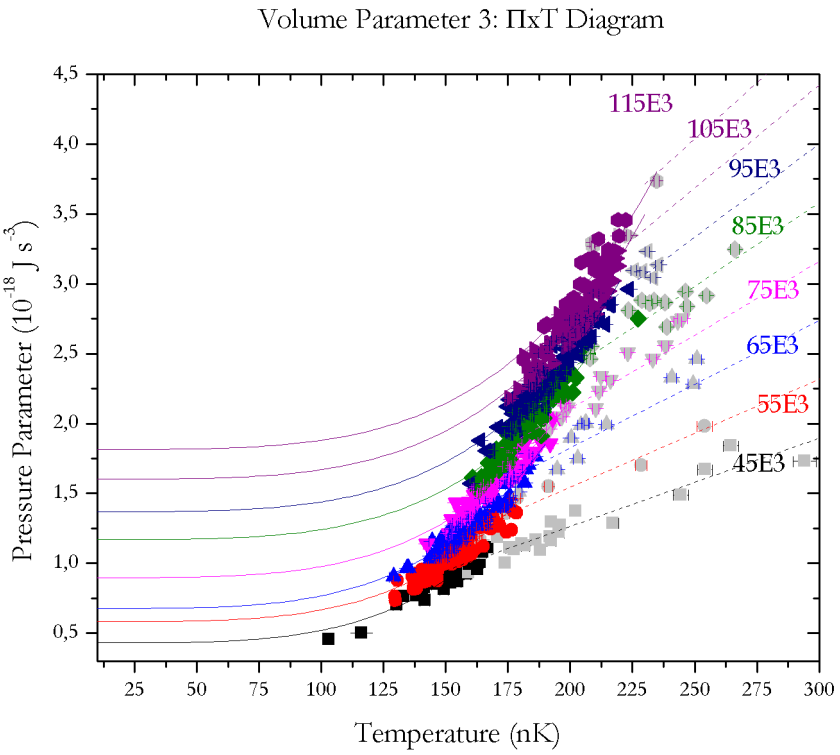

Figure A.0.2 – $\Pi \times T$ diagram for $\mathcal{V}_3$. Source: Elaborated by the author.

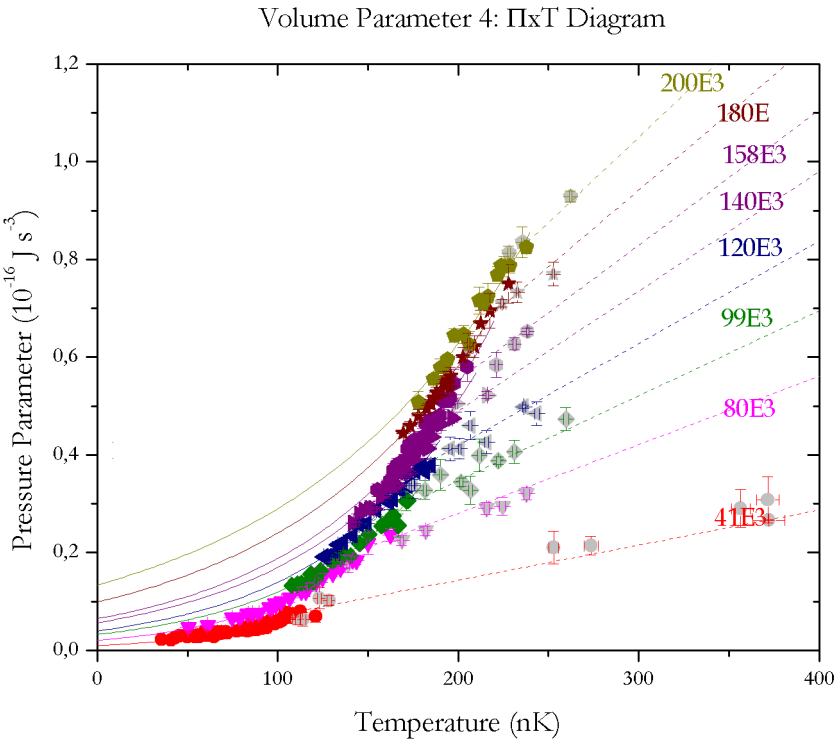

Figure A.0.3 – $\Pi \times T$ diagram for $\mathcal{V}_4$. Source: elaborated by the author.

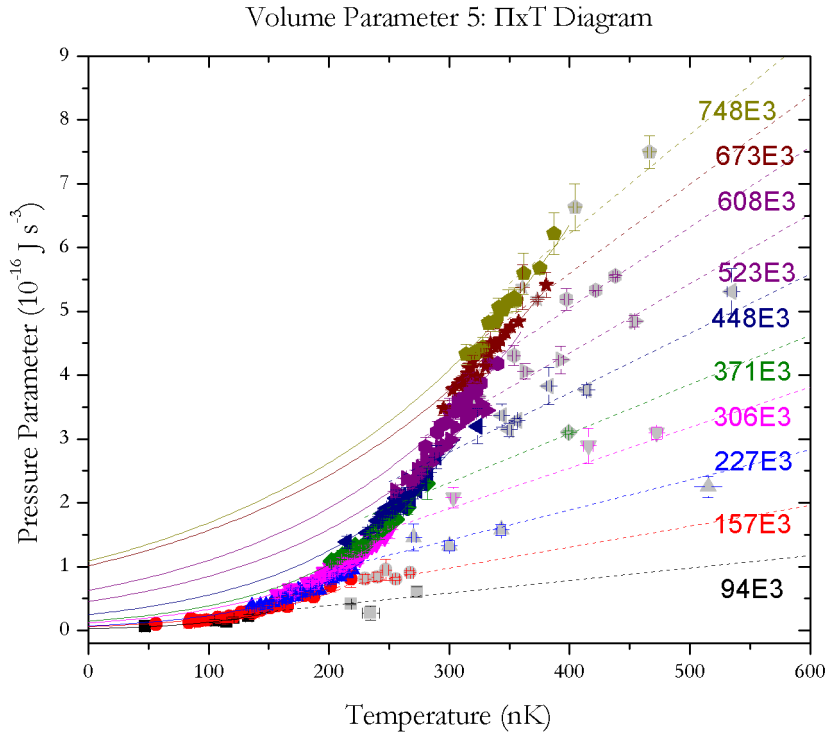

Figure A.0.4 – $\Pi \times T$ diagram for $\mathcal{V}_5$. Source: elaborated by the author.

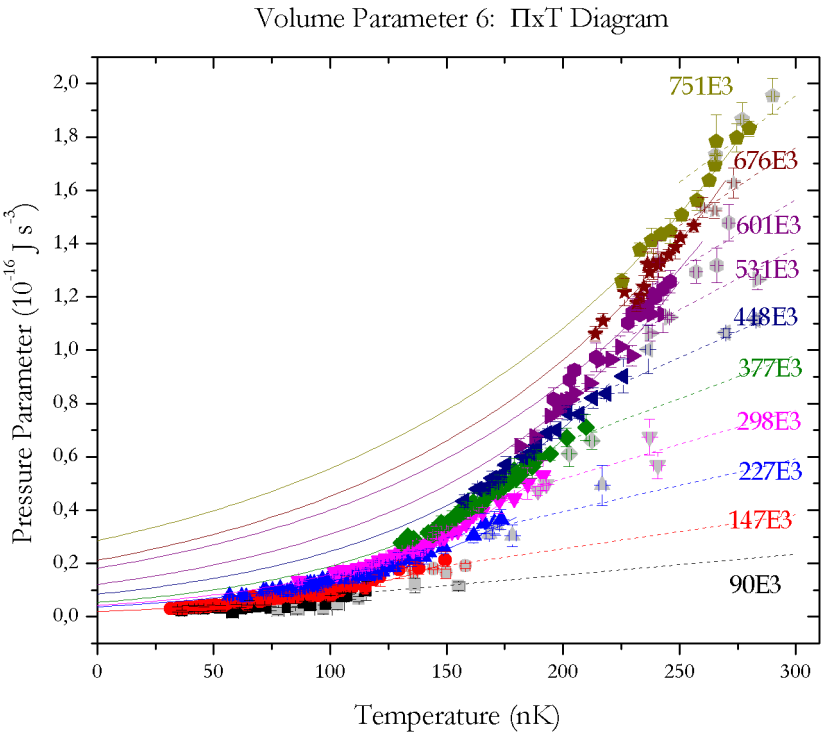

Figure A.0.5 – $\Pi \times T$ diagram for $\mathcal{V}_6$. Source: elaborated by the author.